Fluvial sedimentary response to late Quaternary climate and tectonics at the Himalayan Frontal Thrust, central Nepal

Mari Hamahashi[1], Judith Hubbard[2], Rafael Almeida[3], Samuel Haines[4], Lewis A Owen[5], Sanjita Mishra[6], and Soma Nath Sapkota[7]

[1]Kobe University, Kobe Ocean-Bottom Exploration Center
[2]Nanyang Technological University
[3]San Diego State University
[4]Earth Observatory of Singapore
[5]North Carolina State University
[6]Department of Mines and Geology, National Seismological Center, Nepal
[7]Department of Mines and Geology

November 24, 2022

Abstract

To investigate the subsurface structure surrounding the Main Frontal Thrust (MFT) in central Nepal, we drilled and cored sediments to depths of 45-100 m at ten sites. Our boreholes were located along previously acquired high-resolution seismic profiles across the MFT imaging the upper 1-2 km of the subsurface, which revealed a beveled erosional surface in the hanging wall above a broad, gentle anticline, as well as growth strata in the footwall. The boreholes exhibit interlayered clays, silts, sands, and gravels, dated with optically stimulated luminescence and radiocarbon to $<72.5\pm4.3$ ka, with a transition from finer to coarser sediments at ˜13.5±0.1 ka. Near the fault tip, the sediments exhibit steeper dips and deformation bands. A 25-m-thick section of silt and clay above the south end of the buried anticline is interpreted as a temporary lacustrine depocenter formed due to uplift near the fault tip. Based on the distribution of marker beds and sediment ages, we interpret a shortening rate of 3.1-12.1 mm/a on the MFT. Three major transitions between fluvio-lacustrine and coarse fluvial channel facies are inferred from the boreholes, and the timings of these transitions correlate with Indian monsoonal intensity variations linked to Earth's precession. We infer that strengthened monsoon led to increased river discharge and advance of coarse bedload-dominant braided channels, whereas weak monsoon formed a finer-grained channel environment. These monsoonal climate variations have affected the depositional environment and river base levels in this region, influencing the formation and apparent relative uplift of nearby river terraces.

Posted on 24 Nov 2022 — The copyright holder is the author/funder. All rights reserved. No reuse without permission. — https://doi.org/10.1002/essoar.10510280.1 — This a preprint and has not been peer reviewed. Data may be preliminary.

Fluvial sedimentary response to late Quaternary climate and tectonics at the Himalayan Frontal Thrust, central Nepal

Mari Hamahashi[1†], Judith A. Hubbard[1, 2], Rafael V. Almeida[3], Samuel H. Haines[1], Lewis A. Owen[4], Sanjita Mishra[5], and Soma Nath Sapkota[5]

[1]Earth Observatory of Singapore, Nanyang Technological University, Singapore, [2]Asian School of the Environment, Nanyang Technological University, Singapore, [3]Department of Geological Sciences, San Diego State University, USA, [4] Department of Marine, Earth, and Atmospheric Sciences, North Carolina State University, USA, [5] Department of Mines and Geology, National Seismological Center, Nepal

Corresponding author: Mari Hamahashi (mhamahashi@aquamarine.kobe-u.ac.jp)

†Current affiliation: Kobe Ocean-Bottom Exploration Center, Kobe University, Japan

Key Points:

- Boreholes combined with seismic profiles characterize the subsurface structure and stratigraphy across the Main Frontal Thrust
- We document major transitions from fluvio-lacustrine to coarse fluvial channel facies
- Indo-Asian monsoonal fluctuations have likely affected sediment supply and river base levels in the frontal Himalaya of central Nepal

Abstract

To investigate the subsurface structure surrounding the Main Frontal Thrust (MFT) in central Nepal, we drilled and cored sediments to depths of 45–100 m at ten sites. Our boreholes were located along previously acquired high-resolution seismic profiles across the MFT imaging the upper 1–2 km of the subsurface, which revealed a beveled erosional surface in the hanging wall above a broad, gentle anticline, as well as growth strata in the footwall. The boreholes exhibit interlayered clays, silts, sands, and gravels, dated with optically stimulated luminescence and radiocarbon to <72.5±4.3 ka, with a transition from finer to coarser sediments at ~13.5±0.1 ka. Near the fault tip, the sediments exhibit steeper dips and deformation bands. A 25-m-thick section of silt and clay above the south end of the buried anticline is interpreted as a temporary lacustrine depocenter formed due to uplift near the fault tip. Based on the distribution of marker beds and sediment ages, we interpret a shortening rate of 3.1–12.1 mm/a on the MFT. Three major transitions between fluvio-lacustrine and coarse fluvial channel facies are inferred from the boreholes, and the timings of these transitions correlate with Indian monsoonal intensity variations linked to Earth's precession. We infer that strengthened monsoon led to increased river discharge and advance of coarse bedload-dominant braided channels, whereas weak monsoon formed a finer-grained channel environment. These monsoonal climate

variations have affected the depositional environment and river base levels in this region, influencing the formation and apparent relative uplift of nearby river terraces.

Plain Language Summary

The Main Frontal Thrust (MFT) is the youngest and most active fault at the foot of the Himalayan mountain belt, posing a major seismic hazard to the dense populations living in the Himalaya and the Indo-Gangetic Plain. To study the recent deformation history of the MFT in central Nepal, we drilled and sampled sediments to depths of 45–100 m at ten sites. Our boreholes were located where previous surveys have imaged the structures of the MFT using a seismic technique. The recovered sediments consist of clays, silts, sands, and gravels. The deformation by the MFT is characterized by folding and steeply-dipping sediments at the tip of the fault. We used two different methods to date the ages of the sediments, called optically stimulated luminescence and radiocarbon dating. Based on the observed structures and sediment ages, we interpret that the MFT in this region is slipping at a rate of 3.1–12.1 mm/a. Three major transitions from coarse- to fine-grained sediments indicate past changes in the river environment; these correlate with Indian monsoonal climate changes. We interpret that monsoonal variations have significantly influenced

sediment deposition and erosion, impacting the geomorphology and relative uplift of the region.

1. Introduction

Understanding the processes that govern sediment supply and river base levels in an orogenic foreland is important for interpreting depositional processes, incision, and tectonic deformation. River base level, which is the lowest level of erosion or the highest level of sedimentary succession in a river profile, defines the equilibrium surface between deposition and incision (e.g., Blum & Tornqvist, 2000; Catuneanu et al., 2009). In tectonically active regions, rock uplift or subsidence is generally considered to be the main driver for local base-level change, leading to river incision or fluvial sediment deposition; an example of this interaction is steady-state topography models that assume that erosion balances rock uplift, and thus there is no change in the landscape over time (e.g., Willet & Brandon, 2002). Tectonic uplift plays a major role in the frontal Himalaya, where young active faults underlie and deform sediments at the piedmont.

Climate can also play an important role in modulating river base levels in foreland systems. In the Himalayan foreland, the Indian summer monsoon is responsible for more than 80% of the annual rainfall, significantly impacting river discharge and sediment flux in both the foreland and downstream in the Indo-Gangetic-Bengal basin (e.g., Bookhagen et al., 2010). Changes in the monsoonal climate are known to affect sedimentation and river base levels over various timescales (e.g., Plink-Björklund, 2015), but their effects in the proximal foreland are not well understood (Fig. 1). While river base levels close to the coast are primarily affected by sea level (e.g., Goodbred et al., 2014), those in the frontal foreland are largely influenced by sediment supply and the combined effects of climate and tectonics (e.g., Bookhagen et al., 2005; Fig. 1). This impact of climate on base level should be taken into account when interpreting tectonic deformation from geomorphology; here, we study this effect in the frontal Himalaya of central Nepal.

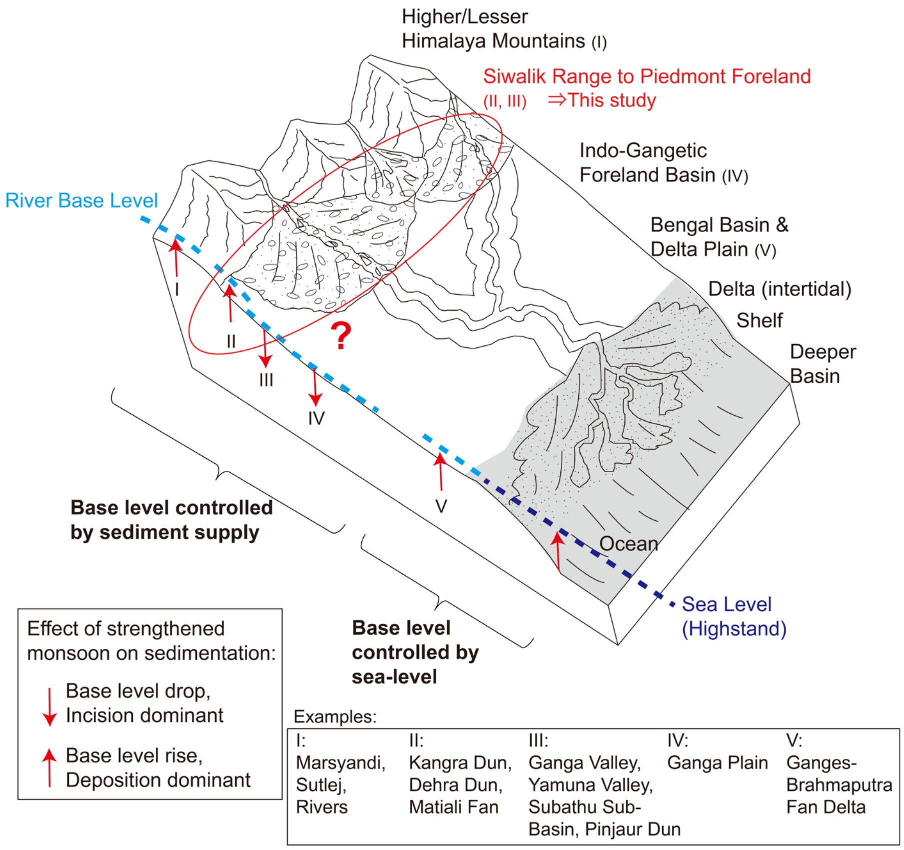

Figure 1. Variations in river base levels in the Himalayan foreland system in response to strengthened Indian monsoon, from the high mountains to the ocean basin. During strong Indian monsoon events, an increase in river discharge and sediment supply are inferred to cause aggradation and base level rise in regions I, II and V, whereas incision and base level fall occur in III and IV, notably variable within the piedmont foreland (regions II and III). An opposite process is inferred during weak monsoon periods. Base levels in regions I-IV are likely controlled mainly by sediment supply, whereas region V is controlled by sea level. References for each example in regions I-IV (lower rectangle) are as follows (locations are shown

in Supporting Information Figure S8). I: Marsyandi river (Pratt et al., 2002), Sutlej river (Bookhagen et al., 2005, 2006). II: Kangra dun (Thakur et al., 2014; Dey et al., 2016), Dehra dun (Densmore et al., 2016), Matiali fan (Kar et al., 2014). III: Ganga valley (Sinha et al., 2009; Ray and Srivastava, 2010), Yamuna valley (Dutta et al., 2012), Subathu sub-basin (Kumar et al., 2007), Pinjaur dun (Suresh et al., 2007). IV: Ganga plain (Srivastava et al., 2003b; Gibling et al., 2005; Sinha et al., 2007). V: Ganges-Brahmaputra fan delta (Goodbred and Kuehl, 2000 a,b; Goodbred et al., 2014; Pickering et al., 2014, 2017).

The thrust system at the foot of the Himalaya is composed of a largely right-stepping fault system called the Main Frontal Thrust (MFT), which dips 20º–40º to the north before linking with a gently dipping megathrust at 2–5 km depth, the Main Himalayan Thrust (MHT; Almeida et al., 2018). In the Bardibas region of central Nepal, this fault system has been imaged by high-resolution seismic profiles that cross two strands of the MFT, locally named the Bardibas and Patu thrusts, constraining both the local deformation and the depositional environment (Almeida et al., 2018; Liu et al., 2020; Figs. 2, 3; Supporting Information Fig. S1). These seismic profiles indicate that the southern MFT strand (the Bardibas thrust) at this location is blind (Figs. 3a,b).

Furthermore, as slip on this fault decreases to the west, the geomorphic signature of the fault decreases, with the westernmost 5 km of fault-related deformation completely erased by surface processes (Fig. 2c). In this tip region, the seismic profiles reveal a ~4-km-wide hanging-wall anticline bevelled by erosion and then later buried by ~100 m of sediments (Almeida et al., 2018; Fig. 3c). This relationship cannot be explained by tectonics alone, and implies that the local river base level was at least ~100 m lower at some point in the past. A scour surface interpreted as an incised valley within the growth strata of the footwall suggests that similar base-level changes may have occurred multiple times (Almeida et al., 2018).

To constrain the depositional patterns, rates of deformation, and evolution of inferred incision/aggradation events near the MFT in central Nepal, we drilled and cored the imaged stratigraphy to depths of 45–100 m below the surface (mbs) at ten locations in the hanging wall and footwall of the Bardibas thrust (Figs. 2, 3). Here, we characterize the sedimentary facies from recovered cores and report on sediment ages obtained by optically stimulated luminescence (OSL) and radiocarbon (^{14}C) dating. By combining our observations with previously acquired seismic profiles, our analyses allow us to 1) reconstruct the shallow structure and infer the slip rate of the Bardibas thrust, and 2) interpret the evolution of the depositional environment and river base levels in this region in relation to past climatic changes.

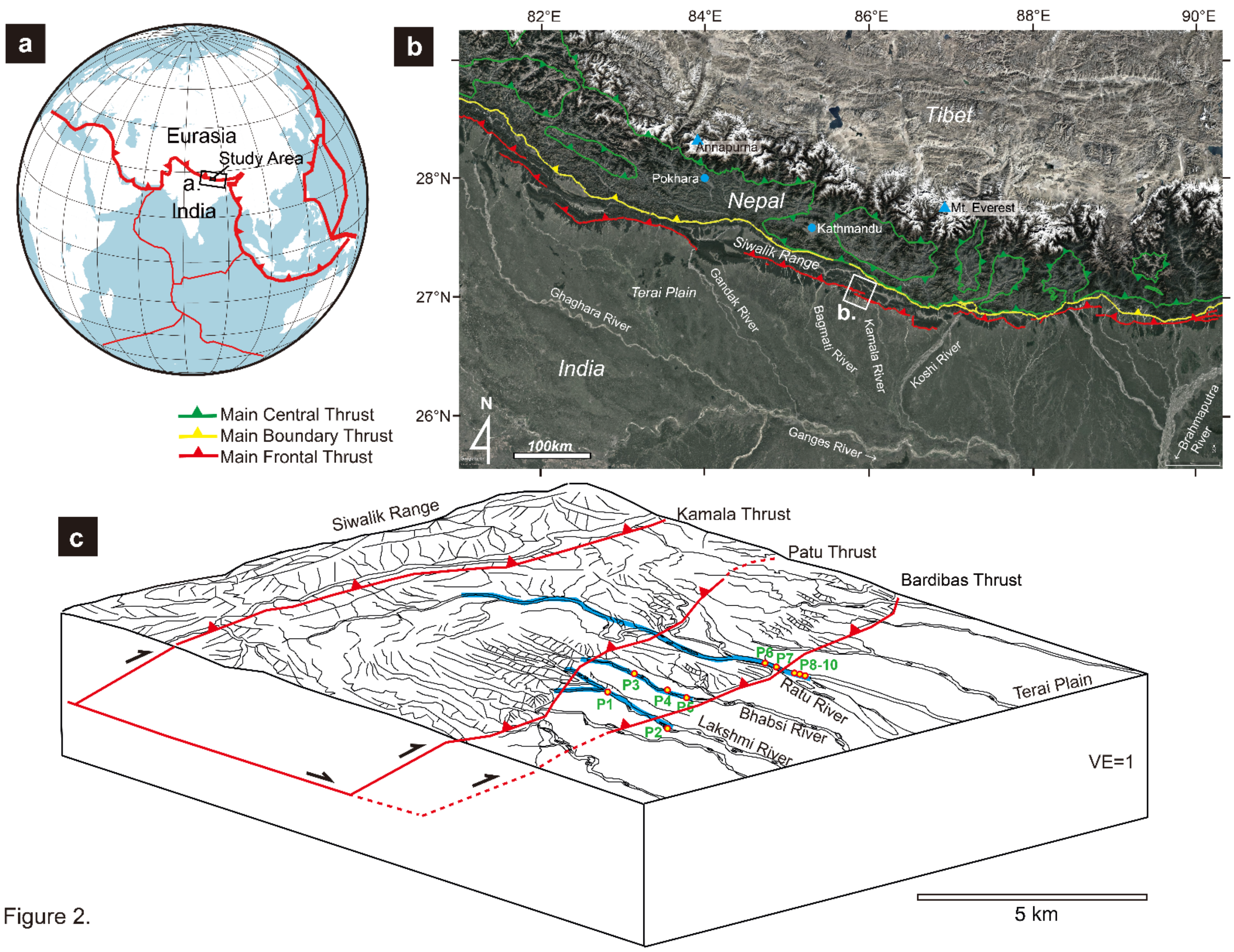

Figure 2.

Figure 2. Regional map of study area. (a) Major tectonic plate framework showing collision of India to Eurasia, and location of study area. Box shows location of (a). (b) Satellite image showing major Himalayan faults and river systems from high mountains to foreland basin (Terai plain). The Siwalik Range is located between the

Main Frontal Thrust and Main Boundary Thrust. White box marks the location of study area shown in (c). (c) Close-up of study area showing traced geography of the frontal foreland and braided river system. Drill sites are shown by yellow dots labeled P1–P10, along the Lakshmi, Bhabsi, and Ratu rivers. Blue lines show locations of previously acquired seismic reflection profiles along the rivers (Almeida et al., 2018; Liu et al., 2020) (Figure 3). Red lines: approximate locations of the fault strands of the Main Frontal Thrust in this region. Red dashed lines: locations where the fault displacement decreases and are likely terminated. The geomorphological signature of the Bardibas thrust decreases west of the Bhabsi river. No vertical exaggeration.

158 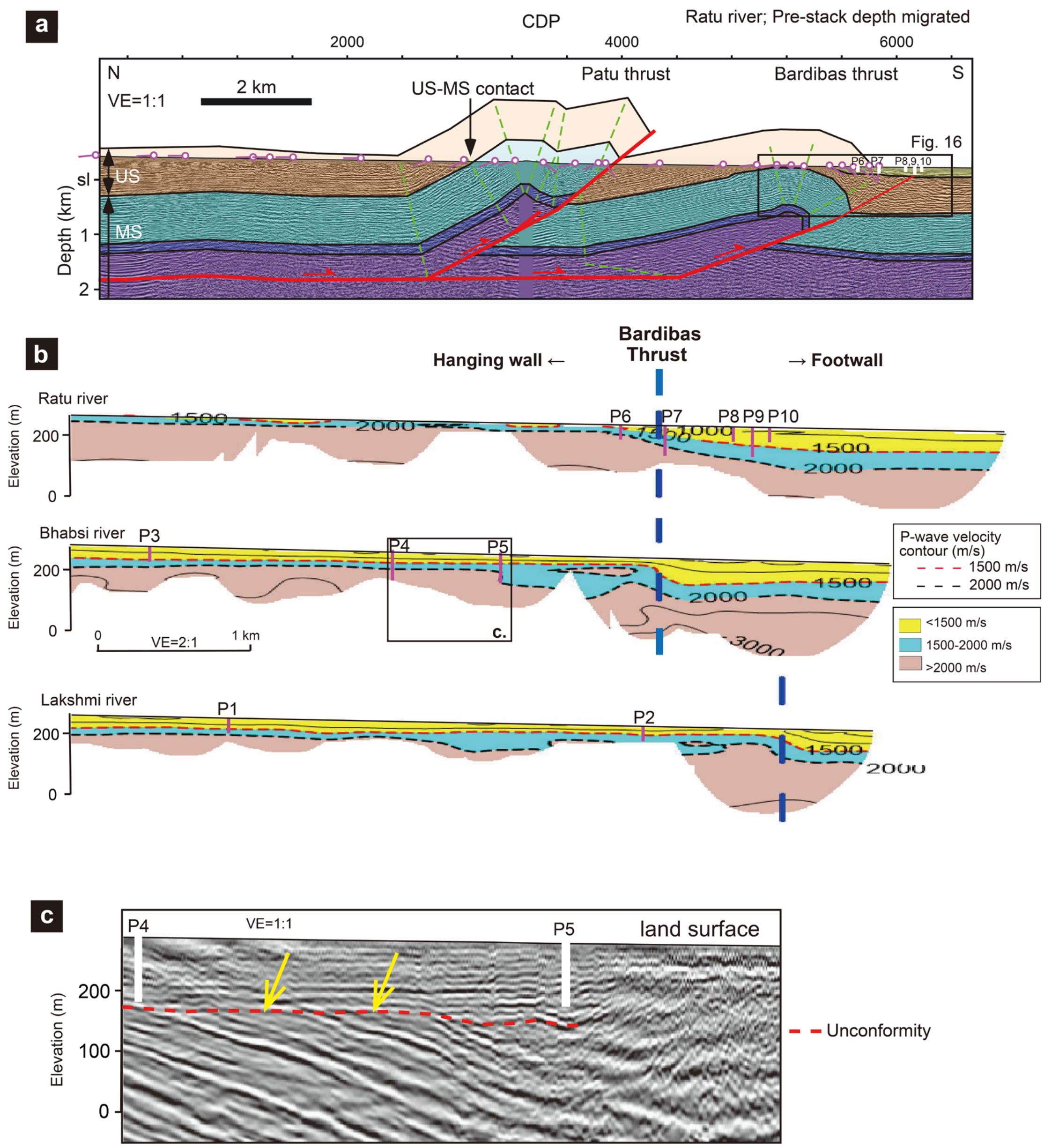

159 **Figure 3. Sections across the study area. (a) Interpreted Ratu river seismic profile**
160 **(pre-stack depth-migrated, no vertical exaggeration) by Almeida et al. (2018) (red**
161 **lines: thrusts; green dashed lines: axial surfaces). Uninterpreted profile is shown in**
162 **Supporting Information Fig. S1. CDP spacing is 2.5 m. Depth measurements are**
163 **with respect to sea-level (sl). White vertical bars show locations of borehole sites P6–**

P10 in this study. US: Upper Siwalik Group. MS: Middle Siwalik Group. Contact between US and MS observed in the field. Magenta tick marks: projected bedding dips measured from the field (Almeida et al., 2018). Area of black box is shown in Figure 16. (b) 2D refraction velocity models by Liu et al. (2020) generated from seismic data collected along Ratu, Bhabsi, and Lakshmi rivers (vertical exaggeration 2:1), with locations of borehole sites (magenta bars) P1–P10. Each contour line shows 500 m/s velocity interval. Red and black dashed lines show the 1500 and 2000 m/s contours, respectively. Blue vertical dashed lines represent the approximate location of the tip of the Bardibas thrust. Black box along Bhabsi river shows location of seismic reflection image shown in c. (c) Section of Bhabsi river seismic profile (post-stack depth-migrated, no vertical exaggeration) on the hanging wall of the Bardibas thrust by Almeida et al. (2018), showing close-up of the buried angular unconformity (marked by yellow arrows and red dashed line) between tilted Siwalik Group strata (below) and subhorizontal fluvial sediments (above). White vertical bars show locations of boreholes P4 and P5.

2. Geologic Setting

The Himalaya is currently accommodating shortening at a rate of ~13–21 mm/a (Larson et al., 1999; Ader et al., 2012; Lindsey et al., 2018). The MFT is the youngest and most active fault of the Himalayan orogen, extending >2500 km along strike. During the interseismic period, geodetic observations show shortening accumulating around the deep base of the megathrust, but most of this shortening is expected to eventually reach the surface as slip along the MFT (Lavé and Avouac, 2001), likely during or soon after large earthquakes, as inferred from paleoseismic studies (e.g., Nakata et al., 1998; Lavé et al., 2005; Sapkota et al., 2013; Bollinger et al., 2014; Wesnousky et al., 2017; Wesnousky, 2020; Dal Zilio et al., 2021). This seismic hazard poses a threat to the populations living in the Himalaya and its foothills, as well as the densely populated areas of the Indo-Gangetic Plain. The fault system also modifies the accommodation space and sediment supply to the largest foreland basin system on Earth, i.e., the Indo-Gangetic Plain (e.g., Kumar et al., 2007).

Our study area in central Nepal (Fig. 2) is located in the lowlands between the foothills of the Himalaya (the Siwaliks) and the Indo-Gangetic Plain, a region known as the Terai. Located within ~1 km south of the topographic range front, the area is actively deforming due to slip on the Patu and Bardibas thrusts (e.g., Bollinger et al., 2014;

Almeida et al., 2018) (Figs. 2, 3). Paleoseismic studies have identified fault offsets associated with the last two great (M>8) earthquakes in east-central Nepal along the Patu thrust (1255 and 1934 CE; Sapkota et al., 2013; Bollinger et al., 2014). In contrast, no surface rupture has been identified along the Bardibas thrust, although a fold scarp has been found (Bollinger et al., 2014).

The fault system here has been characterized by seismic reflection surveys, which imaged the ~20–30° north-dipping Bardibas thrust as blind, and the ~28–39° north-dipping Patu thrust as emergent (Figs. 3a; Almeida et al., 2018). Refraction velocities determined from the seismic data document the distribution of low-velocity sediments overlying the more lithified Siwalik bedrock in the hanging wall (~20–50 m thick) and footwall (~80–120 m thick) of the Bardibas thrust, indicating relatively recent sediment deposition across the fault, with ~60–70 m of uplift since their deposition (Fig. 3b; Liu et al., 2020). The effect of fault-related shortening on the Bardibas thrust should be to raise the hanging wall relative to base level and cause incision; the observation of deposition (Fig. 3c) therefore implies that another factor must be influencing base level, and the magnitude of that effect must exceed that of local tectonics. Specifically, exogenetic factors such as climate must play an important role in modulating the river base levels and incision in this region (Almeida et al., 2018).

The bedrock in the study region consists of the Miocene-Pliocene Siwalik Group, which is a set of fluvial strata comprising at large scale an overall coarsening-upward sequence of alternating beds of sandstone and siltstone with lenses of conglomerate, with smaller-scale fluvial successions showing fining-upward sequences (Corvinus, 2001; Ulak, 2009; Dhital, 2015; Supporting Information Fig. S2a). The current depositional environment is characterized by confined braided channels with minor overbank floodplains within a channel-dominant alluvial fan system. The contemporary alluvial fan is surrounded by abandoned river terraces, older alluvial fans, and uplifted hills.

The highest river terrace is ~70 m above the current riverbed and has a reported age of ~7 ka based on radiocarbon dating of a charcoal buried in the same horizon as cobble tool assemblages (artefacts of paleolithic industry) found within the sediments (Gaillard et al., 2011; Bollinger et al., 2014). A succession of six to seven younger river terraces, presumably abandoned during the Holocene, are also present (e.g., Gaillard et al., 2011; Bollinger et al., 2014). These river terraces are both deposition-dominant “fill terraces,” which exhibit thick alluvial fills not exposing the underlying bedrock, and incision-dominant “strath terraces,” which are underlain by tilted bedrock (Supporting Information Figs. S2b,c, S3). South of the Bardibas thrust, the rivers supply sediments into the Indo-Gangetic foreland basin between the Koshi and Gandak megafans (e.g., DeCelles and Cavazza, 1990; Sinha et al., 2014). Surprisingly, as the rivers travel hundreds of kilometers towards the southeast, their channel widths decrease (from ~300 m to ~10 m wide) (Supporting Information Fig. S4). Some of these narrow meandering channels are abandoned, while others eventually merge with the Koshi river and flow into the Ganges-Brahmaputra rivers and the Bay of Bengal (Supporting Information Fig. S4a).

In contrast to the major transverse Himalayan rivers, e.g., Ganga, Maakali, Karnali, Narayani, and Koshi rivers, which cut across the High Himalaya with large drainage basins, the catchment areas of the Lakshmi, Bhabsi, and Ratu rivers in this study are confined to the southern part of the Siwalik Range (area <100 km^2), and the drainages are hence younger (Fig. 2; Supporting Information Fig. S4). The rivers are supplied mainly by seasonal monsoon rainfall and associated runoff, with hardly any contribution of snowmelt (e.g., Bookhagen and Burbank, 2010). Annual rainfall around the Siwalik Range is about 2.8–3.8 m/a in central-eastern Nepal, with >80% of total precipitation occurring during the Indian summer monsoon (Bookhagen and Burbank, 2010). The moisture is derived from the Bay of Bengal and is carried north and rainfall peaks spatially south of the topographic barriers formed by the Lesser and Higher Himalayas (e.g., Bookhagen and Burbank, 2010; Hirschmiller et al., 2014; Deal et al., 2017). The rivers in the foreland thus have highly variable water discharge, experiencing high flow and flooding during the monsoon, with a long dry period for the rest of the year. Because the monsoon supplies large amounts of water to this river system, climate-driven changes in monsoon intensity are expected to be one of the key paleoenvironmental controls on its fluvial sedimentary record.

3. Methods

To investigate the subsurface structure surrounding the MFT, we drilled and cored sediments to depths of 45–100 m at ten sites (Sites P1-P10) across the fault. Drilling was conducted along the Lakshmi, Bhabsi and Ratu rivers around the town of Bardibas in the Mahottari district of central Nepal (Figs. 2). These rivers flow nearly perpendicular to the MFT. Sites P1–P5 are located on the hanging wall of the Bardibas thrust, whereas Sites P6–P10 are located on the footwall (Figs. 2b, 3).

Rotary drilling was applied using XUL-100 and UEW vol-35 drill rigs and NQ double core barrels, with core recovery of 28–59% (average: 41%), and maximum penetration depths of 45–100 mbs. There was no attempt to core the first 5 m of each borehole. Areas of low recovery were associated with coarse gravels and poorly sorted fluvial sediments. The cores were transferred from the core barrel to rolled tins with a mechanical extruder, tightly secured to avoid light exposure, transported to Kathmandu, and then cut in a dark room, preserving 25–30 cm of core every 2 m for sampling for OSL dating. The rest of the cores were then cut open, and laid in steel trays for observation.

The recovered cores were logged based on principal grain size range, sediment color, lithification, bed thickness, grading, sorting, clast size, sedimentary and deformation structures, weathering, organic content, and bioturbation (Supporting Information Dataset S1). The orientations of structures such as bedding were measured using core protractors by Holcombe Coughlin Oliver (www.hcovglobal.com). We also referred to the geotechnical reports from the drilling operations to infer the lithology where the cores had low or no recovery (Supporting Information Dataset S2). All core log data were digitized using Strater 5 (Golden Software LLC), and facies were interpreted. We combined our observations with the co-located seismic reflection profiles of Almeida et al. (2018; and unpublished data) to reconstruct regional cross-sections.

To date the sediments, we conducted OSL dating on quartz grains in fine sand, and accelerator mass spectrometry ^{14}C dating on organic sediments (see details in Supporting Information Texts S1, S2, Figs. S5–S7). Eighteen OSL samples were measured at the University of Cincinnati and North Carolina State University, using an automated Riso OSL reader model TL-DA-20. At least thirty-two quartz aliquots were measured for each sample. The single aliquot regeneration (SAR) method (Murray & Wintle, 2000, 2003) was used to determine the dose rate for age estimation. To help resolve the overestimate of ages due to partial bleaching and hence a large spreads of equivalent dose values (dispersion >25%), we applied a 2-mixing model (Vermeesch, 2009) to determine the minimum age for samples that yielded >25% dispersion. For samples that showed ≤ 25% dispersion, we used the average OSL ages.

Fourteen samples of organic sediments were measured for ^{14}C dating at Beta Analytics Inc., using NEC accelerator mass spectrometers. Given the absence of detrital charcoals and other macrofossils, the bulk organic fraction (carbon content: 0.06–1.62%) smaller than 180 μm, inclusive of humic and humins, was used for dating. $\delta^{13}C$ values were measured separately by Thermo isotope ratio mass spectrometers (IRMS). Conventional radiocarbon ages were calculated using the Libby half-life (5568 years), and were corrected for total isotopic fractionation effects. Errors reported from the laboratory are based on 1-sigma counting statistics. Calibration of the conventional age was performed using the 2013 calibration databases (INTCAL13) (Reimer et al., 2013), high probability density range method, and Bayesian probability analysis (Ramsey, 2009).

4. Results

4.1. Core descriptions

Three sedimentary facies were present within the recovered cores: 1) poorly sorted gravels with silt to sand, interpreted to represent coarse-grained braided channel facies (herein "Facies A"); 2) moderately sorted silt to sand with gravels sandwiched by thin floodplain silts, interpreted to represent fine-grained braided channel facies (herein "Facies B"); and 3) massive, well-sorted clayey silt with bioturbation, alternating redox state and occasional sand beds, interpreted to represent fluvio-lacustrine facies (herein "Facies C"). In all boreholes, Facies A caps the upper section, overlying Facies B and C (Figs. 4–10). Detailed lithological and structural features for each site are described in this section. The recovered gravels are mainly metamorphosed quartz-feldspar-mica sandstone including quartzite. These are similar to typical clasts found in conglomerates of the Upper Siwaliks Group and are likely reworked derived clasts (e.g., Dhital, 2015).

4.1.1 Lakshmi river (Hanging wall)

4.1.1.1 Site P1 (27.03302ºN, 85.87577ºE; total depth of core: 55 mbs)

The recovered sedimentary sequence at Site P1 (0–55 mbs) (Fig. 4a) consists of three beds of 6–11-m-thick, poorly sorted gravels (16 mm < diameter (d) < 256 mm) with a matrix of fine-coarse sand (Fig. 5a), assigned as Facies A, interbedded with 7–11-m-thick moderate-poorly sorted, grayish-orange silt to medium sand, and well-sorted silt (Fig. 5b), assigned as Facies B. These interbeds of coarse and fine sediments are interpreted to represent bedload and suspended load deposits of a braided river system. Well-sorted silts (at 12–14 and 34–35 mbs) are thin, and occur near the base of coarser beds; we interpret these to have floodplain or aeolian origin (Fig. 5b). The sediments are generally massive, and contain occasional rip-up clasts. The presence of oxidized patches and black Fe/Mn oxides in fine-grained sediments indicate moderate pedogenesis/weathering.

4.1.1.2 Site P2 (27.01315°N, 85.85964°E; total depth of core: 45 mbs)

The upper 20 m of sediments at Site P2 (Fig. 4b) consist of mostly poorly sorted gravels (16 mm < d < 128 mm) with variable amounts of fine to coarse sand; these likely represent bedload-dominant channel deposits and are assigned as Facies A. In contrast, the underlying sediments (20–45 mbs) consist of primarily well-sorted clayey silt, with several beds of fine to medium sand containing a few gravel clasts (a few cm to 3 m thick, with the thickest sections at 29–33, 35–38 and 42–45 mbs); this suggests a change in depositional environment (Figs. 5c–h). Bioturbation by burrowing and color mottling associated with an irregular distribution of Fe/Mn oxides are distinct, reflecting pedogenesis (Figs. 5c,d). These sediments are generally massive, occasionally containing rhythmic interbeds of silt and clay (0.2–2 cm thick; Figs. 5e–g). Other sedimentary structures include silty rip-up clasts and silt dikes. These sediments are interpreted to have been deposited in a waterlogged, low-energy lacustrine environment in the vicinity of a channel, with pulses of sandy fluvial inputs and aeolian silts (loess), which we assign as Facies C.

The observed bedding planes are mostly sub-horizontal, dipping between 0° and 10° (Fig. 4b). The interval at 20–29 mbs is characterized by oxidized, dark yellowish orange silty clay with distinct pedogenic features, including rounded mud-filled nodules (Fig. 5h); below 29 mbs, gleyed dark gray sediments are more dominant (Fig. 4b). Gradual alternations between gleyed silty clay and oxidized silty clay are common at 29–34 mbs, implying changes between anaerobic and aerobic conditions (Figs. 5e–g).

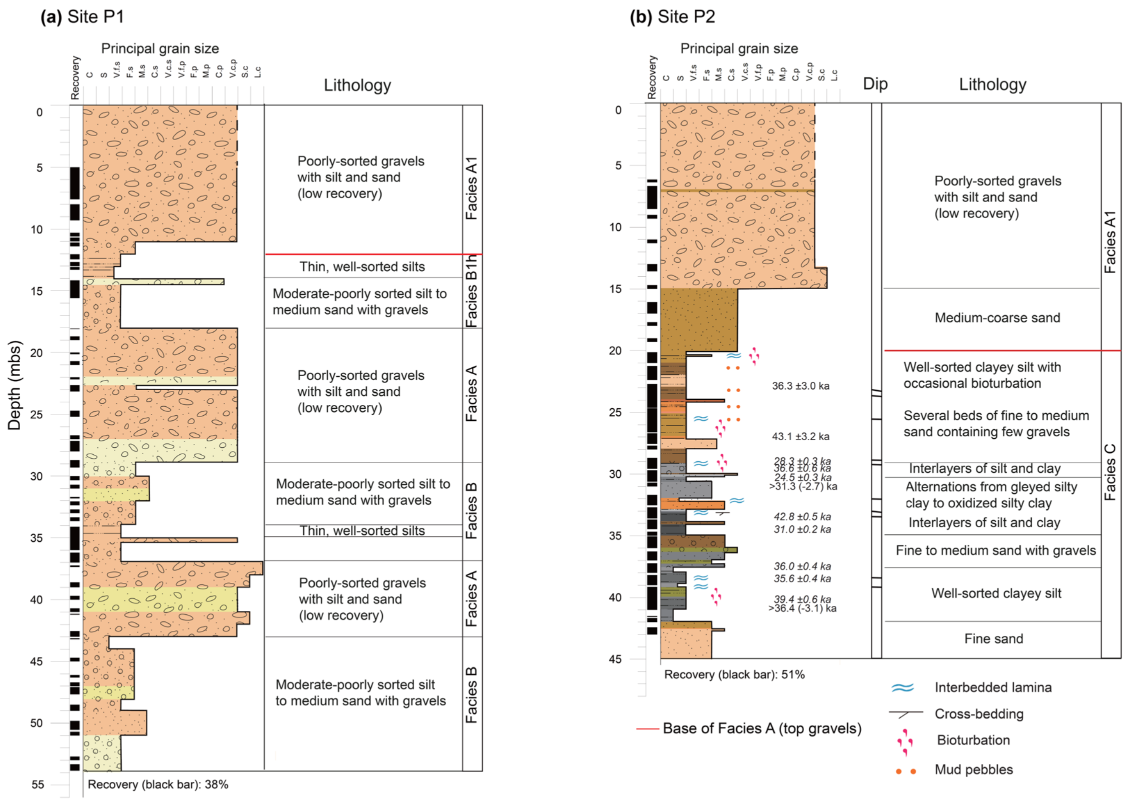

Figure 4. Graphic sedimentary core logs of Lakshmi river Sites P1 and P2 showing principal grain size, sediment color, description of lithology, and bedding dip angle. Black bars represent core recovery (black: recovered). Facies A–C are interpreted facies (see Section 4.2 for details). Red line marks the base of top gravels. (a) Site P1. (b) Site P2. Symbols next to core log described in legend below. Numbers are OSL and radiocarbon (italic) ages at each depth. Age results are detailed in Figure 12 and Tables 1 and 2. Measured dip angles are shown in tilted lines.

363

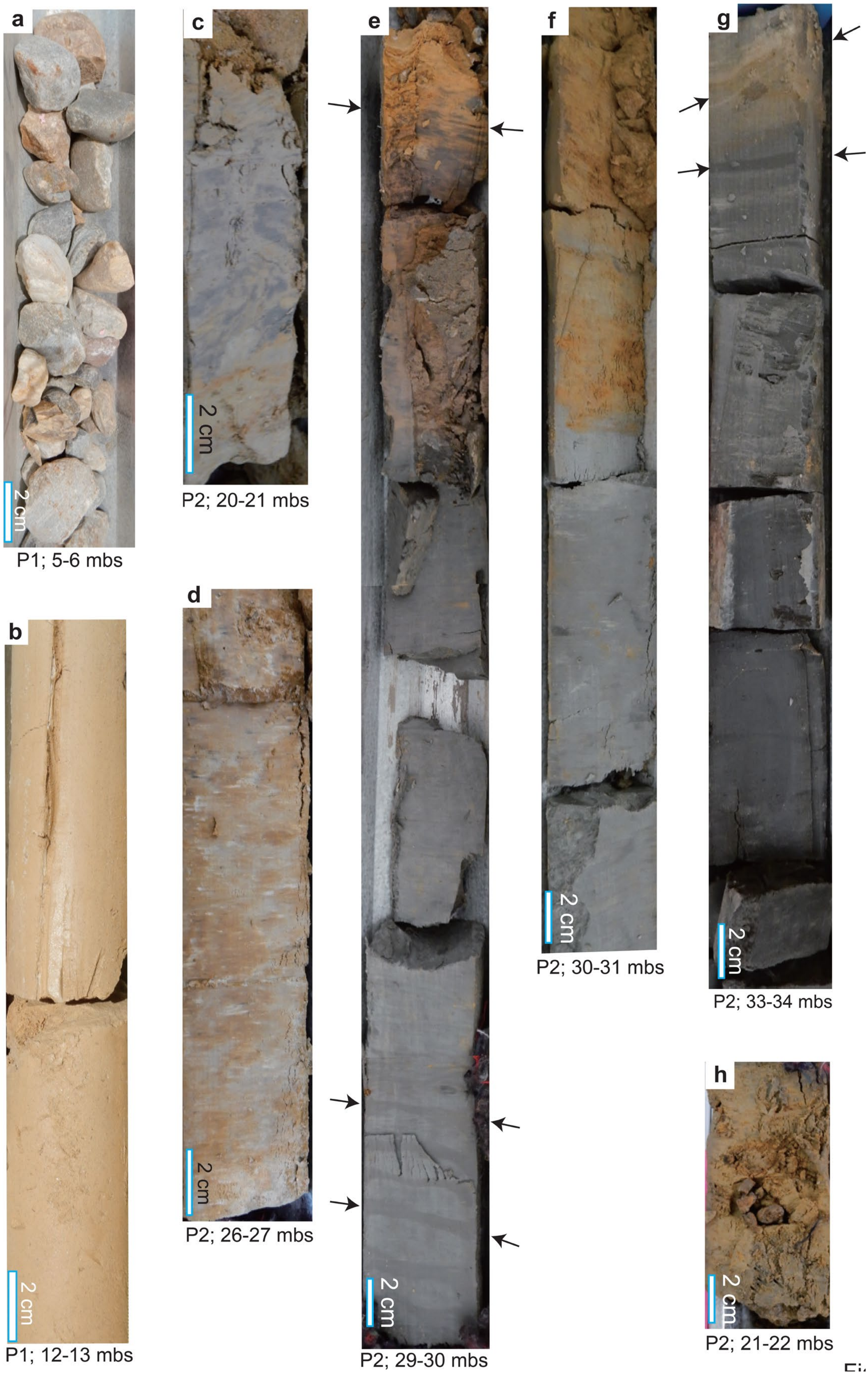
a
2 cm
P1; 5-6 mbs
b
2 cm
P1; 12-13 mbs
c
2 cm
P2; 20-21 mbs
d
2 cm
P2; 26-27 mbs
e
2 cm
P2; 29-30 mbs
f
2 cm
P2; 30-31 mbs
g
2 cm
P2; 33-34 mbs
h
2 cm
P2; 21-22 mbs

Figure 5. Representative features of cores from Lakshmi river Sites P1 and P2. Cores in each image are shallowing upward. (a) Coarse gravels at Site P1; 5–6 mbs. (b) Well-sorted silt at Site P1; 12–13 mbs. (c) Silty clay exhibiting bioturbation at Site P2; 20–21 mbs. (d) Silt with mottled texture interpreted to be paleosol at Site P2; 26–27 mbs. (e) Transition from gleyed to oxidized silty clay, with thin interbeds of silt and clay (marked by arrows) at Site P2; 29–30 mbs. (f) Transition from gleyed clay to oxidized silt at Site P2; 30–31 mbs. (g) Interbeds of silt and clay showing cross-bedding (marked by arrows) at Site P2; 33–34 mbs. (h) Rounded mud-filled nodules observed in silty clay at Site P2; 21–22 mbs.

4.1.2 Bhabsi river (Hanging wall)

4.1.2.1 Site P3 (27.02714°N, 85.88994°E; total depth of core: 50 mbs)

The upper 27 m of sediments at Site P3 (Fig. 6a) are mostly coarse gravels (8 mm < d < 64 mm) with variable amounts of sand, and are assigned as Facies A. Beneath this unit (27–50 mbs, base of core), the sediments are finer grained, characterized by moderately to poorly sorted fine to medium sand with gravels, interbedded with well-sorted silt to clay, assigned as Facies B. The well-sorted fine sediments include brown clay (Fig. 7a), grayish-orange silt, and gleyed clay/silt, interpreted to be of floodplain origin. These sediments are massive and thinly bedded, with no bioturbation, contrasting with the lacustrine sediments at Site P2. A distinct, lithified organic-rich black clay (possibly a paleosol) is present at 40 mbs and coarsens up to fine sand (Fig. 7b). This observed reverse grading was likely caused by a gradual increase in water level during flooding in the overbank (e.g., Iseya, 1989; Rubin et al., 1998; Skolasińska, 2014).

The sediments are generally structureless, occasionally containing rip-up clasts and oxidized spots. Gradual transitions from silt to clay and from sand to silt show wavy contacts that dip 15–30° below 40 mbs (Fig. 6a). Infiltration of roots and organic materials in brown and gleyed clay, together with the distribution of Fe/Mn oxides, indicates pedogenesis.

4.1.2.2 Site P4 (27.01497ºN, 85.88236ºE; total depth of core: 100 mbs)

The upper 42 m of sediments at Site P4 (Fig. 6b) are mostly coarse gravels (16 mm < d < 256 mm) with coarse sand and thin layers of poorly sorted sandy clay with pebbles, representing bedload-dominant channel deposits, assigned as Facies A. From 42–100 mbs (base of the core), the sediments are finer grained, consisting of packages of silt to very coarse sand with gravels, assigned as Facies B (Fig. 7c–f). These sediments generally have normal grading, sandwiched by well-sorted gleyed clayey silt, grayish-orange silt, and/or brown clay, interpreted to be floodplain deposits. Under the microscope, the gleyed sediments contain disseminated pyrite and ferrous minerals that presumably formed under reducing conditions.

Moderate to intense color mottling due to bioturbation and pedogenesis are common in the fine sediments, as are fine-grained rip-up clasts. The sediments are generally massive, except for several horizons of inclined laminas in silty fine sand (Figs. 7c,d), which dip 3–45° below 55 mbs (Fig. 6b). These dips likely reflect local sedimentary processes such as cross-bedding, and/or post-depositional processes such as soft sediment deformation.

4.1.2.3 Site P5 (27.00879ºN, 85.88044ºE; total depth of core: 95 mbs)

The upper 68 m of sediments at Site P5 (Fig. 6c) are mostly coarse gravels (16 mm $< d <$ 256 mm) with variable amounts of silt to coarse sand, occasionally interbedded with poorly sorted silty clay to fine sand with pebbles, assigned as Facies A. From 68–95 mbs (base of the core), the sediments are finer grained, consisting of normally graded, poorly sorted silt to coarse sand with gravels of Facies B (Fig. 7g–i). Inclined laminas in silty fine sand are present, and are mostly oxidized (Fig. 7i). Very well sorted, clayey silt is thinly interbedded between coarser channel deposits, and is interpreted to represent aeolian/floodplain sediment. The dips of these laminas and silt beds range from 5°–65° and 2–30°, respectively (Fig. 6c), and they likely reflect largely local depositional processes such as cross-bedding, and/or post-depositional processes such as soft-sediment deformation.

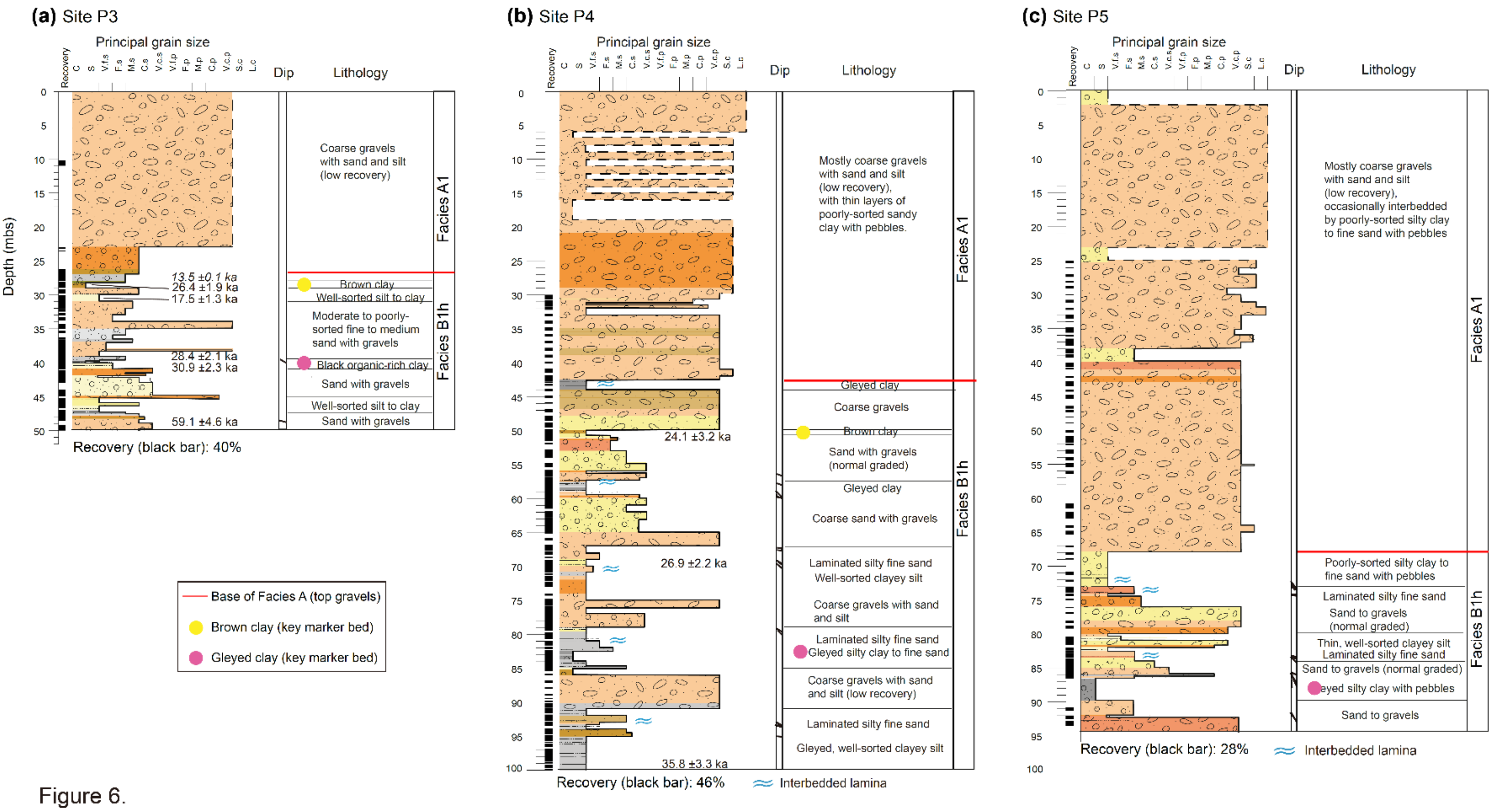

Figure 6.

Figure 6. Graphic sedimentary core logs for Bhabsi river sites (a) P3, (b) P4, and (c) P5 showing principal grain size, sediment color, dip angles and description of lithology. Black bars show recovered core. Symbols next to core log are described in legend below. Dating results are for OSL and radiocarbon (italic) ages. Age results

are detailed in Figure 12 and Tables 1 and 2. Measured dip angles are shown as tilted lines. Facies A and B are interpreted facies (see Section 4.2 for details). Red line marks the base of top gravel section (Facies A1). Brown clay (yellow dots) and gleyed clay (pink dots) are key beds traced in Fig. 14.

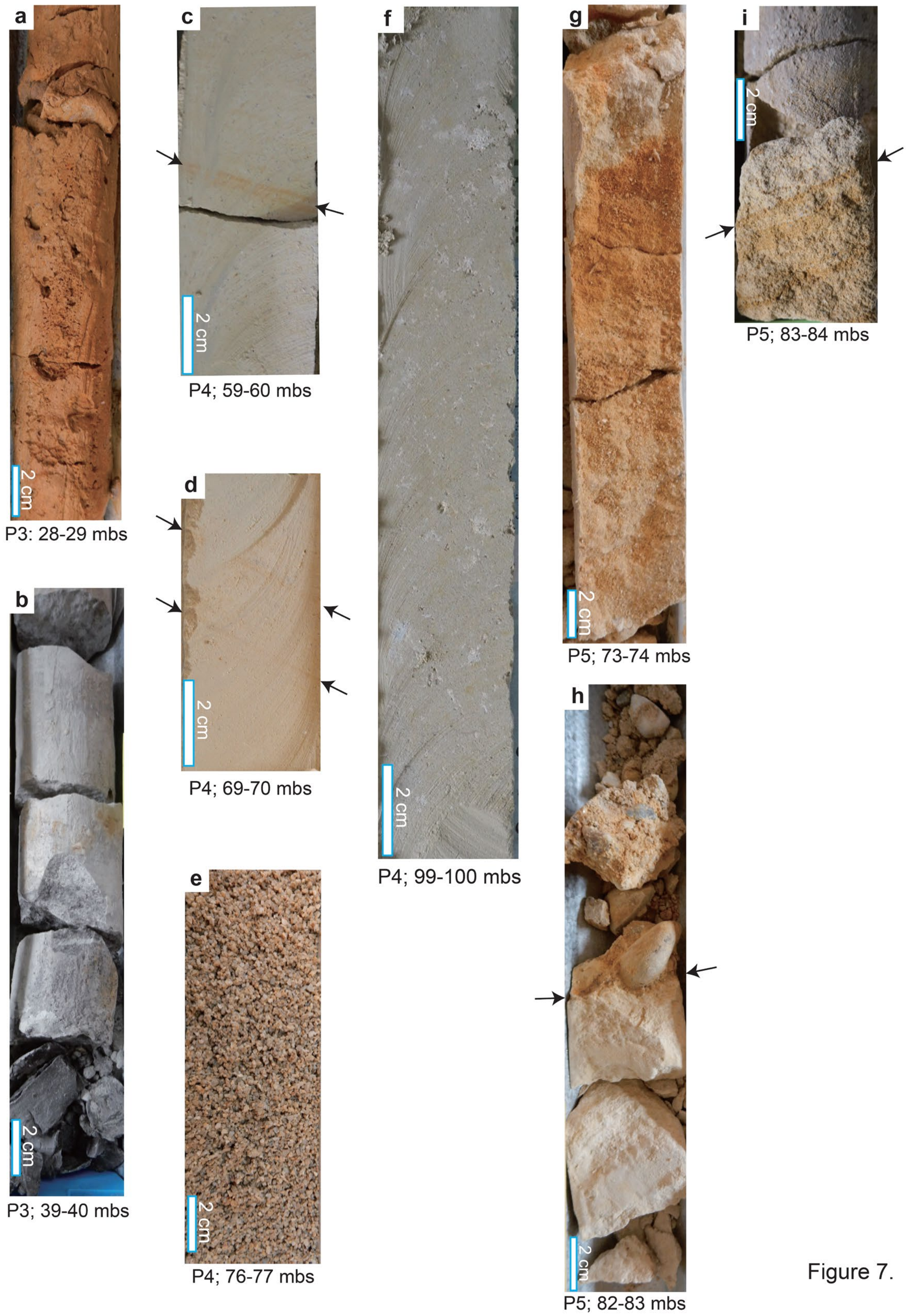

Figure 7.

431

432

Figure 7. Representative features of cores from Bhabsi river Sites P3–P5. Cores in each image shallow upward. (a) Brown clay at Site P3; 28–29 mbs. (b) Black organic-rich clay at Site P3; 39–40 mbs. (c) Inclined lamina in gleyed silt at Site P4; 59–60 mbs. (d) Inclined lamina in grayish orange silt at Site P4; 69–70 mbs. (e) Very coarse sand at Site P4; 76–77 mbs. (f) Gleyed silt at Site P4; 99–100 mbs. (g) Fine to medium sand at Site P5; 73–74 mbs. (h) Erosional contact from silt to gravels recovered at Site P5; 82–83 mbs. (i) Inclined laminas in silty sand at Site P5; 83–84 mbs.

4.1.3 Ratu river (Footwall)

4.1.3.1 Site P6 (26.98673ºN, 85.91089ºE; total depth of core: 50 mbs)

The upper 15 m of sediments at Site P6 (Fig. 8a) are mostly coarse gravels (16 mm < d < 256 mm) with silt to coarse sand, representing bedload-dominant channel deposits, assigned as Facies A (Fig. 9a). From 15 mbs, the sediments are finer grained, characterized by silt and fine to coarse sand of Facies B, intercalated with gravels until 29 mbs. Below this unit, from 29 mbs to the base of the core at 50 mbs, gravel layers are absent, and the sediments consist of moderately sorted, normally graded silt to medium sand (Figs. 10a–f). Color mottling and oxidized spots are common throughout the core, reflecting pedogenesis and bioturbation.

Continuous sub-vertical bedding planes characterize the sediments below 29 mbs, whereas the sediments above dip sub-horizontally (3–25°) (Figs. 8a, 10a–f, 11). The transition occurs around 30–35 mbs, where distinct silt laminas (1–2 mm thick) in well-sorted, indurated sandy silt show an abrupt increase in dip from 30° to 85° (Figs. 10a–e, 11). Within this interval, laminas exhibit several variations of decrease and increase in dip, forming multiple open, recumbent folds (Fig. 11). Below this interval, the sandy beds maintain near-vertical dip (~75–90°) (Figs. 10f, 11).

4.1.3.2 Site P7 (26.98347ºN, 85.91175ºE; total depth of core: 100 mbs)

The upper 17 m of sediments at Site P7 (Fig. 8b) are mostly coarse gravels (16 mm < d < 256 mm) with silt and sand, assigned as Facies A. From 17 to 36 mbs, the sediments become finer grained, consisting of poorly sorted silt with various sand and pebbles intercalated with thin gravels of Facies B. At the bottom of this unit (35–36 mbs), very well sorted, smooth and friable silt suggests aeolian loess. From 36 to 56 mbs, the sediments exhibit mainly coarse gravels, similar to the upper 17 mbs (Facies A) (Fig. 9b).

Below this unit (56–100 mbs), the sediments become finer grained, consisting of normally graded cycles of well sorted clayey silt intercalated with poorly sorted silt to coarse sand with gravels of Facies B (Figs. 9c–e, 10g). 1–2-mm-thick laminas in fine sand and silt are inclined (~15–45°) (Figs. 8b, 10g), and occasionally exhibit cross-bedding (dip 5–40°) (Fig. 9c).

At depths of 66.34–66.42 mbs, distinctive white fine-grained tabular features, identified to be deformation bands, are visible in the middle of a 2-m-thick moderately sorted, medium-coarse grained, massive sand (Fig. 10h–m). The deformation bands are narrow (0.5–3 mm) and cuts across the core and inferred shallow bedding (Fig. 10h, i, m). The bands form a conjugate set dipping 70° and 30°, where the high-angle band is cross-cut by the sub-horizontal band (Fig. 10m). Under a microscope, the deformation band is finer-grained than the host sand and lacks the abundant visible porosity of the host immature arkosic sand (Fig. 10j,k,l). Instead, intergranular space is filled mostly by 50–100 μm angular grains and clay material (Fig. 10k,l). Beneath this interval, sediment lithification continues to increase downhole, as evident in massive gleyed clayey silt below 82 mbs (Fig. 9e) and lithified conglomerates at 95–99 mbs (Fig. 9d).

4.1.3.3 Site P8 (26.97999ºN, 85.90928ºE; total depth of core: 47 mbs)

The upper 18 m of sediments at Site P8 (Fig. 8c) are mostly coarse gravels (16 mm < d < 256 mm) with silt to coarse sand, assigned as Facies A. From 18 to 35 mbs, the sediments are finer grained, consisting of moderately to poorly sorted silt with sand and pebbles, intercalated with thin gravels assigned as Facies B (Fig. 9f). Organic-rich black-brown sandy silt at 19 and 21 mbs is notable. The sediments are generally massive, with several sub-horizontal laminas observed in well sorted silt towards the bottom of the unit (32–35 mbs), possibly representing floodplain deposits or loess (Fig. 9f). These laminas and bedding planes dip 5°–15° (Fig. 8c). From 35 to 47 mbs (base of core), the sediments are mainly coarse gravels of Facies A, similar to the upper 18 mbs.

4.1.3.4 Site P9 (26.97883ºN, 85.90906ºE; total depth of core: 96 mbs)

The upper 28 m of sediments at Site P9 (Fig. 8d) are mostly coarse gravels (16 mm < d < 256 mm) with silt to coarse sand, representing Facies A. From 28 to 41 mbs, sediments become finer grained, consisting of poorly sorted silt to sand with gravels intercalated with well sorted clayey silt, suggesting the channel/floodplain environment of Facies B. The sediments are generally massive and normally graded, with some sub-horizontal wavy laminas in silt at 32–33 mbs (Fig. 9g). Bedding dips 5°–30° (Fig. 8d). Thin layers of organic rich, brown clayey silt also characterize this unit. Color mottling, oxidized spots and irregular layers are present in the fine sediments. At the bottom of this unit, well sorted silt to clay is present (39–41 mbs), with a particularly friable silt at 40–

41 mbs, which is likely aeolian loess. Beneath this unit, from 41 mbs to the base of the core at 96 mbs, the sediments are mainly coarse gravels of Facies A, similar to the upper 28 mbs (Fig. 9h).

4.1.3.5 Site P10 (26.97794ºN, 85.90878ºE; total depth of core: 50 mbs)

The upper 20 m of sediments at Site P10 (Fig. 8e) are mostly coarse gravels (16 mm < d < 256 mm) with silt to coarse sand, representing Facies A. From 20 to 38 mbs, the sediments are finer grained, consisting of well sorted clayey silt intercalated with poorly sorted silt to sand with pebbles and thin gravel layers, assigned as Facies B. Intervals of organic-rich dark brown clayey silt are also distinct (Fig. 9i). Towards the bottom of this unit (36–38 mbs), well sorted, friable to earthy-hard silty clay, possibly aeolian loess, is present. The sediments are generally massive, and color mottling with oxidized spots and organic matter is common. Beneath this unit, from 38 to 50 mbs (base of core), the sediments are mainly coarse gravels of Facies A, similar to the upper 25 m.

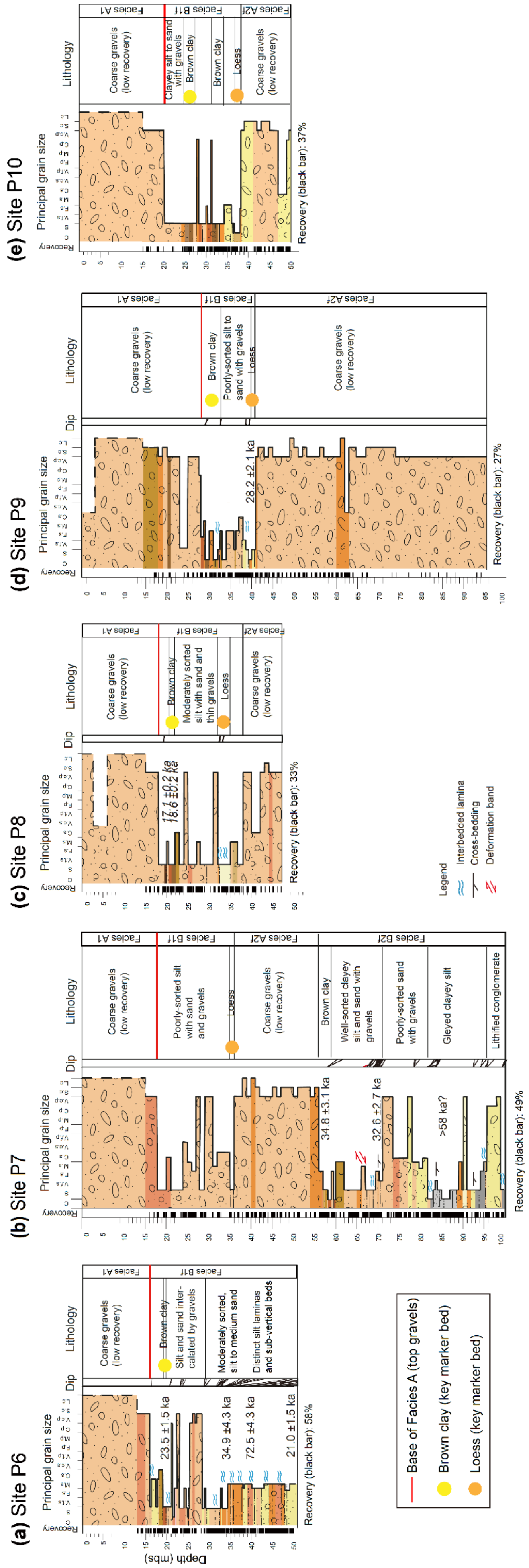
(a) Site P6
(b) Site P7
(c) Site P8
(d) Site P9
(e) Site P10
Principal grain size
Lithology
Dip
Recovery
Depth (mbs)
Coarse gravels (low recovery)
Brown clay
Loess
Facies A1
Facies B1f
Facies A2f
Facies B2f
Recovery (black bar): 58%
Recovery (black bar): 49%
Recovery (black bar): 33%
Recovery (black bar): 27%
Recovery (black bar): 37%
23.5 ±1.5 ka
34.9 ±4.3 ka
72.5 ±4.3 ka
21.0 ±1.5 ka
34.8 ±3.1 ka
32.6 ±2.7 ka
>58 ka?
17.1 ±0.2 ka
18.6 ±0.2 ka
28.2 ±2.1 ka
Base of Facies A (top gravels)
Brown clay (key marker bed)
Loess (key marker bed)
Legend
Interbedded lamina
Cross-bedding
Deformation band

Figure 8. Graphic sedimentary core logs for the Ratu river sites (a) P6, (b) P7, (c) P8, (d) P9, and (e) P10 showing principal grain size, sediment color, dip angles, and description of lithology. Black bars are recovered core. Symbols next to core log are described in legend below. Dating results are for OSL and radiocarbon (italic) ages (also shown in Tables 1 and 2). Measured dip angles are shown as tilted lines. Facies A and B are interpreted facies (see Section 4.2 for details). Red line marks the base of top gravels (Facies A1). Brown clay (yellow dots) and loess (orange dots) are key beds traced in Fig. 15.

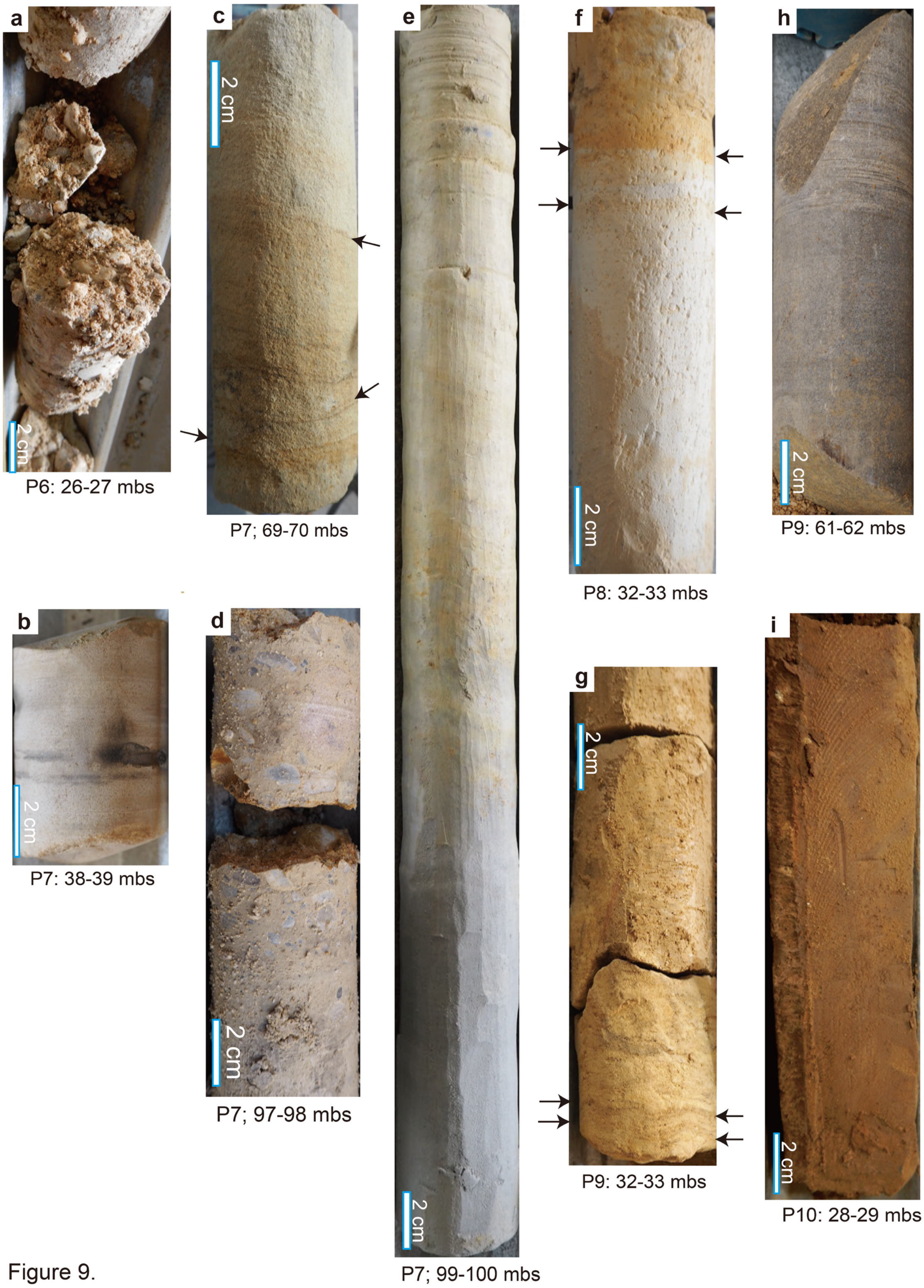

Figure 9.

Figure 9. Representative features of cores for the Ratu river sites P6–P10. Cores in each image shallow upward. (a) Gravels with matrix of sand and silt at Site P6; 26–

27 mbs. (b) Large cobble of quartzite at Site P7; 38–39 mbs. (c) Cross-bedding in silty fine sand at Site P7; 69–70 mbs. (d) Lithified conglomerate at Site P7; 97–98 mbs. (e) Grayish orange silt transitioning into gray silt at Site P7; 99–100 mbs. (f) Sub-horizontal laminas in silt at Site P8; 32–33 mbs. (g) Sub-horizontal laminas in silt at Site P9; 32–33 mbs. (h) Large cobble of sandstone at Site P9; 61–62 mbs. (i) Brown clay at Site P10; 28–29 mbs.

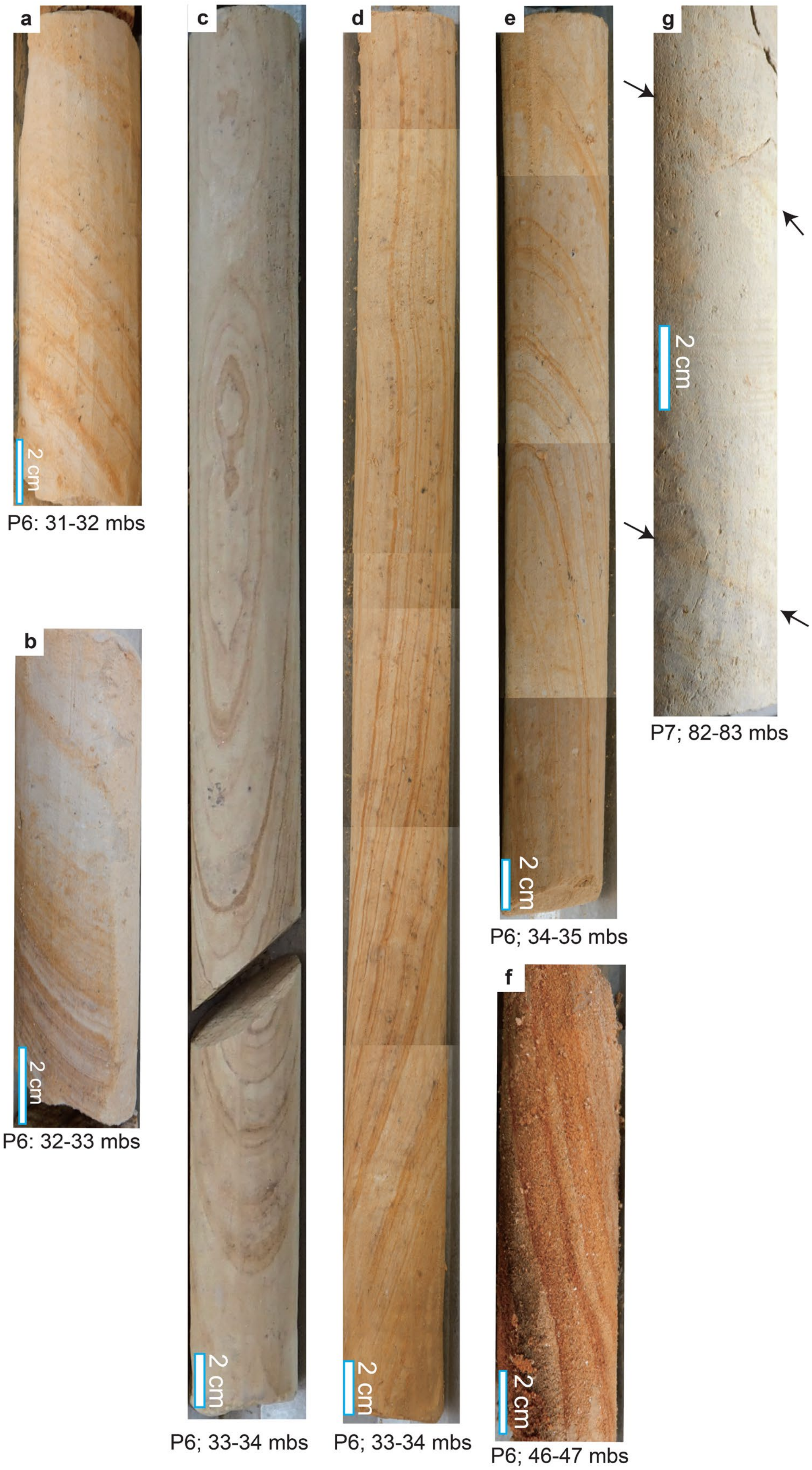
a
2 cm
P6: 31-32 mbs
b
2 cm
P6: 32-33 mbs
c
2 cm
P6; 33-34 mbs
d
2 cm
P6; 33-34 mbs
e
2 cm
P6; 34-35 mbs
f
2 cm
P6; 46-47 mbs
g
2 cm
P7; 82-83 mbs

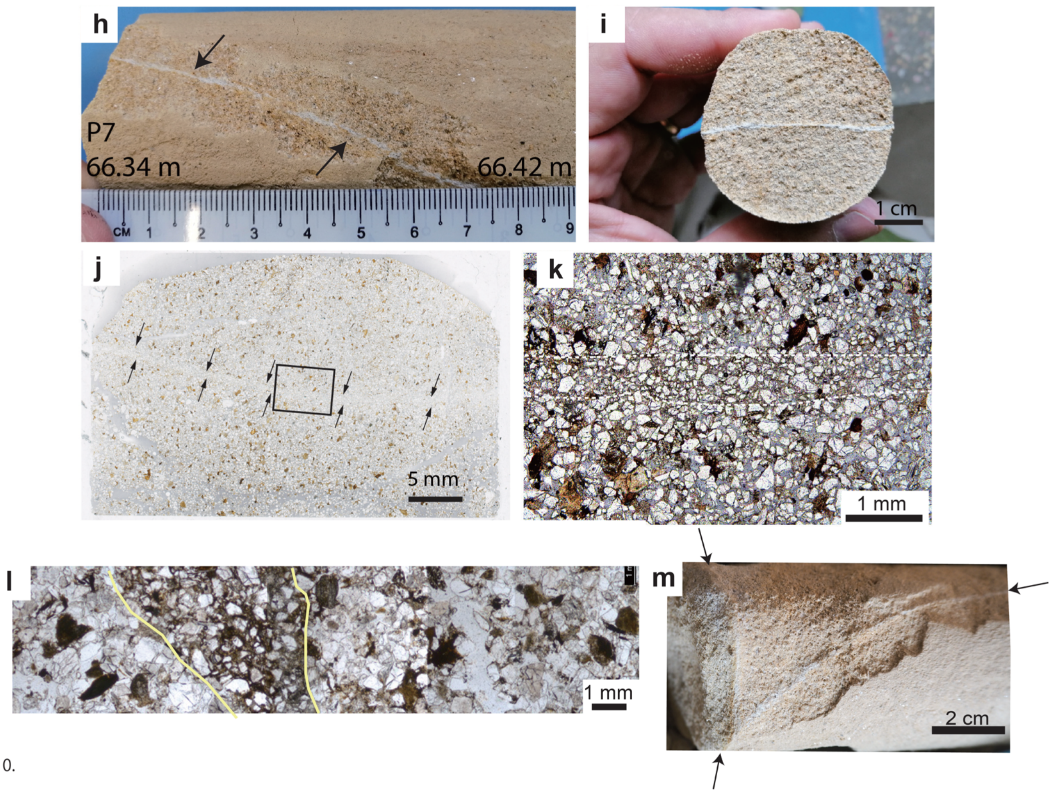

Figure 10.

Figure 10. High-angle bedding and deformation band observed at Sites P6 and P7. Cores in each image shallow upward. (a) Inclined laminas in silt at Site P6; 31–32 mbs. (b) Inclined laminas in silt at Site P6; 32–33 mbs. (c) Near-vertically dipped laminas in silt at Site P6; 33–34 mbs. (d) Same core as (c). (e) Inclined laminas in silt exhibiting gradual increase in dip with depth at Site P6; 34–35 mbs. (f) Near-vertically dipped laminas in medium sand at Site P6; 46–47 mbs. (g) Inclined laminas in silt at Site P7; 82–83 mbs. (h) Deformation band observed in medium-coarse sand at Site P7; 66.34–66.5 mbs. Deformation band is white (marked by arrows), and dip is steep. (i) Same core as (h), viewed uphole at 66.35 mbs. (j) High-resolution scan of thin section of core cut perpendicular to plane of deformation

band. Section epoxy is stained weakly blue to show porosity. Note finer grain size and whiter color of deformation band (arrows) relative to matrix. White box show area of (k). (k) Plane polarized photomicrograph of inset box shown in (j). Epoxy is stained light blue to show porosity. Note porosity reduction and grain size reduction within deformation band (central region highlighted with dashed lines). (l) Close-up of plane polarized photomicrograph of deformation band without epoxy from another thin section. Yellow line marks the top and bottom of the deformation band. (m) Deformation bands observed in conjugate set. Same location as (h).

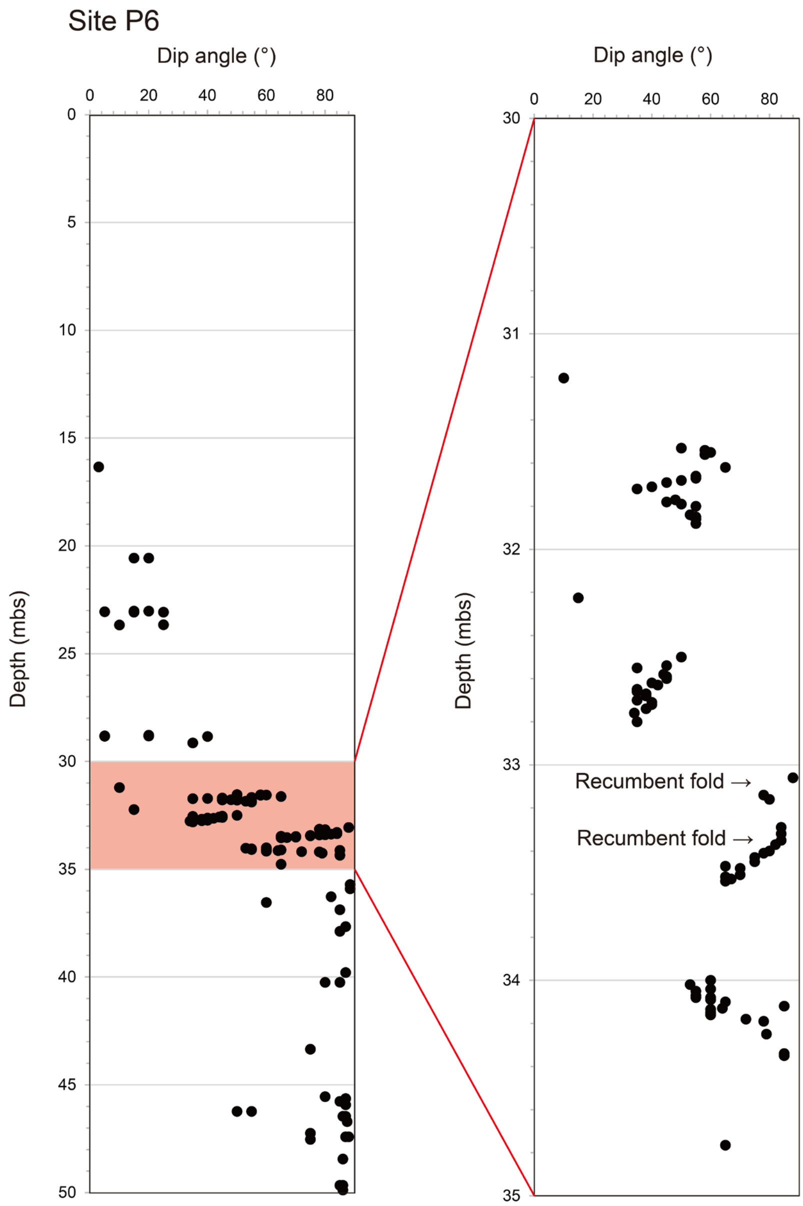

Figure 11. Distribution of dip angles measured at Site P6. The right panel shows close-up of 30–35 mbs, shaded in red in the left panel. Two recumbent folds are identified between 33–33.6 mbs, owing to continuous core recovery (see Figs. 9c,d).

4.2. Sediment ages, marker beds, and timing of facies transitions

Sediment ages from Sites P2–P4 and P6–P9 were determined from 18 samples by OSL dating and 14 samples by ^{14}C dating (Figs. 4, 6, 12, Tables 1, 2). The ages span from 13.5±0.1 to 72.5±4.3 ka. Based on our stratigraphic observations (Section 4.1) and the recovered ages, we infer the timing of facies transitions. Despite the variations in deposition and sediment thickness observed in each river, we are able to correlate the major facies transitions among them. We also identify several key lithologies that can be correlated across the different sites and across different rivers: brown clay, gleyed clay/silt, and well-sorted aeolian silt (loess). Together, this information is used to construct a regional cross-section and timing of events in Section 5.

Figure 12 shows the ^{14}C and OSL ages at Sites P2 and P3. The overall ranges of ages obtained by the two methods are similar (Fig. 12). However, there is a wide scatter in dates that cannot be explained by the reported uncertainties from either method. This may be related to specific challenges associated with each dating method, such as reworking of organic material, and partial bleaching and/or saturation (all OSL electron traps have become filled, and no further charge is trapped in the sample) of quartz sands. For example, the gleyed clay at 40 mbs at Site P3 yielded older ^{14}C ages (38.7–41.5 ka) than the OSL data both above and below (30.9±2.3 ka) (Figs. 6a, 12b). This could be explained by the clay containing reworked old residual carbon (e.g., Wu et al., 2011; Reuther et al., 2017). Due to this possibility, we prefer the OSL age over the ^{14}C age for this section, since the OSL ages are internally consistent. We also note that the OSL ages obtained at 30.9 mbs and 40.9 mbs are >31.3 and >36.4 ka, respectively, at Site P2 represent lower limits (Fig. 12a), since the OSL responses for the obtained equivalent doses are approaching saturation and reaching the limit of detection; these ages therefore have infinite positive error bars (Supporting Information Fig. S5).

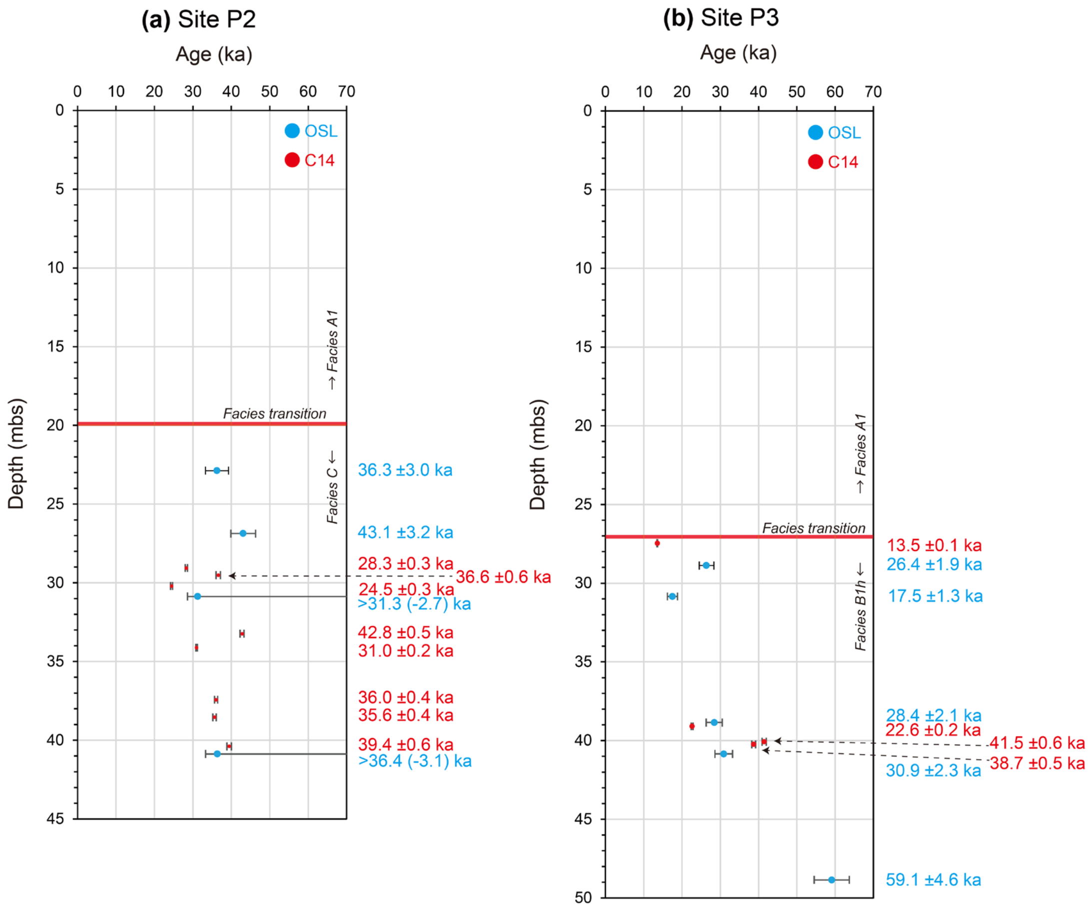

Figure 12. Sediment ages from Sites P2 and P3 (also see Tables 1, 2). Blue dots: OSL dating. Red dots: 14C dating. Age values are given next to each data point (blue: OSL, red: 14C). Orange line marks the lithologic base of Facies A1 (see Figs. 3 and 5). Error bars for OSL include dose rate errors and uncertainty for equivalent dose. Error bars for 14C are 1σ counting statistics. (a) Site P2. (b) Site P3.

The first marker bed is the brown clay in Facies B, which is observed both in the hanging wall (28 mbs at Site P3 and 50 mbs at Site P4) and in the footwall (20–30 mbs at Sites P6–P10), and has a sediment age of 17.5–26.4 ka (Figs. 6, 8). In the hanging wall, the brown clay is dated between 13.5–26.4 ka (Site P3, ^{14}C and OSL ages above and below) and 24.1±3.2 ka (Site P4, OSL) (Fig. 6; Tables 1, 2). In the footwall, the brown clay is dated at 23.5±1.5 ka (Site P6, OSL) and 17.1±0.2 to 18.6±0.2 ka (Site P8, ^{14}C) (Fig. 8; Tables 1, 2).

The second marker bed is the gleyed clay in Facies B in the hanging wall, identified at 39–40 mbs at Site P3, 80–85 mbs at Site P4, and 86–90 mbs at Site P5 (Fig. 6). The gleyed clay is dated at 30.9±2.3 ka (Site P3, OSL) and between 26.9 and 35.8 ka (Site P4, OSL ages above and below) (Fig. 6; Table 2).

The third marker bed is the loess in the footwall, identified at 35–36 mbs at Site P7, 32–35 mbs at Site P8, 39–41 mbs at Site P9, and 36–38 mbs at Site P10 (Fig. 8; Section 4.1). This loess is dated at 28.2±2.1 ka by OSL methods at Site P9 (Fig. 8; Table 2).

The obtained sediment ages also constrain the timing of the observed facies transitions (Section 4.1). The youngest and clearest facies transition that we identify occurs between the upper Facies A, which encompasses the upper part in all boreholes, and the Facies B section beneath it (observed in all but Site P2, which has Facies C below Facies A). Here, we name the upper Facies A that is common in all boreholes as “Facies A1,” and the Facies B below Facies A1 as “Facies B1h” and “Facies B1f” in the hanging wall and footwall of the Bardibas thrust, respectively (Figs. 4, 6, 8). We do not have any dates from Facies A1 as it is not suitable for dating (coarse gravels with very low recovery), but the nearest sample below the facies transition is obtained at 27 mbs at Site P3 and has an age of 13.5±0.1 ka (^{14}C); this represents a maximum age for the transition into Facies A1 (Fig. 12b).

The facies transition at Site P2, from Facies C (lacustrine) below to Facies A1 above, is poorly dated. However, within Facies C at this site, we dated eight samples by ^{14}C and four by OSL methods (Fig. 12a). The ages are scattered and do not exhibit a strong relationship with depth, but in general range from 24.5 ± 0.3 to 43.1 ± 3.2 ka (Fig. 4b, 12a, Tables 1, 2); these sediments are older than the Facies A/B transition (13.5±0.1

ka) estimated at Site P3.

The base of Facies B1, which is buried beneath Facies A1, is best observed in the footwall. At Sites P7–P10, the base of Facies B1f is marked by the loess marker bed (28.2±2.1 ka), and we consider this age to represent the timing of this transition (Fig. 8). Beneath this unit at these sites, we observe a coarse-grained sequence assigned as Facies A and an underlying fine-grained sequence of Facies B in the footwall (Sites P7–P10). Here we name these second sequences of Facies A and B in the footwall as "Facies A2f" and "Facies B2f", respectively (Figs. 4, 6, 8). At Site P7, we obtained an OSL age of 34.8±3.1 ka at the base of Facies A2f at 56.6 mbs, and 32.6±2.7 ka at 70.9 mbs within Facies B2f (Fig. 8; Table 2). Below this depth, age constraints are poor: we have an estimate age of >58 ka at 85 mbs at Site P7 by OSL, but we are reluctant to use this age as there were not sufficient quartz aliquots for this sample (only 8; Table 2). At Site P6, OSL ages of Facies B1f at 30–50 mbs include some older ages than Facies B1f at Sites P7–P10, ranging from 21.0 to 72.5 ka (Fig. 8, Table 2). The large scatter in ages at Site P6 may be due to disturbance by the deformation that produced the sub-vertical beds (~75°–90°) that characterize this section below 29 mbs (Fig. 11).

These deeper facies transitions recorded in the footwall (associated with Facies A2f and B2f) are not well observed in the hanging wall (Sites P1–P5), despite the fact that the dated ages show that the sediments cover the same age range (Figs. 4, 6, 8). In particular, the deep sediments of Facies B1h (59.1±4.6 ka; Site P3) and Facies C (43.1±3.2 ka; Site P2) in the hanging wall are older than the base of Facies B1f (28.2±2.1 ka; Site P9) in the footwall (Figs. 4, 6, 8; Table 2). This may be the result of different facies being active in different locations; alternatively, some sedimentary sections may not be preserved in the hanging wall due to different rates of uplift/subsidence, and/or there could be poor recovery of some sections in the hanging wall. It is likely that Facies B1h corresponds to both Facies B1f and B2f, with a missing or very thin or poorly recovered section of Facies A2f in between (Figs 4, 6, 8).

Table 1

Site	Depth (mbs)	Lithology	Dated material	Conventional radiocarbon age (ka) (1σ)	Calendar calibrated age (ka) (higher probability)*	Calendar calibrated age (ka) (lower probability)**	Stable isotope δ13C (‰)	Carbon content (%)
P2	29.05-29.07	Brown silt	Organic sediment	24.26 ± 0.09	28.600 - 28.005	28.459 - 28.150	-14.4	0.27
P2	29.5-29.54	Gray silty clay	Organic sediment	32.59 ± 0.19	37.144 - 36.023	36.714 - 36.243	-17	0.19
P2	30.2-30.21	Gray clay	Organic sediment	20.36 ± 0.06	24.751 - 24.202	24.544 - 24.327	-16.9	0.09
P2	33.23-33.24	Black silty clay	Organic sediment	38.87 ± 0.36	43.323 - 42.272	43.027 - 42.516	-11	1.2
P2	34.1-34.15	Black silt	Organic sediment	26.81 ± 0.11	31.147 - 30.762	31.061 - 30.865	-13.2	0.5
P2	37.42-37.43	Dark gray medium sand	Organic sediment	32.15 ± 0.18	36.428 - 35.617	36.260 - 35.850	-13.6	0.5
P2	38.53-38.55	Black silt	Organic sediment	31.75 ± 0.17	36.092 - 35.201	35.888 - 35.426	-13.6	0.3
P2	40.37-40.4	Black silt	Organic sediment	34.91 ± 0.24	40.038 - 38.826	39.745 - 39.110	-12.5	0.4
P3	27.45-27.48	Gray silty sand	Organic sediment	11.72 ± 0.04	13.615 - 13.442	13.703 - 13.681	-17.7	0.2
P3	39.09-39.1	Grayish orange silt	Organic sediment	18.76 ± 0.06	22.830 - 22.434	22.693 - 22.491	-18.2	0.07
P3	40-40.15	Black clay	Organic sediment	36.9 ± 0.31	42.016 - 40.904	41.775 - 41.236	-13.3	1.4
P3	40.23-40.25	Gray silt	Organic sediment	34.16 ± 0.22	39.213 - 38.216	38.870 - 38.435	-14.7	0.3
P8	19.82-19.87	Brown silt	Organic sediment	14.06 ± 0.04	17.330 - 16.882	17.185 - 16.996	-11.4	0.52
P8	21.47-21.49	Brown silt	Organic sediment	15.34 ± 0.06	18.765 - 18.462	18.700 - 18.547	-12.3	1.62

Calibration of the conventional age were performed using the INTCAL13 (2013 calibration databases) (Reimer et al. 2013), high probability density range method and Bayesian probability analysis (Ramsey, 2009). For sediment age, we use the higher probability calendar-calibrated age.

* 95.4% probability density range for all samples except for P3 27.45-27.48 mbsf, which is 94.1% probability.

** 68.2% probability density range for all samples except for P3 27.45-27.48 mbsf, which is 1.3%.

Table 1. Summary of radiocarbon dating results from Sites P2–P8 showing sample location, lithology, dated material, conventional radiocarbon age, calendar calibrated age, δ13C (‰), and carbon content. See more details in Supporting Information Text S2.

Table 2.

Site	Depth (mbs)	Lithology	U[a] (ppm)	Th[a] (ppm)	K[a] (%)	Rb[a] (ppm)	Cosmic[b, c] (Gy/ka)	Dose-rate[b, c, d] (Gy/ka)	n[e]	Average equivalent dose[f] (Gy)	Weighted average equivalent dose[h] (Gy)	2-mixed model equivalent dose[i] (Gy)	Average OSL Age[f,j,] (ka)	Weighted average OSL Age[h,j] (ka)	2-mixing model OSL Age[h,i,j] (ka)
P2	22.75-23	Silt with fine sand	3.4	19.5	1.62	42	0.026±0.003	3.44±0.20	30(60) [6]	124.8±7.3	102.0±1.9	99.2±2.0 (21%)	**36.3±3.0**	29.6±1.8	28.8±1.8
P2	26.75-27	Silt with medium sand	3.9	17.4	1.44	182	0.021±0.002	3.24±0.19	26(60) [13]	139.5±6.3	114.07±2.6	99.0±3.5 (19%)	**43.1±3.2**	35.2±2.2	30.6±2.1
P2	30.75-31	Clayey silt with very fine sand	4.4	20.2	1.68	42	0.017±0.002	3.73±0.22	14(48) [14]	>116.9±7.2	>101.3±5.1	107.6±5.7 (6%)	**>31.3±2.7**	>27.2±2.1	28.8±2.3
P2	40.75-41	Silt with fine sand	4.1	18.5	1.54	175	0.011±0.001	3.43±0.20	15(48) [13]	>124.9±7.8	>93.9±3.6	78.6±4.5 (24%)	**>36.4±3.1**	>27.4±1.9	22.9±1.9
P3	28.75-29	Clay	4.6	16.7	1.39	138	0.019±0.002	3.29±0.20	25(60) [7]	183.3±19.1	102.5±3.0	86.9±3.5 (35%)	55.7±6.7	31.2±2.1	**26.4±1.9**
P3	30.7-31	Silt	3.9	17.7	2.20	155	0.02±0.002	3.94±0.24	34 (29) [70]	133.84±9.1	79.9±1.8	69.1±2.6 (34%)	34.0±3.1	20.3±1.3	**17.5±1.3**
P3	38.7-39	Silt with very fine sand	5.6	15.0	2.04	135	0.02±0.002	3.98±0.24	10 (2) [32]	113.0±5.0	104.2±3.7	73.7±2.9 (11%)	**28.4±2.13**	26.2±1.8	
P3	40.7-41	Gleyed silt with fine sand	3.6	16.8	1.53	97	0.02±0.002	3.21±0.19	30 (4) [52]	175.1±12.1	119.9±3.0	98.9±4.2 (36%)	54.6±5.0	37.4±2.4	**30.9±2.3**
P3	48.7-49	Medium sand with silt	4.3	17.0	2.13	141	0.02±0.002	3.91±0.24	39 (11) [58]	231.2±11.1	193.4±3.9	186.6±5.0 (21%)	**59.1±4.6**	49.5±3.2	47.7±3.2
P4	50.75-51	Brown silt	3.7	15.9	1.32	163	0.007±0.001	2.98±0.18	18(48) [10]	128.1±9.3	94.2±3.6	71.9±8.5 (26%)	43.0±4.1	31.6±2.3	**24.1±3.2**
P4	69.75-70	Silt with fine sand	4.7	22.1	1.83	146	0.004±0.000	4.04±0.24	22(48) [18]	185.8±13.0	143.69±4.0	108.8±5.9 (28%)	46.0±4.2	35.6±2.3	**26.9±2.2**
P4	99.75-100	Clayey silt	3	16.4	1.36	120	0.002±0.000	2.90±0.17	26(48) [2]	103.8±7.5	86.0±1.4	89.5±1.4 (14%)	**35.8±3.3**	29.6±1.8	30.9±1.9
P6	19.75-20	Brown clayey silt	2.2	11	0.91	123	0.034±0.003	2.02±0.12	26(48) [0]	62.9±3.9	53.0±0.7	47.4±0.93 (29%)	31.1±2.7	26.2±1.6	**23.5±1.5**
P6	33.75-34	Silt with fine sand	3.2	14.5	1.20	131	0.015±0.002	2.69±0.16	11(48) [11]	93.8±10.1	85.4±3.0	51.0±6.4 (24%)	**34.9±4.3**	31.7±2.2	19.0±2.6
P6	39-39.25	Fine to medium sand	1.9	9.3	0.77	100	0.012±0.001	1.70±0.10	10(16) [6]	164.0±17.8	129.67±4.7	123.3 ±6.0 (27%)	96.4±11.9	76.3±5.3	**72.5±4.3**
P6	49.75-50	Fine to medium sand with silt	2.1	11.1	0.92	123	0.008±0.001	1.98±0.12	54(76) [1]	80.0±4.3	47.9±0.7	41.5±1.7 (34%)	40.4±3.3	24.2±1.5	**21.0±1.5**
P7	56.5-56.75	Fine sand with silt	3.3	16.4	1.36	98	0.006±0.001	2.97±0.18	18(48) [16]	103.3±6.6	89.4±2.4	78.0±3.9 (24%)	**34.8±3.1**	30.1±2.0	26.3±2.1
P7	70.75-71	Silt to fine sand	3.2	15.5	1.29	103	0.004±0.000	2.81±0.17	32(48) [6]	91.6±5.2	74.1±1.2	74.6±1.3 (25%)	**32.6±2.7**	26.4±1.6	26.5±1.6
P7	84.75-85	Silt	3.1	15.5	1.29	175	0.003±0.000	2.79±0.17	8	>150			**> 58**		
P7	99.75-100	Silt	5.9	17.7	1.47	106	0.002±0.000	3.68±0.22		No quartz					
P9	31.75-32	Clay	2.4	14.8	1.23	113	0.016±0.002	2.57±0.15		No quartz					
P9	40.75-41	Silt	2.2	12.4	1.03	108	0.011±0.001	2.19±0.13	27(48) [3]	61.8±2.9	53.1±0.9	46.4±1.5 (22%)	**28.2±2.1**	24.3±1.5	21.2±1.4

[a] Elemental concentrations from ICP-MS of whole sediment measured at Activation Laboratories Limited Ancaster, Ontario Canada.
[b] Estimated fractional day water content for whole sediment is taken as 10% and with an uncertainty of ± 5%.
[c] Estimated contribution to dose-rate from cosmic rays calculated according to Prescott and Hutton (1994). Uncertainty taken as ±10%.
[d] Total dose-rate from beta, gamma and cosmic components. Beta attenuation factors for U, Th and K compositions incorporating grain size factors from Mejdahl (1979). Beta attenuation factor for Rb is taken as 0.75 (cf. Adamiec and Aitken, 1998). Factors utilized to convert elemental concentrations to beta and gamma dose rates from Adamiec and Aitken (1998) and beta and gamma components attenuated for moisture content. Dose rates calculation was confirmed using the Dose Rate and Age Calculator (DRAC) of Duncan et al. (2015).
[e] Number of replicated equivalent dose (D_E) estimates used to calculate D_E. These are based on recuperation error of < 10%. Number is parentheses is the number of saturated aliquots.The number in the square parentheses is the total measurements made including failed runs with unusable data.
[f] Average equivalent dose (D_E) determined from replicated single-aliquot regenerative-dose (SAR; Murray and Wintle, 2000) runs. The uncertainty is the standard error and includes an uncertainty from beta source estimated of ±2.5%.
[h] Weighted average equivalent dose (D_E) determined from replicated single-aliquot regenerative-dose (SAR; Murray and Wintle, 2000) runs. The uncertainty is the standard error and includes an uncertainty from beta source estimated of ±2.5%.
[i] Age based on minimum population in 2-mixing model using the program of Vermeesch (2009). Values in parentheses are the dispersion of the aliquots.
[j] Uncertainty incorporate all random and systematic errors, including dose rates errors and uncertainty for the $D_{E.}$

In this study, we use average OSL ages for samples that showed ≤ 25% dispersion of the aliquots, and 2-mixing model OSL ages for samples that yielded > 25% dispersion. Preferred ages are highlighted in bold.

Table 2. Summary of OSL dating results from Sites P2, P3, P4, P6, P7 and P9 showing sample location, lithology, radioisotope concentration, moisture contents, total dose rates, equivalent dose estimates and optical ages. Dose rate and age calculations follow the details indicated in the footnote. See more details in Supporting Information Text S1.

5. Discussion

5.1. Shallow structure of the Bardibas thrust

The Bardibas thrust is characterized by a hanging wall anticline composed of Siwaliks bedrock beveled by erosion and buried by ~100 m of more recent sediments (Fig. 3). Sediment cores in this study reveal that a ~15–68-m-thick gravel sequence (Facies A1) was deposited during the latest Pleistocene to Holocene, capping both the hanging wall and footwall (Section 4.1). Near the fault tip, displacement by the thrust is accommodated by a tip-line fold or fault-propagation fold, deforming the syntectonic strata in the footwall (Fig. 3a).

We construct cross-sections across the Bardibas thrust by placing the boreholes presented here onto the seismic profiles of Almeida et al. (2018; and unpublished data;

Figs. 13–15). We also compare our data with the refraction velocity models of Liu et al. (2020), which were developed from the same raw data as the seismic profiles of Almeida et al. (2018; Figs. 3b, 16). We first document the shallow structures surrounding the hanging wall anticline beneath the Lakshmi and Bhabsi rivers, using the stratigraphy from Sites P1–P5. We then constrain the shallow structures around the fault tip and growth strata in the footwall beneath the Ratu river, using the stratigraphy from Sites P6–P10. These comparisons, together with sediment ages, allow us to infer the shortening of the hanging wall anticline, and the uplift of the hanging wall of the Bardibas thrust relative to the footwall.

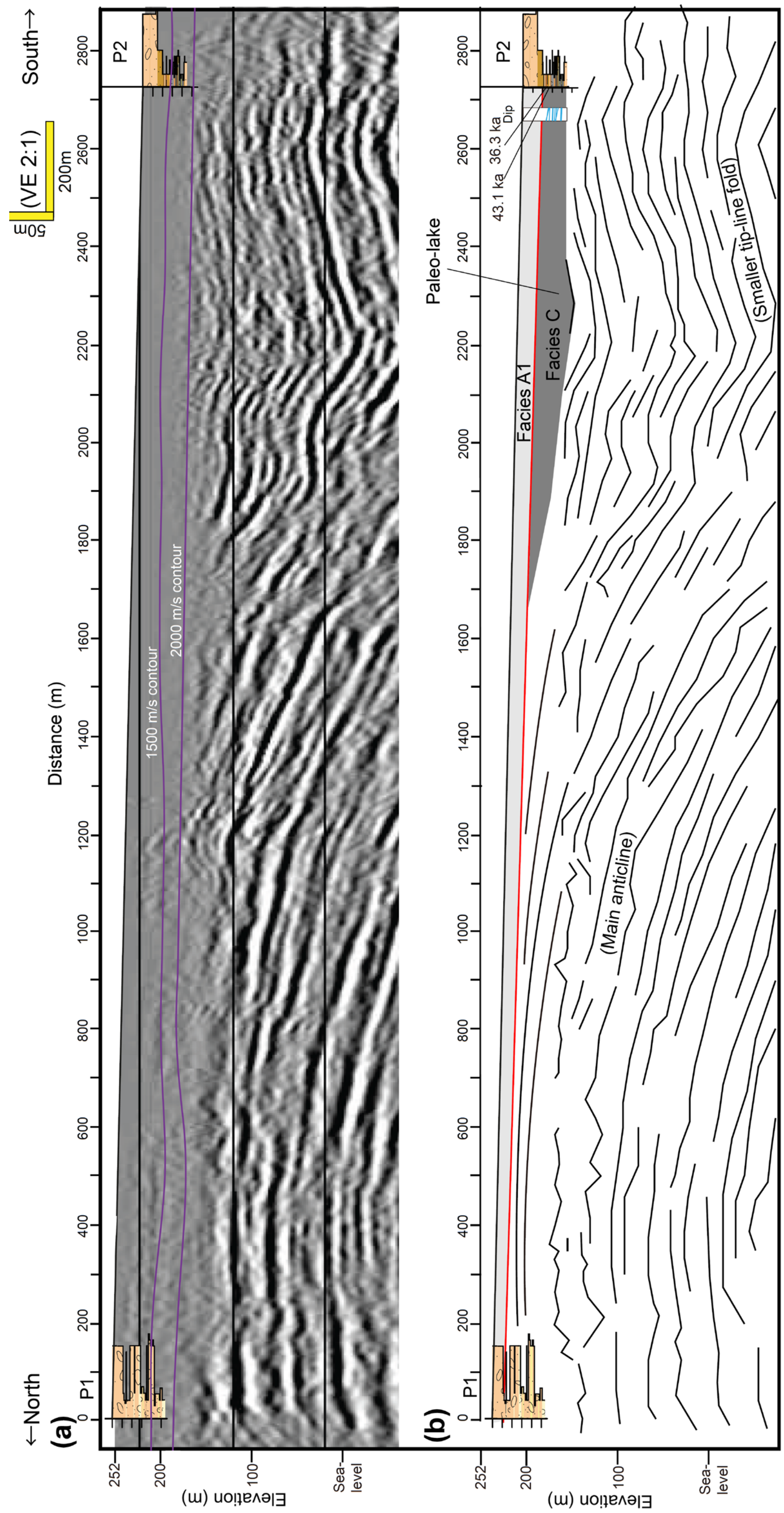

Figure 13. Lakshmi river cross-section. (a) Graphic sedimentary core logs of Sites P1 and P2 placed in seismic reflection profile of Almeida et al. (unpublished data).

Vertical exaggeration=2:1. (b) Interpretation of (a) with colored Facies A1 (light gray) and Facies C (dark gray). Red line marks the base Facies A1. Measured dip angles from the cores at Site P2 are shown in blue bars, vertically exaggerated (2:1). Representative ages obtained at Site P2 are shown next to core log (also see Fig. 12; Table 1). The hanging wall anticline of the Bardibas thrust is observed at depth, with a small syncline between the south-dipping forelimb of the main anticline and a north-dipping limb of smaller tip-line fold of a southern splay, creating a local lacustrine depocenter.

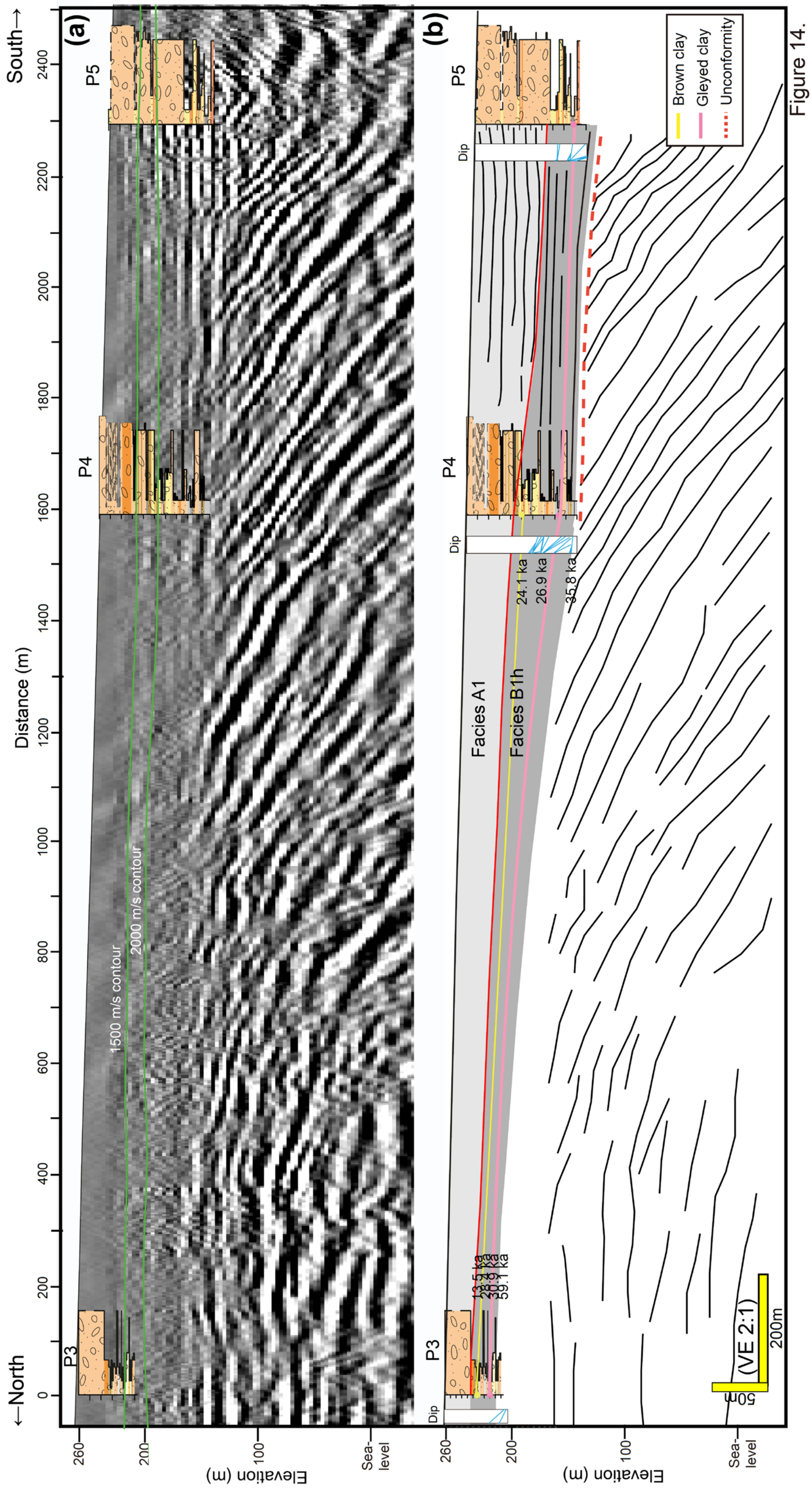

Figure 14. Bhabsi river cross-section. (a) Graphic sedimentary core logs of Sites P3–

P5 placed on seismic reflection profile of Almeida et al. (2018). The hanging wall anticline of the Bardibas thrust is observed at depth (tilted strata). Vertical exaggeration=2:1. (b) Interpretation of (a) with colored Facies A1 (light gray) and Facies B (dark gray). Red line marks the base of Facies A1 at 27–68 mbs. The seismically imaged angular unconformity (marked by red dashed line) between the tilted sediments and relatively younger sediments (colored in gray). Measured dip angles from the cores are shown in blue bars, vertically exaggerated (2:1). Marker beds of brown clay (yellow dots and lines) and gleyed clay (pink dots and lines) are traced and their ages are shown next to graphic logs (also see Fig. 12; Tables 1, 2).

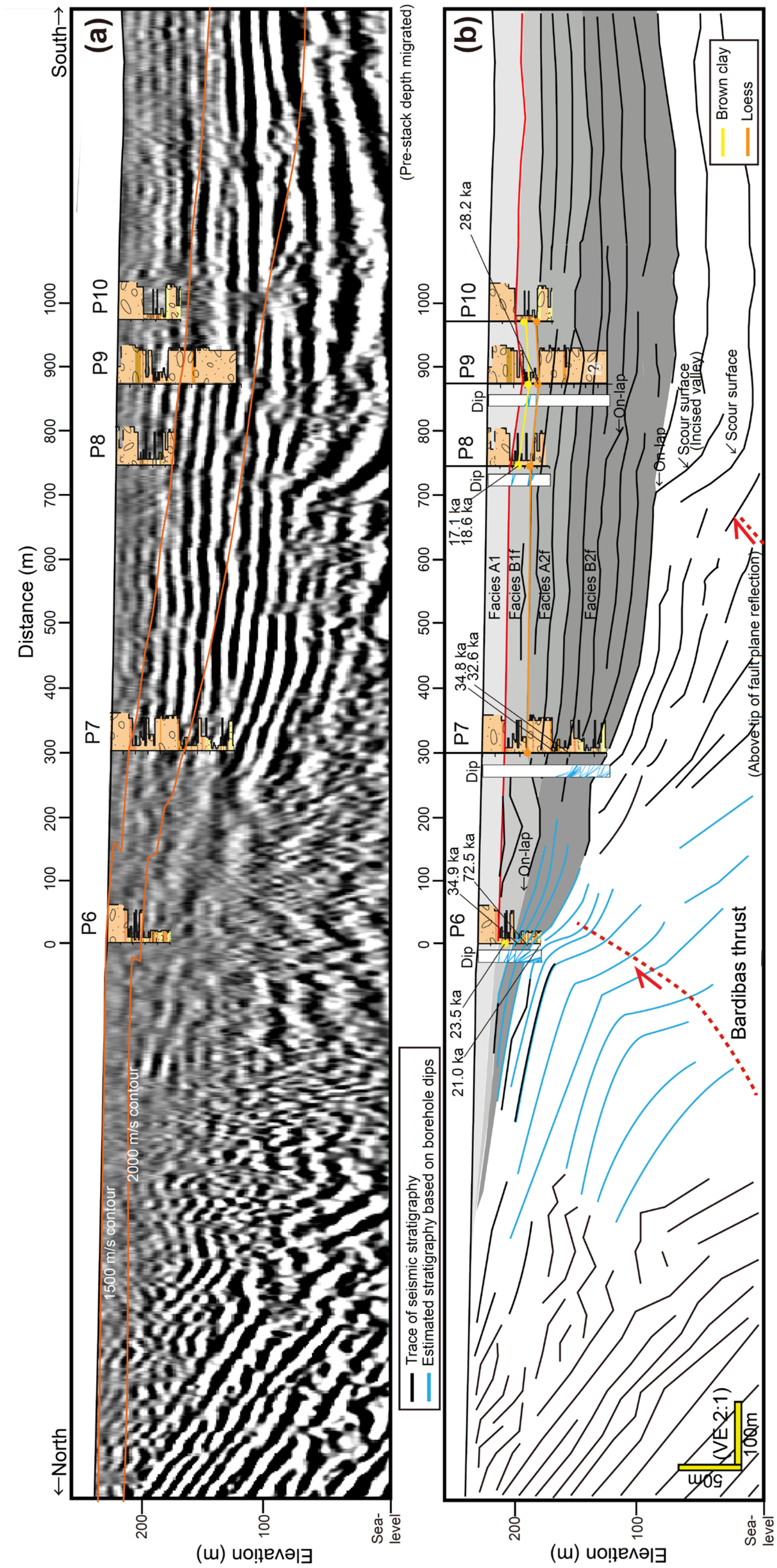

Figure 15. Ratu river cross-section. (a) Graphic sedimentary core logs of Sites P6–P10 placed on seismic reflection profile of Almeida et al. (2018). Northward increase

in dip in deeper sediments represents the effect of fault-propagation folding near the tip of the Bardibas thrust. Growth strata are observed in the footwall (south side). Vertical exaggeration=2:1. Near the base of the fold axis beneath Sites P6 and P7, seismic section shows poor imaging. (b) Interpretation of (a) with colored Facies A and B. Red line marks the base of top gravels (Facies A1) at ~15–28 mbs. Measured dip angles from the cores are shown in blue bars, vertically exaggerated (2:1). Marker beds of brown clay (yellow dots and lines) and loess (orange dots) are traced and their ages are shown next to graphic log (also see Table 1). Fluvial on-lap of sediments onto tilted strata is inferred. Red dashed lines represent the two fault splays of the Bardibas thrust from Almeida et al. (2018). The tip of the southern splay is inferred based on fault plane reflections beneath the growth strata, and the position of the northern splay is inferred based on fault-propagation folding.

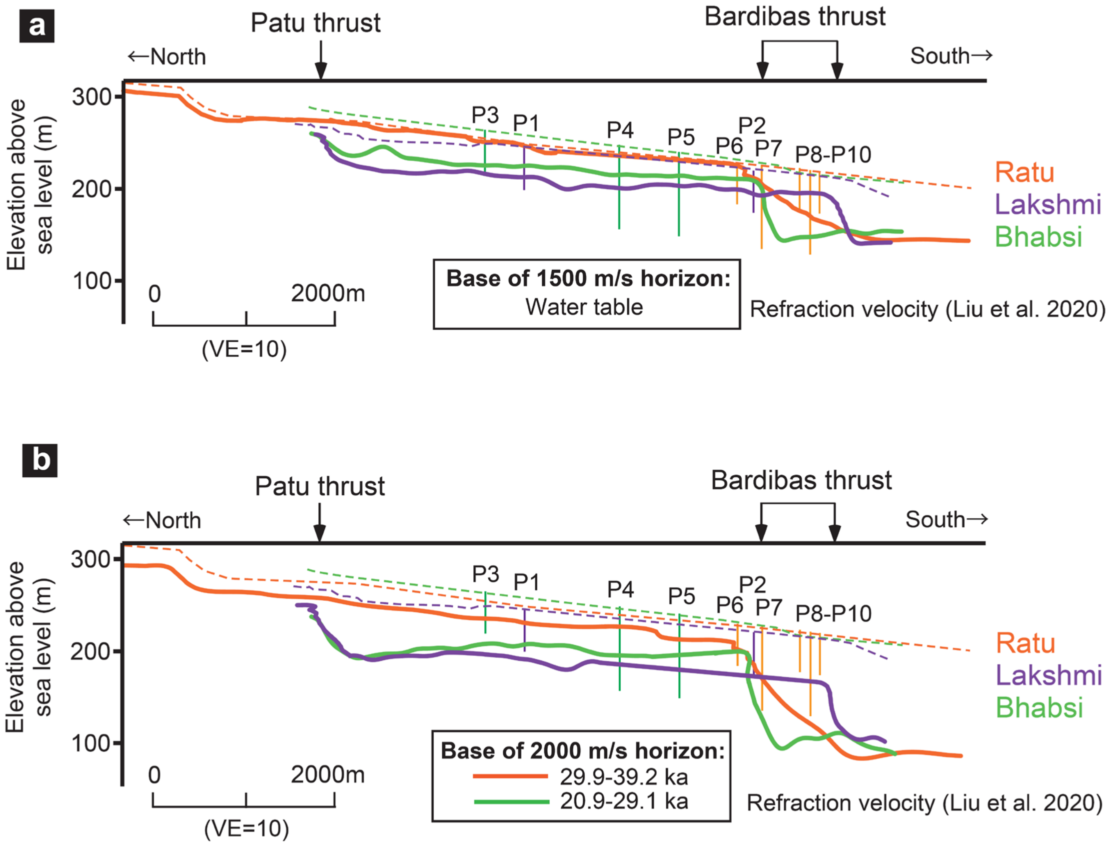

Figure 16. Boreholes placed onto refraction velocity models and the estimation of the timing of uplift. (a) Boreholes and sediment ages from this study placed on the refraction velocity model by Liu et al. (2020). Vertical exaggeration=10:1. 1500 m/s contour traced along the Ratu, Bhabsi and Ratu river profiles, interpreted to represent the water table. (b) 2000 m/s contour, proposed by Liu et al. (2020) to represent the top of the bedrock (Siwalik Group). In this study, the 2000 m/s horizon is found to be consistently above this contact, suggesting that the Siwalik Group strata have faster seismic velocities.

5.1.1. Temporary lacustrine depocenter formed due to uplift of the hanging wall anticline

Along the Lakshmi river, Site P1 is located near the crest of the hanging wall anticline of the Bardibas thrust, above the gently north-dipping back-limb, whereas Site P2 is located to the south, above a secondary tip-line anticline (Figs. 2c, 13). Since we do not have sediment ages from Site P1, and the seismic reflection imaging does not exhibit clear and continuous reflectors in this shallow section (Fig. 13a), we cannot define the timing of the facies transitions at Site P1. Because of this, we cannot exclude the possibility that Site P1 may have penetrated the bedrock Upper Siwalik Group (Fig. 13b).

At Site P2, beneath the recent ~10–20 m of coarse gravels (Facies A1), we identified a >25-m-thick section of lacustrine facies sediments (Facies C), which was not evident at Site P1 (Figs. 4, 13). We interpret that a depocenter formed between the broad anticlinal uplift to the north and the narrower uplift zone related to the fault tip to the south, that would have impounded the river, creating a small depocenter in the small syncline between these two anticlines (Fig. 13b).

The rate of deposition of the lacustrine sediments (Facies C) may represent the minimum rate of uplift of the secondary anticline in order to maintain a lacustrine depositional environment (e.g., Collignon et al., 2016). Samples from this section (Site

P2, Facies C) date from around 24.5 ± 0.3 to 43.1 ± 3.2 ka; however, it is not possible to confidently infer how long the depocenter was active due to the large scatter in the data (Fig. 12a). In addition, there may be a non-depositional time gap between the top of Facies C and the base of Facies A1. We therefore are unable to use this section to infer tectonic deformation rates.

Analogous modern depocenters have been identified elsewhere in the vicinity of the MFT, produced by local tectonic uplift. Dasgupta et al. (2013) reported the distribution of elongated lakes and marshes (long axis: ~0.5–1 km) with clay deposits (~1–2 m thick) at the base of north-facing scarps in the Bhutan Himalaya. These lakes are inferred to have resulted from damming of south-flowing rivers during uplift of the hanging wall of the local strands of the MFT there (Dasgupta et al., 2013). Larger paleo-lakes (~5 km in diameter) are also documented in the Lesser Himalaya in Kumaun near thrust faults, with sediments composed largely of carbonaceous mud (>5–10 m thick) deposited around 21–36 ka (Kotlia et al., 2000, 2008, 2010). These paleo-lakes are inferred to have formed behind thrust faults (Kotlia et al., 2000, 2008, 2010). Our study is the first documentation of such a paleo-lake formed by the MFT in the frontal piedmont in Nepal.

The paleo-lake sediments documented in this study were later capped by coarser fluvial inputs/gravels (Facies A1) during the late Pleistocene to Holocene (Site P2, Figs. 4, 13). This change may have resulted from a reduction in the rate of tectonic uplift, the breaching of the anticline by the Lakshmi river, or from a climate event that modified the fluvial sediment supply and/or discharge. Similarly, a number of paleo-lakes in the Kumaun Himalaya are also documented to have been filled with coarse fluvial deposits at around the same time (Kotlia et al., 2000, 2010), suggesting that this lake filling may have been the result of a regional climatic shift. The transition to coarse fluvial deposition across the late Pleistocene–Holocene is discussed in more detail in Section 5.2.

5.1.2. Tilted stratigraphy and uplift inferred from marker beds and ages above the hanging wall anticline

Along the Bhabsi river, Site P3 is located near the crest of the hanging wall anticline of the Bardibas thrust, whereas Sites P4 and P5 are located on the forelimb, more than 1 km south of the crest (Fig. 14). The coarse gravels of Facies A1 that compose the top unit in these cores thicken downstream, from 27 to 42 m and then 68 m. Based on the distance between the sites, and the changes in sediment thickness and channel slope, the base of Facies A1 dips ~1.2° between Sites P3 and P4, and ~2.8° between Sites P4 and P5, steeper than the current channel slope of ~0.7° (Fig. 14b). Below this unit (Facies

B1h), brown clay (at 28 mbs at Site P3 and 50 mbs at Site P4) and gleyed clay (at 39–40 mbs at Site P3, 80–85 mbs at Site P4, and 86–90 mbs at Site P5) can be traced as marker beds (Section 4.2; Fig. 14b). Between Sites P3 and P4 the apparent dip of the brown clay bed between boreholes is ~1.5°, and the dip of the gleyed clay bed ranges 2.1–2.3°. Between Sites P4 and P5, the gleyed clay bed dip ranges from 0.8° to 1.5° (Fig. 14b). Compared to the stratigraphic dip constrained by the marker beds, the orientations of laminas and silt beds measured directly from recovered cores (2–65°) show some much steeper values, which we attribute to local depositional and/or post-depositional processes such as cross-bedding and soft sediment deformation, or deviation of the well bore from vertical (Fig. 14b).

The tilting of the strata inferred from the boreholes along the Bhabsi river is likely caused by a combination of changes in river slope through time due to changes in sediment supply and/or river discharge (e.g., Finnegan et al., 2007), and folding of the hanging wall anticline of the Bardibas thrust, with associated southward tilt of the forelimb, similar to the shape of the underlying fold. In the current study, we cannot quantify the effect of varying sediment supply or river discharge on channel slope, however the difference in dip between the mapped dip of the marker beds and the current river slope may be a maximum estimate for tectonic tilting. We note that between Sites

P4 and P5, the dip of the gleyed clay beds in Facies B1h (0.8–1.5°) is less than that at the base of Facies A1 (~2.8°) above, although the clay beds of Facies B1h are older and should have incurred more tectonic deformation. This suggests that sediment supply and river discharge have a strong influence on the sediment thickness of Facies A1, obscuring the effect of tectonic deformation (folding) by the thrust. This also suggests that the base of Facies A1 may be erosive, and could have removed the underlying sediments (such as the brown clay downstream of Site P4).

Here, we use the age and tilting of the base of the brown clay (24.1±3.2 ka) and gleyed clay (30.9±2.3 ka) (Section 4.2) marker beds to estimate the shortening rate using an area-of-uplift calculation (e.g. Lavé & Avouac, 2000; Almeida et al., 2018; Fig. 17). We first estimate the area of uplift for each of the two marker beds, by tracing the tilted stratigraphy of the base of the brown clay and the gleyed clay in the seismic section, and inferring their original (undeformed) tilt of the sediments based on the modern channel slope (Fig. 17b).

Since we did not observe brown clay at Site P5, we interpret that this marker bed terminates between Sites P4 and P5, and/or was eroded at the base of Facies A1 (Fig. 17b). Here, we estimate the extension of the brown clay south of Site P4, by extending the stratigraphy between Sites P3 and P4 on a straight line (Fig. 17a,b). The section south of

Site P5 and north of Site P3 are also poorly imaged by the seismic data, and we cannot directly observe the area of uplift between Site P5 and the fault tip, and the area of uplift at the backlimb north of Site P3 (Fig. 17a,b). Here, we assume that the fold is symmetric, and estimate the uplift at these locations by extending the stratigraphy of the marker beds south of Site P5 to the fault tip and north of Site P3, and inferring the intersection with the original (undeformed) tilt of the sediments based on the modern channel slope (Fig. 17a,b). Our ranges of shortening allow for qualitative uncertainties in the location of the axial surface defining the northern edge of the backlimb, which is poorly imaged by the seismic data and not penetrated by boreholes (Fig. 17ab).

We use a depth to detachment from the undeformed horizon of ~1.9–2.1 km, defined by Almeida et al. (2018) from the Ratu profile, considering possible errors associated with the location of the axial surface (horizontal shift by ±100 m) and fault dip shifts by ±5° (Almeida et al., 2018; Fig. 3a). Since the hanging wall is buried by thicker sediments beneath the Bhabsi river than at Ratu river (Figs. 14, 15), it is possible that the axial surface beneath Bhabsi is located further away from the fault tip than at Ratu, making the detachment deeper than ~2 km. However, since we cannot clearly constrain the axial surface from the Bhabsi profile due to the scatter in seismic signals (Fig. 17), we prefer to use the depth to detachment (1.9–2.1 km) that is better constrained in the

Ratu section (Fig. 3a). We then assume conservation of mass; i.e., that the area displaced along the detachment equals the area of uplift (Fig. 17c). By dividing the area of uplift by the depth to detachment, we obtain shortening of 275±14 and 313±16 m in 24.1±3.2 (brown clay) and 30.9±2.3 ka (gleyed clay), respectively.

We plot the shortening vs. time to calculate an average shortening rate, assuming that the rate was constant over time (Fig. 18a). From this analysis, the shortening rate of the Bardibas thrust ranges from 11.4±2.4 m/ka (mm/a), inclusive of the full error ranges. The linear regression taking into account uncertainties of both ages and shortening (York et al., 2004) yields a shortening rate of 10.5±1.8 m/ka (mm/a) (Figure 18a; best-fit line). The shortening rate may have changed over time, but we do not have sufficient date points to address this. We also note that a deeper detachment depth will produce smaller shortening rates; e.g. if we use 3 km as detachment depth, we estimate a shortening rate of 7.5±1.3 m/ka.

Near or below the base of Sites P4 and P5 (deeper than ~100 mbs), seismic imaging reveals that the Siwalik bedrock dips ~14°, significantly steeper than the overlying sediments, below an angular unconformity (Almeida et al., 2018; Fig. 14). Creating this angular unconformity requires at least two phases: first, uplift and erosion (here, associated with tectonic folding), followed by a period during which the deposition rate exceeded the uplift rate. The sediments at 49 mbs at Site P3 are dated to 59.1±4.6 ka, which is the oldest obtained age in the drilled sections of the hanging wall. The overall thickness of the stratigraphy at Site P3 is thinner compared to Sites P4 and P5, likely due to the faster uplift near the crest of the anticline (Fig. 14, Table 2). Given that the underlying Siwalik Group sediments are much older (Miocene–Pliocene), we infer that the P3 borehole did not penetrate the Siwalik Group bedrock (Figs. 6, 14; Table 2).

The geometry of the upper 100 m of strata is not well-imaged in the seismic section (Fig. 14). The refraction velocity model by Liu et al. (2020) provides some additional detail in this shallow section (Figs. 3b, 16). Liu et al. (2020) highlight a transition at 1500 m/s, which they associate with the water table; this horizon lies somewhere in Facies B1h in the hanging wall units but does not show the southward deepening that we observe at Sites P3–P5, suggesting it may indeed reflect water rather than stratigraphy (Figs. 3b, 16). Liu et al. (2020) interpret the boundary between Siwalik Group and young sediments to be at 2000 m/s; with this interpretation, our boreholes P4 and P5 would penetrate the Siwalik Group (Figs. 3b, 16), which is inconsistent with the deepest dates from P4 (Fig. 6). The fine-grained Facies B1h sediments may have lower porosities and higher seismic velocities than the typical coarser young sediments (Facies A1), resulting in the miss-association of these sediments with the lithified, higher velocity

885 Siwalik Group sediments.

886

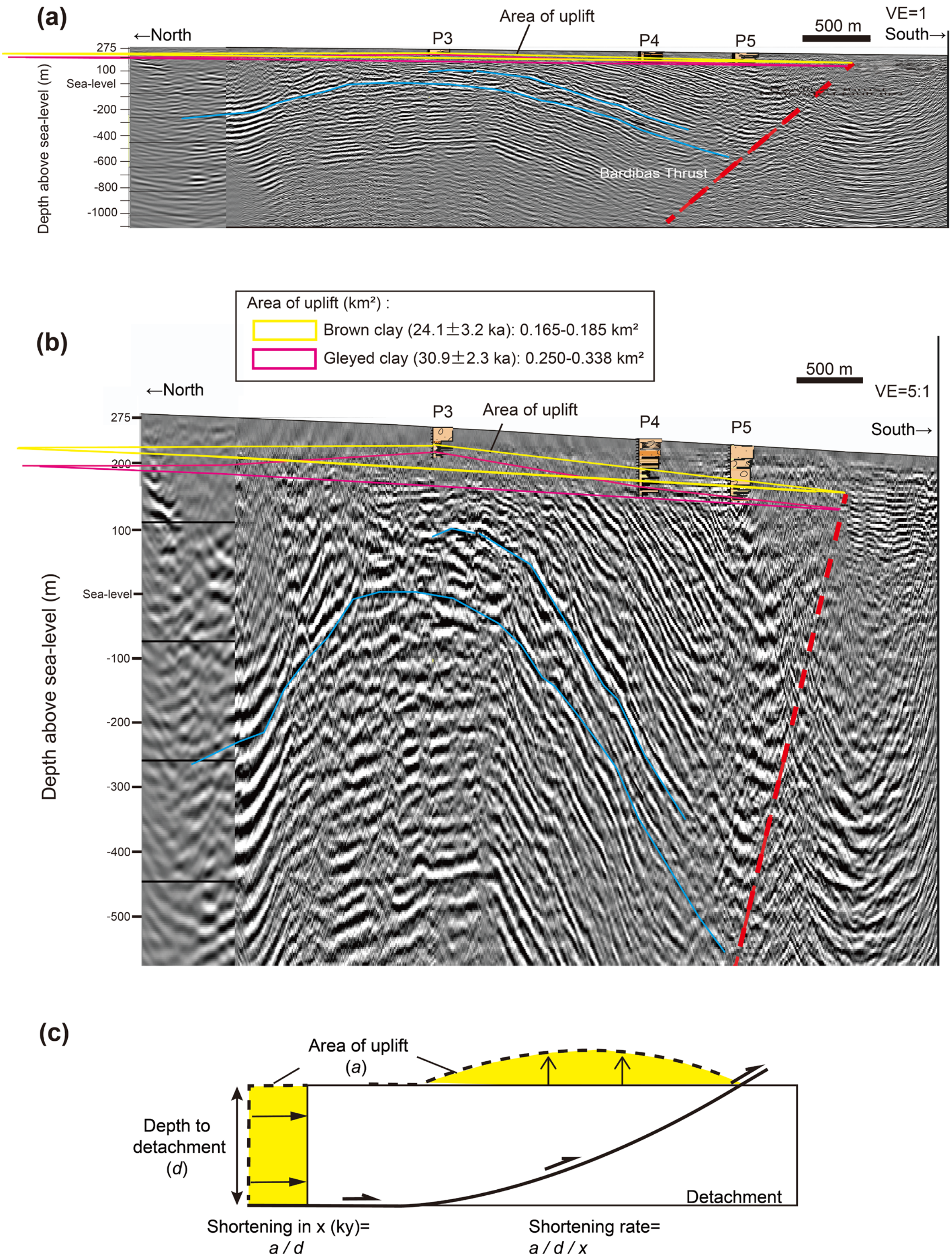

Figure 17. Shortening rate estimated from area-of-uplift calculation at the Bhabsi river. (a) Sites P3–P5 placed on seismic reflection profile of Almeida et al. (2018). No vertical exaggeration. Red dashed line represents the Bardibas thrust. Blue lines are representative trace of folded reflections at greater depth for reference. (b) Close-up of the entire lateral length of (a). Vertical exaggeration=5:1. Areas of uplift are obtained by tracing the base of the brown clay key marker bed (yellow) and the gleyed clay key marker bed (pink), assuming that the fold is symmetric, and by inferring that their depositional dip was equal to the modern channel slope. (c) Schematic cartoon showing the approach used to obtain shortening in this study, assuming that the area displaced along the detachment equals the area of uplift (colored yellow).

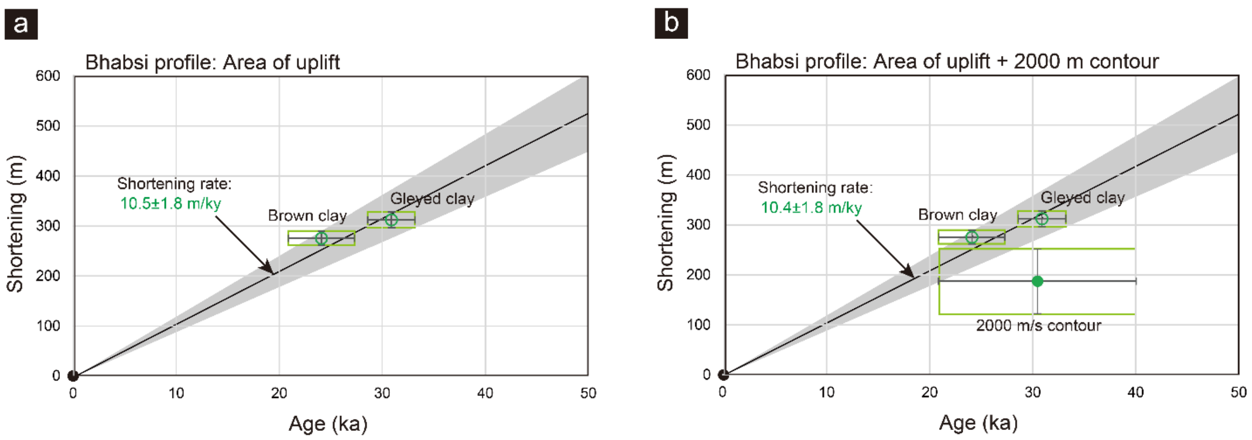

Figure 18. Shortening rate estimation for the Bhabsi river section. Black dot shows

0 ka (zero shortening). Box shows error range. The slope of the best-fit linear regression line indicates the shortening rate incorporating both uncertainties of shortening and age (York et al., 2004). Error is 2σ. Gray shaded areas are 95% confidence intervals. (a) Shortening estimated from area-of-uplift calculation based on stratigraphy of key bed markers (base of brown clay and gleyed clay) along the Bhabsi river profile (Fig. 17), plotted with sediment age. (b) Shortening combining data from uplift of marker beds and 2000 m/s contours (Fig. 19).

5.1.3. High-angle beds and deformation bands related to shallow deformation at the fault tip

Sites P6–P10 are located near the fault tip of the Bardibas thrust, south of the forelimb of the hanging wall anticline (Figs. 3c, 15). Here, there are two splays of the Bardibas thrust. The tip of the southern splay is inferred to be at ~300 mbs based on fault plane reflections beneath the growth strata, and the position of the northern splay is inferred based on fault-propagation folding (Almeida et al., 2018; Fig. 15). The high-angle beds observed in the cores at Sites P6 (~30–85° below 30 mbs) and P7 (~15°–45° below 55 mbs) are likely the result of fault-propagation folding up dip of the northern splay (Fig. 15). The seismic imaging cannot recover these high dips due to scattering of the signal; Site P6 therefore lies in a zone of no imaging that continues ~300 m to the south (Fig. 15). Based on the observations of bed dip from P6, we suggest that the abrupt transition from imaging to noise reflects a fold axis.

Packages of sediments defined as Facies A1, B1f, A2f, and B2f can be traced across Sites P6–P10 (Fig. 8); these sediments form the growth strata identified in seismic reflection profiles (Almeida et al., 2018) and illustrate the gradual southward decrease in stratigraphic dip (Fig. 15b). Traceable marker beds include the brown clay/silt and the loess, as described in Section 4.2 (Figs. 8, 15b). Measured dips from the cores are generally consistent with the dips of the seismic stratigraphy (Fig. 15b). The slight tilting of beds (by ~4°), which we observe around Sites P8 and P9 at ~15–40 mbs in both the cores and seismic stratigraphy, likely reflects kink band deformation above the fault tip documented by Almeida et al. (2018).

The tilted strata of Facies B2f observed at Sites P6 (> 31 mbs, Fig. 8a) and P7 (> 55 mbs, Fig. 8b) thicken downstream, from ~30 m thick below Site P6 to ~100 m thick below Site P10, as inferred from seismic data (Fig. 15b). This observation is consistent with uplift above the fault tip reducing the accommodation space. To the south, below Site P8, a scour surface is present at ~130 mbs, interpreted as an incised valley associated with episodes of incision and deposition (Almeida et al., 2018; Fig. 15b).

The near-vertical dip observed at Site P6 is consistent with surface outcrop measurements of bedding dips below river terraces that are vertical and even locally overturned in the southernmost part of the anticline forelimb (Almeida et al., 2018; Fig. 3a). These terraces are distributed above the current footwall growth strata, and the exposed tilted beds are documented as Siwalik bedrock (Fig. 3a). Beneath the current river, the bedrock is covered by growth strata. These growth strata exhibit sub-horizontal dips at shallow depths, and become steep below ~30–55 mbs at Sites P6 and P7 (Fig. 11). The near-vertical beds below ~30 mbs at Site P6 are dated to 21.0–72.5 ka (Fig. 8), indicating that they are not bedrock Upper Siwalik Group, despite their intense deformation. The significant amount of deformation of these young sediments and the terraces at the surface is likely due to localized deformation at the fault tip (Fig. 15).

Shallow deformation is also evident in the form of deformation bands, found in medium-coarse sand at Site P7 at 66 mbs (Section 4.1.3.2) (Figs. 10h–m). Here, we note deformation bands ~230 m above the fault tip of the Bardibas thrust; these are likely associated with related folding and strain. Deformation bands are a suite of narrow (generally mm- to cm-thick), low-displacement, tabular deformational features found both in poorly lithified porous sediments (Cashman et al., 2007), and lithified sediments with porosity >15%, such as sandstones, carbonates, tuffs, and chalks (Aydin, 1978;

Wilson et al., 2003; Fossen et al., 2007; Cilona et al., 2012; Wennberg et al., 2013; Pizzati et al., 2020). The deformation bands observed in this study indicate significant grain size reduction and porosity loss by cataclasis (Fig. 10h–m), and are classified as 'shear bands' or 'cataclastic shear bands' on the basis of their morphology (Fossen et al., 2007).

Cataclastic shear bands are generally known to form where higher confining and shear stresses in an initially high-porosity material are sufficient for grain breakage to occur (Fossen et al., 2007). In porous lithified rock, shear band formation is thought to occur at 1.5–3.0 km depth and effective stresses of 20–40 MPa, based on numerous field studies in predominantly quartz-rich aeolian sandstones (Fossen et al., 2007 and references therein), with the onset of cataclasis at burial depths of 0.9–1.2 km in quartz-rich sands, while in more arkosic sands, the onset of cataclasis in shear bands can occur at burial depths of 0.4–0.5 km (Beke et al., 2019; Pizzati et al., 2020). In contrast, the position of Site P7 in the hanging wall block of the active Bardibas thrust precludes significant burial beyond present-day depth, and the maximum overburden stress at ~66 m depth is ~1.3 MPa, assuming an average 15% overburden porosity. The confining stresses are thus too low to explain the significant cataclasis that is observed in the core (Figure 10h–m). The formation of deformation bands and observed cataclasis may thus likely instead records slip at seismic velocities reaching the surface in the process zone at the tip of the Bardibas thrust at some point post-deposition.

Cataclastic shear bands, with both porosity loss and visible cataclasis are also documented from unlithified sands in the immediate vicinity of active faults such as the San Andreas and McKinnleyville faults in California, USA (Cashman & Cashman, 2000; Cashman et al. 2007, Kaproth et al., 2010). These cataclastic bands in sands with maximum burial <200 m have been posited to be indications of slip at seismic velocities owing to the very low (<4.5 MPa) possible maximum overburden stresses at such depths being insufficient on their own to induce the observed cataclasis (Cashman et al., 2007). We suggest that the deformation band at Site P7 at ~66 m burial depth may similarly record brittle localized slip suggestive of rapid failure.

5.1.4. Slip rate estimation based on age and vertical uplift inferred from seismic refraction velocities

Figure 16 shows the depths of interpreted horizons based on seismic refraction velocities along the Lakshmi, Bhabsi, and Ratu river profiles (Liu et al., 2020). By placing our boreholes on the refraction velocity models and integrating our new dates with previously inferred fault throw, we can infer the rate of uplift on the Bardibas thrust (Figs. 3b, 16). Here, we evaluate the 1500 and 2000 m/s contours identified by Liu et al. (2020)

and establish the age of sediments for these horizons.

We first evaluate the 1500 m/s contour, interpreted by Liu et al. (2020) to represent the water table. Along the Lakshmi, Bhabsi, and Ratu rivers, this contour exhibits a vertical offset of ~17–32, ~12–51, ~57–66 m between the hanging wall and footwall of the Bardibas thrust, respectively (Liu et al., 2020) (Figs. 3b, 16a). In our boreholes, this 1500 m/s contour exists at ~40 mbs (Facies B) at Site P1 and ~27 mbs (Facies C) at Site P2 along the Lakshmi river (Figs. 3b, 16a). At the Bhabsi river, the 1500 m/s horizon exists at ~40 mbs (Facies B1h), ~35 mbs (Facies A1), and ~30 mbs (Facies A1) at Sites P3, P4, and P5, respectively (Figs. 3b, 16a). At the Ratu river, the 1500 m/s horizon is inferred at the subsurface at Site P6, ~15 mbs (Facies B1f) at Site P7, and at ~50 mbs (Facies A2f) at Site P9 (Figs. 15, 16ab). Given that we observe different lithologies at these depths, we agree that the 1500 m/s contour likely represents a non-stratigraphic feature like the water table, and therefore we are unable to assign an age for this horizon.

The 2000 m/s contour is inferred to represent a regional lithological boundary, common in all the three rivers, likely at the base of or within relatively young sediments (Liu et al., 2020) (Fig. 3b). At the Lakshmi river, this contour lies approximately at the base of our borehole at Site P2, and therefore the dates from the borehole would correspond to the sediments overlying it (Figs 3b, 16b). The dates in Facies C are mixed, ranging from 24.5±0.3 ka at 30.2 mbs to 43.1±3.2 ka at 26.8 mbs (Fig. 12a). Three well-constrained dates at 37.4–40.4 mbs near the base of the borehole all date between 35.2–40 ka (Fig. 12a), so we here use 40 ka to represent the youngest possible age of the contact at the Lakshmi river.

At the Bhabsi river, the 2000 m/s contour is at ~55 mbs (Facies B1h) at Site P4 and ~40–45 mbs (Facies A1/Facies B1h) at Site P5 (Fig. 3b, 16b); we estimate the timing of this horizon to be ~20.9–29.1 ka, based on the sediment age from Site P4 (24.1±3.2 ka at 50.8 mbs and 26.9±2.2 ka at 69.8 mbs) (Fig. 6). At the Ratu river, the 2000 m/s horizon is inferred at ~30 mbs (Facies B1f) at Site P6 and ~60 mbs (Facies B2f) at Site P7 (Figs. 3b, 16b); we infer the timing of this horizon to range ~29.9–39.2 ka, based on sediment age of 34.8±3.1 and 32.6±2.7 ka at 56.8 mbs and 70.8 mbs at Site P7, respectively, and 34.9±4.3 ka at 33.8 mbs at Site P6 (Fig. 8).

Here, we treat the sediment age of the 2000 m/s contour beneath the three rivers to be the same, and use the overall age range of ~20.9–40 ka to characterize this horizon for all the rivers, and fully incorporate the uncertainties of age. At the Lakshmi river, a vertical offset of ~37–42 m of the 2000 m/s contour is evident (Liu et al., 2020) (Fig. 16b). When using the sediment age of 20.9–40 ka, this yields a tectonic throw rate of 0.9–2.0 m/ka (mm/a), corresponding to a shortening rate of 1.9–5.9 m/ka (mm/a) given a fault dip of 20°–30° (Fig. 19).

At the Bhabsi river, a vertical offset of ~61–86 m is inferred at the 2000 m/s contour (Liu et al., 2020; Figs. 3b, 16b,c). From the estimated vertical offset and assigned age (20.9–40 ka), we calculate an uplift rate of 1.5–4.1 m/ka (mm/a), translated to a shortening rate of 3.1–12 m/ka (mm/a), using a fault dip of 20–30° (Fig. 19). The slip rate is comparable with the average shortening rate of 9.7–12.1 m/ka (mm/a) estimated by area of uplift calculation at the Bhabsi river in Section 5.1.2 (Figs. 17, 18), although it is also wide enough to be consistent with area of uplift estimates based on deeper detachment depths as well. When combining the results from the area of uplift and 2000 m/s contour, the linear regression taking into account uncertainties on all errors (York et al., 2004) yields a shortening rate of 10.4 ± 1.8 m/ka (mm/a) (Fig. 18b).

At the Ratu river, a vertical fault offset of >~95–101 m is inferred at the 2000 m/s contour (Liu et al., 2020; Figs. 3b, 16). The offset is a minimum fault throw, as the hanging wall is not fully preserved due to substantial erosion along the Ratu section (Fig. 3b). From the estimated vertical displacement, assigned age (20.9–40 ka), and fault dip (20–30°), we calculate an uplift rate of >2.4–4.8 m/ka (mm/ya), corresponding to a shortening rate of >4.8–14.1 m/ka (mm/a; Fig.19).

Uplift along the Ratu river has also been estimated from river terraces (Bollinger et al., 2014). Bollinger et al. (2014) describe at least four river terrace levels in the hanging wall of the Bardibas thrust, which have heights of ~1–2, ~16, ~40–45, and ~70 m above the current riverbed. If we incorporate the height of the regionally highest river terrace level (~70 m) as the maximum additional uplift in our estimation of slip rate at the Ratu section, this yields a maximum uplift and shortening rate of ~8.2 m/ka (mm/a) and ~23.9 m/ka (mm/a), respectively, using a fault dip of 20–30° (Fig. 19).

Bollinger et al. (2014) estimate an uplift rate of ~10 mm/a by the Bardibas thrust on the basis of the 70 m high terrace, estimated to date to ~7 ka (Gaillard et al., 2011). Using a fault dip of 20–30°, this would reflect a slip rate of 20–29 m/ka, which exceeds the shortening rate across the Himalaya (e.g., Lindsey et al., 2018) and is therefore implausible. We note that the age of this terrace (~7 ka) is poorly constrained, which is derived from a single charcoal sample (Gaillard et al. 2011). Furthermore, fluctuations in past river base level could either add to or subtract from this value, and we are not able to constrain this as we do not have materials dated within the last 7 ka (Tables 1, 2). The height of river terrace levels may also be affected by incision caused by climate events; assumptions of steady-state (erosion balancing uplift) may not be appropriate as the regional climate events such as the Indian monsoonal variations are reported in millennial to centennial to decadal scales (e.g., Wang et al., 2001; Fleitmann et al., 2003; 2007), and are likely to have an impact on river base levels and sedimentary environment (e.g., Pratt et al., 2004; Sharma et al., 2004) (Section 5.2).

Overall, our results indicate that the Bardibas thrust has slipped at an average rate of 1.9–5.9 m/ka (mm/a) (uplift rate: 0.9–2.0 m/ky) beneath the Lakshmi river, 3.1–12.1 m/ka (mm/a) (uplift rate: 1.5–4.1 m/ka) beneath the Bhabsi river, and >4.8 m/ka (maximum 23.8 m/ka) (uplift rate: >2.4 m/ka; maximum uplift rate: 8.2 m/ka) beneath the Ratu river over the last ~50 ka (Figs. 18, 19). We calculate an increase in slip rate from west (Lakshmi) to east (Ratu), which is consistent with the fact that the overall slip on the Bardibas thrust decreases towards the west where the Bardibas thrust strand is dying out, and transferring slip onto the Patu fault strand to the north (Almeida et al., 2018; Liu et al., 2020) (Fig. 2c). Our results from the Bhabsi river are more accurate as they likely reflect the full tectonic offset (Figs. 18, 19). The eastward increase in fault slip is compatible with observed variations in sediment thickness among the three rivers; we measure thicker sediments in the hanging wall along the Bhabsi river than in the Ratu river. In addition, there are possible variations caused by local depositional conditions due to river size and/or proximity of the range front. For example, we measure a thicker section of Facies A1 (27–68 m thick) beneath the Bhabsi river in the hanging wall of the Bardibas thrust than beneath the Ratu river (15–28 m thick) in the footwall of the Bardibas thrust (Figs. 13–15), also indicated by the brown clay marker bed that underlies it (Section 4.2) (Figs. 14–15).

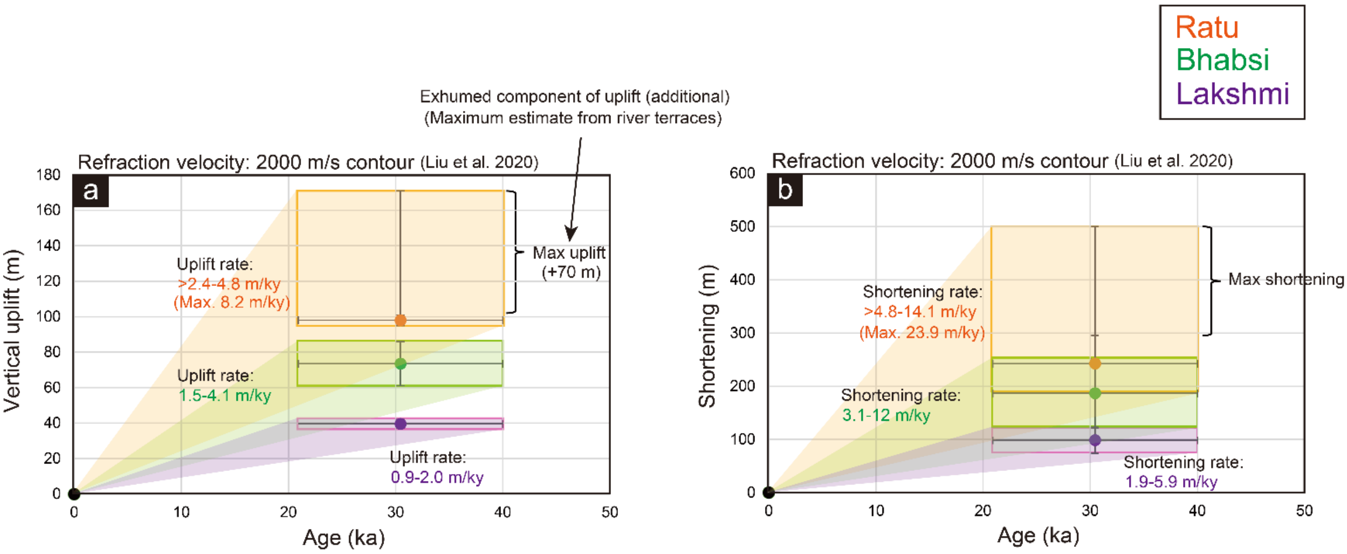

Figure 19. Uplift and shortening rate estimations using the 2000 m/s contour by Liu et al. (2020). Black dot shows 0 ka (zero shortening). Box shows error range. Colored areas show the range of uplift/shortening rate incorporating all errors. (a) Vertical offset at the base of 2000 m/s velocity contours along the Ratu, Bhabsi, and Lakshmi river profiles, plotted with sediment age. We incorporate additional uplift (~70 m; maximum value) above the riverbed from river terrace studies (Bollinger et al., 2014). (b) Shortening estimated from vertical fault offset at the base of 2000 m/s velocity contours (a), plotted with sediment age.

The Patu strand remains active at the longitude of the Ratu river, so we interpret that the slip here is being partitioned between the Bardibas and Patu thrusts (Fig. 2c). At the Ratu river, Almeida et al. (2018) calculated a total shortening of 1.81 km associated with the Patu thrust, and 1.67 km associated with the Bardibas thrust along their seismic lines. If the shortening rate is distributed along the same lines in the inferred ratio (1.81:1.67), this would imply that the Patu thrust is shortening at a rate of >5.2–15.3 m/ka (mm/a), and together the faults would be taking up >10–29.4 m/ka (mm/a). This assumption may be reasonable given that each fault is the frontal thrust of the range within a short distance (Fig. 2c), but is not founded in observation, and the uncertainties above do not reflect either the possibility that the ratio of active shortening differs from the total shortening, or uncertainties in the total shortening.

Bollinger et al. (2014) inferred that the river terrace abandonments in this region were locally consecutive to great earthquakes, and estimated the recurrence interval of past earthquakes and an average uplift rate of 8.5±1.5 mm/a (along the Sir river) and 10–12 mm/a (along the Ratu river) on the Patu and Bardibas thrusts, respectively, based on the elevations and dating of river terraces. Overall, their estimation is much larger than the uplift rate inferred in this study. This may be due to the maximum estimate of uplift from river terraces, which may also be affected by incision caused by climate events

(Section 5.2).

The geodetically constrained shortening rate across this section of the Himalaya is 15–16 m/ka (mm/a) (Lindsey et al., 2018); thus, the rate on this section of the Bardibas thrust inferred from this study from the Bhabsi river (3.1–12.1 m/ka; York regression: 10.4 ± 1.8 m/ka) (Fig. 18) represents 19–81% (York regression: 54–81%) of the total shortening across the range. Lavé and Avouac (2000) interpreted that nearly all of the interseismic shortening eventually manifests as slip on the frontal thrust systems in the region around the Bakeya and Bagmati Rivers, 40–60 km west of our field area. This would be consistent with our results, but our large uncertainties mean that we cannot exclude the possibility of significant shortening being accommodated on other structures within the range.

5.2. Implications for the depositional environment across monsoonal climate variations

5.2.1 Facies transitions in this study compared with paleoclimate records

We identify three depositional facies in the sediment cores recovered from the three rivers: coarse-grained braided channel (Facies A), fine-grained braided channel

(Facies B), and fluvio-lacustrine (Facies C); these are primarily marked by changes in p (grain diameter) size (Section 4.1; Figs. 4, 6, 8). The fact that we observe similar facies transitions in different rivers suggest that they represent a regional event. In general, changes in fluvial sediment grain size are thought to be associated with variations in river discharge, sediment supply, abrasion, and subsidence rate (e.g., Robinson & Slingerland, 1998; Dingle et al., 2017). The timescale of the sediment deposition in this study is tens of ka, and therefore tectonic subsidence/uplift (>hundreds of ka) and/or earthquake-triggered landsliding (<few hundred years) (e.g., Bollinger et al., 2014; Rizza et al., 2019) cannot be the cause for the observed variations in grain size, except for Facies C, which we observe only at Site P2 and interpret as related to localized uplift to the south (see Section 5.1.1). We can also eliminate variations in abrasion, as the sediments are quartz-dominant and the length of the catchment is only a few km. We therefore suggest that changes in river discharge and sediment supply are likely to be the primary processes recorded in these sedimentary facies. Higher river discharge is capable of transporting more and coarser sediments, and hence, the grain size of deposited sediments is expected to be larger (e.g., Parker, 1978). Empirical and physical studies have shown that an increase in river discharge tends to increase both sediment grain size and channel width (e.g., Parker, 1978; Bray, 1982; Hey and Thorne, 1986).

A major transition from fluvio-lacustrine facies (Facies B1h, B1f and C) to coarse braided channel facies (Facies A1) is observed at depths of ~15–68 mbs in all ten boreholes (Figs. 4, 6, 8). ^{14}C and OSL dating from Site P3 suggest that this transition, from finer sediments to coarser, is younger than ~13.5±0.1 ka, around the Pleistocene-Holocene transition (Fig. 12b). The timing of this facies transition coincides with a transition in regional climate observed in a number of climate proxies. Specifically, the Indian monsoon was generally weak in the late Pleistocene, and became much stronger during the Holocene, as determined from speleothems from the Bittoo cave in northwest India (Kathayat et al., 2016), the Timta cave in north-central India (Sinha et al., 2005), and the Mawmluh cave in northeast India (Dutt et al., 2015) (Fig. 20). Previous studies have linked monsoonal variability with Earth's orbital parameters, such as precessional cycles and variations in the Northern Hemisphere summer solar insolation (NHSI), punctuated by millennial-scale oscillations such as the Younger Dryas and Heinrich events (e.g., Cai et al., 2015; Kathayat et al., 2016). The period of strengthened monsoon around the Pleistocene/Holocene transition correlates with the peak of the NHSI and precession that occurred following the Bølling-Allerød interstadial and the last glacial to interglacial boundary (Berger and Lutre, 1991; Wolff et al. 2010) (Fig. 20).

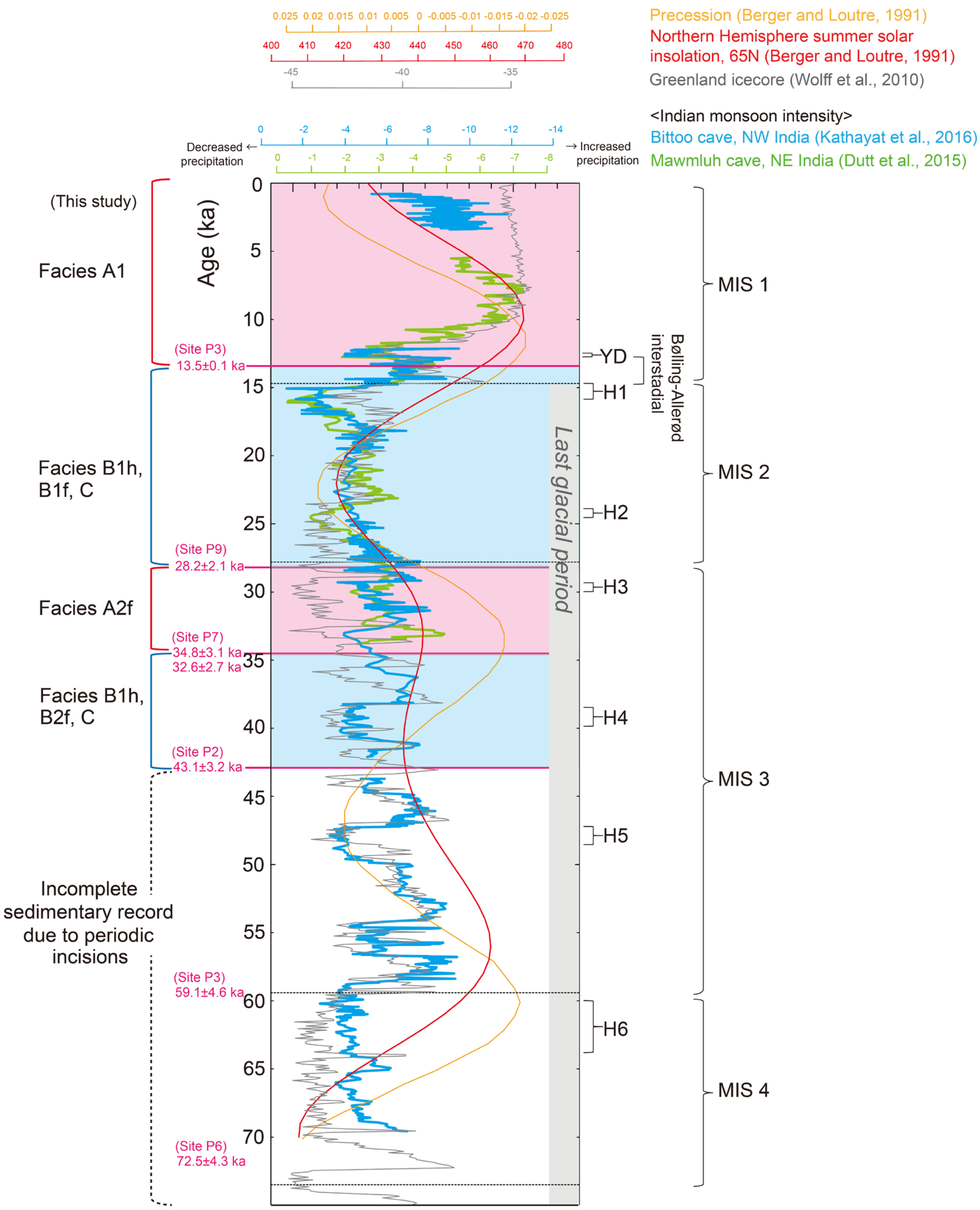

Figure 20. Comparison of our stratigraphic records to records related to the Indian summer monsoon. Plotted records include: compiled δ18O records of cave speleothems (blue and green) tracking Indian summer monsoon intensity, Northern

Hemisphere summer solar insolation (NHSI) (red), orbital precession cycle (orange), and Greenland ice core records (gray). Speleothem δ18O data indicate Indian summer monsoon intensity, where larger absolute values indicate increased precipitation. YD: Younger Dryas. H1–H6: Heinrich events. Gray vertical bar marks the duration of the last glacial period. MIS 1–4: Marine isotope stages, separated by horizontal dotted lines (black). Red shading: Facies A in this study. Blue shading: Facies B and C in this study. Red horizontal line marks the age of each facies transition based on sediment age from Sites P2 (43.1±3.2 ka), P3 (13.5±0.1 ka), P6 (72.5±4.3 ka), P7 (34.8±3.1 ka, 32.6±2.7 ka), and P9 (28.2±2.1 ka) in this study. Facies B and C roughly correlates with the minima of the precession and NHSI, when the monsoon was weaker. In contrast, Facies A roughly coincides with the precession and NHSI maxima, when the monsoon was stronger. Prior to ~43 ka, we are unable to correlate facies with climate events due to missing ages likely associated with incision.

Below this interval, the footwall strata exhibit packages of fine-grained Facies B1f dated to ~13.5–28.2 ka (Figs. 8, 15). These dates match to a period with low NHSI and low precession, when the monsoon was weak (Dutt et al., 2015; Kathayat et al., 2016)

(Fig. 20). This period also corresponds to marine isotope stage (MIS) 2, during the last glacial.

Below this section of Facies B1h and B1f, we have mixed records: at Sites P3 and P4 (hanging wall), we do not recognize another major facies transition, although ages in these cores reach as old as 59.1±4.6 ka (Fig. 6). In contrast, in the footwall cores (P7–P10), we identify a second package of coarse-grained Facies A2f dating to ~28.2–34.8 ka (Figs. 8, 15). This difference may relate to lower stratigraphic preservation over the hanging wall due to uplift, or may have been eroded due to base level fluctuations. We therefore consider that the footwall record is likely to be more representative. Notably, the ages for this coarser section coincide with a period when the NHSI and precession were elevated, and the beginning of MIS 3 (globally warm period) (Fig. 20). Climate proxies also show that the monsoon was stronger during this period, although not as strong as during the Holocene (Dutt et al., 2015; Kathayat et al., 2016; Fig. 20).

The borehole at Site P7 penetrates an additional section of fine-grained Facies B2f in its lowest section (Fig. 8). This period also correlates to the deposition of Facies C (lacustrine) sediments at Site P2 (Fig. 4). During or before this period, there was also events of incision, as inferred from fluvial onlap in seismic imaging (Fig. 15). Climate proxies from this time (prior to ~32.6–34.8 ka) show high-frequency variations without large magnitude of changes; while during this time, the NHSI started low and increased over time (Fig. 20). Given our limited records (likely incomplete due to periodic incision), together with the variability in other climate proxies, it is not possible to link the facies in this section to specific climatic conditions. The oldest sediments that we recovered in this study date to 59.1±4.6 ka at Site P3 in the hanging wall and 72.5±4.3 ka at Site P6 in the footwall; however, we did not recover sediments between 43.1–59.1 ka and 59.1–72.5 ka.

We suggest that the primary sedimentary facies transitions observed in this study are likely associated with changes in the Indian monsoonal climate, which is linked to Earth's precession (~23-ka-cycle; Fig. 20). Indian monsoon intensity is a primary control on river discharge and sediment supply in this region. While the latest transition in sedimentary facies appears to correlate with the last glacial maximum, the catchments of the rivers we are studying were never glaciated (e.g. Owen et al., 2002, 2005, 2009; Tsukamoto et al., 2002; Asahi, 2010), and thus the glaciers did not directly affect river discharge and sediment output in this region.

We interpret instead that the strengthened Indian monsoon through the late Pleistocene to the Holocene led to increased river discharge and the advance of coarse bedload-dominant braided channels in our study area (Figs. 21a, b). These channels were likely wider and less mobile, similar to modern channels (Section 2), due to the high stream power and transport capability (e.g., Wickert et al., 2013; Bufe et al., 2016; Fig. 21b). In contrast, weak monsoon periods should have decreased river discharge and formed a finer-grained channel environment (Fig. 21a, c). These rivers were likely narrower and had higher lateral mobility, forming distinct floodplains and occasional river bedload sediments, as inferred from Facies B (Fig. 21c).

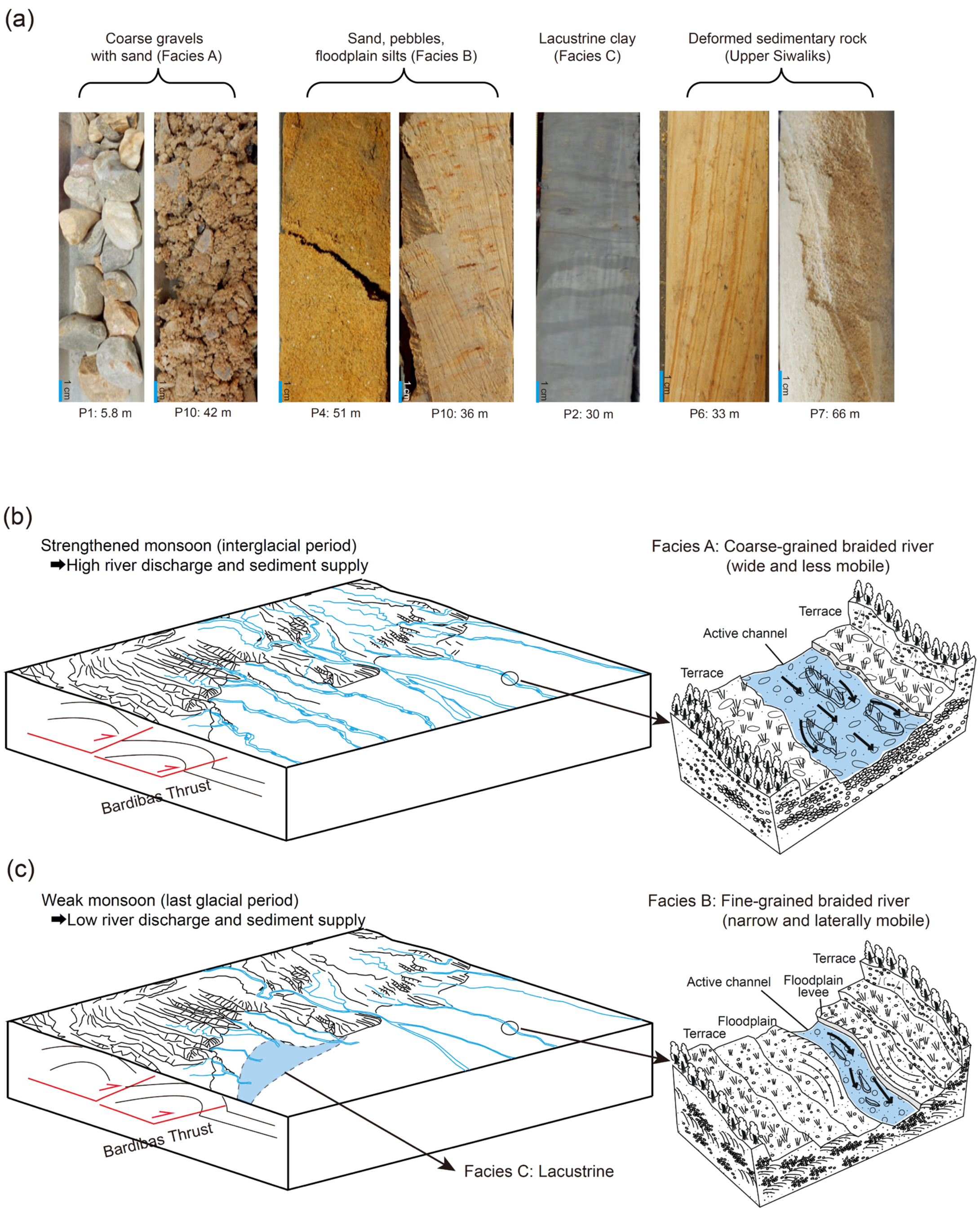

1229

1230 **Figure 21. Overview of observed facies and inferred evolution of depositional**
1231 **environment. (a) Summary of observed facies (see main text). (b) Left: Fluvial**
1232 **environment during strengthened monsoon characterized by wide braided rivers.**
1233 **Rivers are marked in blue. Right: Schematic image of coarse-grained braided**

channel facies (Facies A) during strengthened monsoon. These rivers are wide with less distinct floodplains (less laterally mobile). (c) Left: Fluvio-lacustrine environment during weak monsoon, characterized by narrower braided rivers. Right: Schematic image of fine-grained braided channel facies (Facies B) during weak monsoon. These rivers were laterally mobile, with adjacent floodplain levees.

Other regions around the Himalaya also exhibit a coarse alluvial/fluvial aggradation around the early Holocene (~12–6 ka). These results are inferred from fluvial terraces in several duns and valleys between the MFT and MBT, including the Subathu sub-basin (Kumar et al., 2007), Ganga valley (Sinha et al., 2010; Ray and Srivastava, 2010), Yamuna valley (Dutta et al., 2012), Kangra Dun (Dey et al., 2016) and Pinjaur Dun (Suresh et al., 2007), and in foreland alluvial fan systems south of the MFT, such as the Matiali inter-megafan (Kar et al., 2014) and the southern Ganga Plain (Sinha et al., 2007) (Supporting Information Fig. S8). These studies document a shift from a fine-grained environment such as interfluve floodplains, distal fans, paleosols, aeolian and lakes during the last glacial, to a coarser-grained environment in the early Holocene (e.g., Sinha et al., 2007; Kumar et al., 2007; Srivastava et al., 2009; Dutta et al., 2012). Loess deposition, as observed in Facies B in this study (Section 4), is reported in multiple regions in the Himalaya (e.g., Pant et al., 2005; Srivastava et al., 2003a, 2009), often tied to cold, dry and windier conditions when the monsoon was weaker (e.g., Harrison et al., 2001; Pourmand et al., 2004).

Although the primary shift from fine to coarser sediments is likely climatic in origin, the lacustrine Facies C in this study observed at Site P2 is not. We interpret that this section is the result of uplift around the frontal thrust temporarily defeating the river, resulting in a local depocenter and ponding (Section 5.1.1; Fig. 21c). However, the fact that this ponding no longer exists suggests that it may have been favoured by the weaker monsoon conditions that were active at the time: the reduced river discharge made its defeat by tectonic uplift more likely.

These lacustrine sediments may provide a record of climate-related hydrological changes. For example, the alternations from oxidized to gleyed clay observed at 29–34 mbs at Site P2 (Figs. 4b, 12a, Section 4.1.2) imply diagenetic changes from aerobic to anaerobic conditions, perhaps related to the stadial Heinrich 4–6 events (Fig. 20). The increase in $\delta^{13}C$ values (-13.6–11‰) in gleyed fine sediments at 33–41 mbs suggests decreased precipitation (Table 1). The gradual transition to oxidized sediments above 29 mbs (Fig. 4b) and the low $\delta^{13}C$ values (-17 to -14.4‰) between 28–30 mbs (Table 1, Section 4.1.2), may reflect a transition to a warmer climate towards the Holocene, as the paleo-lake was gradually filled by fluvial input. Based on our limited ages, we cannot confidently relate these variations to regional climate, but suggest that these sediments could provide a window into past climate in this region.

5.2.2. Implications for base level changes across monsoonal climate variation

In addition to stratigraphic changes, we also observe striking changes in relative base level, likely also tied to climatic variations. Sites P1–P5 are located in the hanging wall of the MFT, and therefore tectonic uplift should lower the relative river base level, decreasing the accommodation space for sediments. This is consistent with the angular unconformity imaged in the hanging wall of the Bardibas thrust beneath the Bhabsi River that indicates that the local base level was at least 100 m lower than the present river level when it formed, however after that anticline bevelling event, it has risen (Almeida et al., 2018) (Figs. 3d, 14). To explain this, we must conclude that monsoonal climate variations have affected river base levels in this region (Fig. 22). In the footwall, an incised valley observed in the Ratu River profile also suggests that relative base levels fluctuated in the past (Almeida et al., 2018) (Fig. 15). Based on sediment ages determined here, there has been significant net aggradation over the last few 10s of ka, but it is likely that the observed record is not continuous, preferentially preserving sediments deposited in the early parts of aggradation periods, as the upper sediments might have been later eroded as base level once again dropped (Fig. 22). This process was likely more intense in the hanging wall region (Sites P1–P5) than the footwall (Sites P7–P10), as the hanging wall has been subject to persistent tectonic uplift.

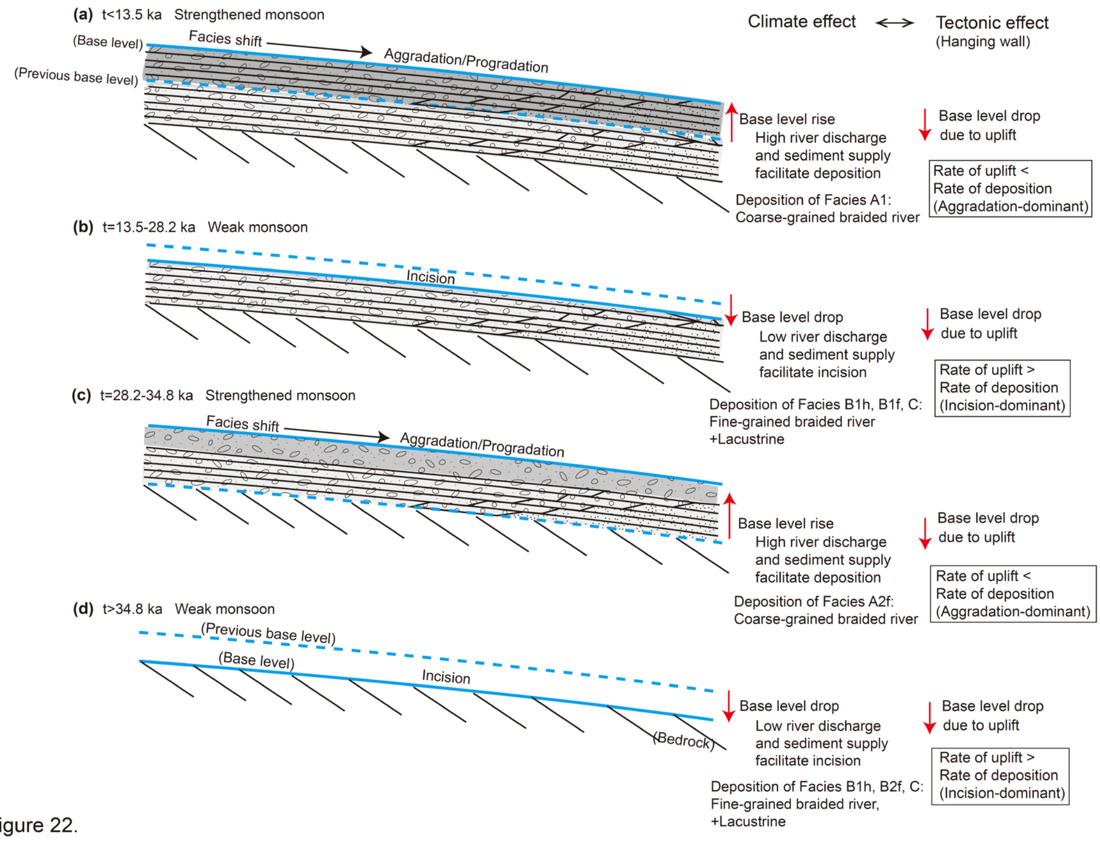

Figure 22.

Figure 22. Base level evolution inferred in this study during different time intervals. Solid blue line: location of base level at each time stage. Dashed blue line: location of previous base level. Tectonic uplift in the hanging wall lowers the relative base level. (a) t<13.5 ka: Sediment aggradation/progradation is facilitated by

strengthened monsoon that causes increase in river discharge and sediment supply, raising the base level. Facies A1 deposited during this period. (b) t=13.5–28.2 ka: During a weak monsoon period, a decrease in river discharge and sediment supply facilitated incision and base level fall, or slow base level rise. Incision and slow deposition occurred, and Facies B and C were deposited during this period. (c) t=28.2–34.8 ka: Dominant aggradation/progradation, rise of base level, and deposition of Facies A2 during strengthened monsoon (similar process as t<13.5 ka). (d) t>34.8 ka: Enhanced incision, base level fall and/or slow rise, and deposition of Facies B and C during weak monsoons (similar process as t=13.5–28.2 ka).

Regionally, the monsoon is known to have a substantial influence on base level (Figs. 1, Supporting Information Fig. S8). In Higher and Lesser Himalayan rivers, increased river discharge during strengthened monsoons is inferred to produce large sediment supply and immediate aggradation in the form of increased alluvium, fill-terrace deposits and landslides, raising river base levels (e.g., Pratt et al., 2002, 2004; Bookhagen et al., 2005, 2006) (Fig. 1). This upstream aggradation is associated with lower sediment supply downstream, as observed in the Ganga and Yamuna Rivers in the Ganga Plain, where high river discharge but low sediment supply during a strengthened monsoon favours incision, lowering the base level (e.g., Srivastava et al., 2003b; Gibling et al., 2005; Sinha et al., 2007) (Fig. 1). In our case, the sites we are studying are very close to the headwaters of the rivers, and our results more closely mirror the upstream results.

Other studies in the piedmont foreland, however, do not always report consistent results. Some report similar patterns: in the Kangra Dun valley (Thakur et al., 2014; Dey et al., 2016), Dehra Dun (Densmore et al., 2016), and Matiali inter-megafan (Kar et al., 2014), strengthened monsoons seem to be associated with high river discharge, high sediment supply and dominant fan/terrace aggradation (Fig. 1), with incision during weak monsoon conditions. However, other regions report different patterns: in the Subathu sub-basin (Kumar et al., 2007), Ganga valley (Sinha et al., 2009; Ray and Srivastava, 2010), Yamuna valley (Dutta et al., 2012), and Pinjaur Dun (Suresh et al., 2007), strengthened monsoons seem to be associated with high river discharge, low sediment supply and dominant incision in the form of terrace abandonment and base level drop (Fig. 1). These studies suggest that there is higher sediment supply during weak monsoon periods due to less vegetation cover and enhanced weathering.

All of these studies in the piedmont agree that a strengthened monsoon should increase river discharge, but suggest different patterns in sediment supply. We note that the regions where sediment supply seems to decrease are formed by large river systems (e.g. Ganga river), and are relatively downstream, compared to the smaller, foothill-fed river systems closer to the catchment like the ones in this study. Thus, these differences likely reflect very real differences in the erosion patterns and sediment transport of different scales of fluvial systems.

6. Conclusions

We drilled and cored to depths of 45–100 m at ten sites along three rivers crossing the southernmost blind fault strand of the MFT in central Nepal, locally named the Bardibas thrust. We characterize the sedimentary facies of the recovered cores, and obtain sediment ages using OSL and radiocarbon dating. By combining our observations with previously published seismic profiles, we study the subsurface structure and the slip rate of the Bardibas thrust, and infer the evolution of the depositional environment. Our main findings are:

1. Sediment cores reveal a lacustrine depocenter between the south-dipping limb of the hanging wall anticline and a north-dipping limb of a smaller tip-line fold, formed due to the uplift near the fault tip of the Bardibas thrust. Our study is the first to document a paleolake formed by the MFT in the Nepalese Himalayan piedmont.

2. Near the tip of the Bardibas thrust, high-angle bedding planes and deformation bands were observed in the sediment cores, ~250 m above the fault tip. These structures characterize the shallow deformation ahead of the propagating fault tip, demonstrating that deformation by the blind thrust reaches to shallow depths via local folding and small-scale faults.
3. We identify marker beds and correlate them between boreholes. By measuring their deformation and age, our results indicate that the Bardibas thrust has slipped at an average rate of 1.9–5.9 m/ka (uplift rate: 0.9–2.0 m/ka) beneath the Lakshmi river, 3.1–12.1 m/ka (uplift rate: 1.5–4.1 m/ka) beneath the Bhabsi river, and >4.8 m/ka (maximum 23.9 m/ka) (uplift rate: >2.4 m/ka; maximum uplift rate: 8.2 m/ka) beneath the Ratu river over the last ~50 ka. The rate on this section of the Bardibas thrust (3.1–12.1 m/ka; Bhabsi) represents 19–81% of the total shortening across the Himalaya at this longitude. The uplift rates estimated in this study are smaller than those reported from previous studies based on elevations of river terraces.
4. We recognize major transitions from finer-grained, fluvio-lacustrine facies to coarse-grained braided channel facies in all ten boreholes. The timing of the facies transitions correlates with reported Indian monsoonal intensity variations linked to northern hemisphere summer solar insolation and precession. We infer that strengthened

monsoon conditions led to increased river discharge and advance of coarse bedload-dominant braided channels, whereas weak monsoon periods formed a finer-grained fluvial channel environment.

5. Fluctuations of river base levels in the past are evident from the seismically imaged angular unconformity underlying the deposition of ~100 m of recent sediments in the hanging wall, and an incised valley in the footwall. Monsoonal climate variations have likely affected the river base levels in this region, causing a non-steady state among uplift, deposition, and incision.

Acknowledgments

This research was supported by the National Research Foundation Singapore (NRF) and the Singapore Ministry of Education under the Research Centres of Excellence initiative, the Earth Observatory of Singapore, and the NRF Fellowship scheme (award No. NRF-NRFF2013-06). This work comprises Earth Observatory of Singapore contribution no. 425. We express our gratitude to Ranjan Kumar Dahal, Manita Timilsina, Om Dhakal, Nitesh Shrestha, and staff members from Geotech Solutions International Pvt Ltd for the drilling operations and core management, and for providing laboratory space. We also thank Suman Pariyar for helping with onsite operations. We are grateful to the Department of Mines and Geology (National Seismological Center, Nepal) and their staff members for providing laboratory space and core storage space. We thank Zhi Long Goh, Jing Ci Neo, Miranda Ong, and Cheng Seah for their assistance in core description and log data analyses. We are thankful to Paul Tapponnier, Çağil Karakaş, and Edgardo Latrubesse for useful discussions. We are grateful to Paula Marques Figueiredo and Antonio Votor for preparing the sediments ready for OSL dating. The authors declare that they have no known financial conflicts of interests or personal relationships that could have appeared to influence the results of this paper.

Open Research

All data used in this study is attached in Supporting Information. The satellite image in Figure 2b uses a map from Google Earth imagery, Image Landsat/Copernicus.

References

Adamiec, G. & Aitken, M. (1998). Dose-rate conversion factors: update. *Ancient TL*, 16, 37–50.

Ader, T., Avouac, J., Liu-Zeng, J., Lyon-Caen, H., Bollinger, L., Galetzka, J., Genrich, J., Thomas, M., Chanard, K., Sapkota, S. N., Rajaure, S., Shrestha, P., Ding, L., &

Flouzat, M. (2012). Convergence rate across the Nepal Himalaya and interseismic coupling on the Main Himalayan Thrust: Implications for seismic hazard. *Journal of Geophysical Research: Solid Earth,* 117(B04403), doi:https://doi.org/10.1029/2011JB009071.

Almeida, R. V., Hubbard, J., Liberty, L., Foster, A., & Sapkota, S. N. (2018). Seismic imaging of the Main Frontal Thrust in Nepal reveals a shallow decollement and blind thrusting. *Earth and Planetary Science Letters,* 494, 216-225. https://doi.org/10.1016/j.epsl.2018.04.045

Asahi, K. (2010). Equilibrium-line altitudes of the present and Last Glacial Maximum in the eastern Nepal Himalayas and their implications for SW monsoon climate. *Quaternary International*, 212, 26-34. doi:10.1016/j.quaint.2008.08.004

Aydin, A. (1978). Small faults formed as deformation bands in sandstone. Pure and Applied Geophysics 116, pp. 913–930.

Beke, B., Fodor, L., Millar, L., Petrik, A., (2019). Deformation band formation as a function of progressive burial: Depth calibration and mechanism change in the Pannonian Basin (Hungary). *Marine and Petroleum Geology* 105, pp. 1 – 16.

Berger, A., & Loutre, M. F. (1991). Insolation values for the climate of the last 10 million years. *Quaternary Science Reviews*, 10, 297-317.

Blum, M. D, & Törnqvist, T. E. (2000). Fluvial responses to climate and sea-level change: a review and look forward. *Sedimentology*, 47 (s1), 2-48. https://doi.org/10.1046/j.1365-3091.2000.00008.x.

Bollinger, L., Sapkota, S. N., Tapponnier, P., Klinger, Y., Rizza, M., Van der Woerd, J., Tiwari, D. R., Pandey, R., Bitri, A., & Bes de Berc, S. (2014). Estimating the return times of great Himalayan earthquakes in eastern Nepal: Evidence from the Patu and Bardibas strands of the Main Frontal Thrust. *Journal of Geophysical Research: Solid Earth*, 119, 7123-7163. doi:10.1002/2014JB010970.

Bookhagen, B., Thiede, R. C., & Strecker, M. R. (2005). Late Quaternary intensified monsoon phases control landscape evolution in the northwest Himalaya. *Geology*, 33 (2), 149-152. doi: 10.1130/G20982.1

Bookhagen, B., Fleitmann, D., Nishizumi, K., Strecker, M. R., & Thiede, R. C. (2006). Holocene monsoonal dynamics and fluvial terrace formation in the northwest Himalaya India. *Geology*, 34 (7), 601-604. doi: 10.1130/G22698.1.

Bookhagen, B., & Burbank, D. W. (2010). Toward a complete Himalayan hydrological budget: Spatiotemporal distribution of snowmelt and rainfall and their impact on river discharge. *Journal of Geophysical Research*, 115, F03019. doi:10.1029/2009JF001426

Bray, D. I. (1982). Regime equations for gravel-bed rivers. *in* Hey, R.D., Bathhurst, J.C., and Thorne, C.R., eds., Gravel-Bed Rivers; Fluvial Processes, Engineering and Management: Chichester, U.K., Wiley, p. 517–542.

Cai, Y., Fung, I. Y., Edwards, R. L., An, Z., Cheng, H., Lee, J-E., Tan, L., Shen, C-C., Wang, X., Day, J. A., Zhou, W., Kelly, M. J., & Chiang, J. C. H. (2015). Variability of stalagmite-inferred Indian monsoon precipitation over the past 252,000 y. *PNAS*, 112 (10), 2954-2959. https://doi.org/10.1073/pnas.1424035112

Cashman, S., Cashman, K. (2000). Cataclasis and deformation-band formation in unconsolidated marine terrace sand, Humboldt County, California. *Geology* 28, pp. 111–114. https://doi.org/10.1130/0091-7613(2000)28<111:CADFIU>2.0.CO;2

Cashman, S.M., Baldwin, J.N., Cashman, K.V., Swanson, K., Crawford, R., (2007). Microstructures developed by coseismic and aseismic faulting in near-surface sediments, San Andreas Fault, California. Geology 35, pp. 611 – 614. https://doi.org/10.1130/G23545A.1

Catuneanu, O., Abreu, V., Bhattacharya, J. P., Blum, M. D., Dalrymple, R. W., Eriksson, P. G., Fielding, C. R., Fisher, W. L., Galloway, W. E., Gibling, M. R., Giles, K. A., Holbrook, J. M., Jordan, R., Kendall, C. G. St. C., Macurda, B., Martinsen, O. J., Miall, A. D., Neal, J. E., Nummedal, D., Pomar, L., Posamentier, H. W., Pratt, B. R., Sarg, J. F., Shanley, K. W., Steel, R. J., Strasser, A., Tucker, M. E., & Winker, C. (2009). Towards the standardization of sequence stratigraphy. *Earth-Science Reviews*, 92, 1-33. doi:10.1016/j.earscirev.2008.10.003

Cilona, A.; Baud, P.; Tondi, E.; Agosta, F.; Vinciguerra, S.; Rustichelli, A.; Spiers, C., (2012). Deformation bands in porous carbonate grainstones: Field and laboratory observations. *J. Structural Geology* 45, pp. 137 – 157. https://doi.org/10.1016/j.jsg.2012.04.012

Collignon, M., Yamato, P., Castelltort, S., & Kaus, B. J. P. (2016). Modeling of wind gap formation and development of sedimentary basins during fold growth: application to the Zagros Fold Belt, Iran. *Earth Surface Processes and Landforms*, 41 (11), 1521-1535. https://doi.org/10.1002/esp.3921.

Corvinus, G. & Rimal, L. N. (2001). Biostratigraphy and geology of the Neogene Siwalik Group of Surai Khola and Rato Khola areas in Nepal. *Palaeogeography, Palaeoclimatology, Palaeoecology,* 165 (2001) 251–279. https://doi.org/10.1016/S0031-0182(00)00163-2

Dal Zilio, L., Hetényi, G., Hubbard, J. & Bollinger, L. (2021). Building the Himalaya from tectonic to earthquake scales. *Nature Reviews Earth & Environment,* 2, 251–268. https://doi.org/10.1038/s43017-021-00143-1

Dasgupta, S., Mazumdar, K., Moirangcha, L. H., Gupta, T. D., & Mukhopadhyay, B. (2013). Seismic landscape from Sarpang re-entrant, Bhutan Himalaya foredeep, Assam, India: Constraints from geomorphology and geology. *Tectonophysics*, 592, 130-140. http://dx.doi.org/10.1016/j.tecto.2013.02.021

Deal, E., Favre, A. C., & Braun, J. (2017). Rainfall variability in the Himalayan orogen and its relevance to erosion processes. *Water Resources Research*, 53, 4004-4021. doi:10.1002/2016WR020030.

DeCelles, P. G., & Cavazza, W. (1999). A comparison of fluvial megafans in the Cordilleran (Upper Cretaceous) and modern Himalayan foreland basin systems. *GSA Bulletin*, 111 (9), 1315-1334.

Densmore, A. L., Sinha, R., Sinha, S., Tandon, S. K., & Jain, V. (2016). Sediment storage and release from Himalayan piggyback basins and implications for downstream river morphology and evolution. *Basin Research*, 28, 446-461. doi: 10.1111/bre.12116

Dey, S., Thiede, R. C., Schildgen, T. F., Wittmann, H., Bookhagen, B., Scherler, D., Jain, V., & Strecker, M. R. (2016). Climate-driven sediment aggradation and incision since the late Pleistocene in the NW Himalaya, India. *Earth and Planetary Science Letters*, 449, 321-331. http://dx.doi.org/10.1016/j.epsl.2016.05.050

Dingle, E. H., Attal, M., & Sinclair, H. D. (2017). Abrasion-set limits on Himalayan gravel flux. *Nature*, 544, 471-482. doi:10.1038/nature22039

Dhital, M. R. (2015). Geology of the Nepal Himalaya, Regional perspective of the classic collided orogen. Regional Geology Reviews, Springer International publishing, Switzerland. DOI 10.1007/978-3-319-02496-7.

Duncan, J.A., King, G.E., & Duller, G.A.T. (2015). DTAC: Dose Rate and Age Calculator for trapped charge dating. Quaternary Geochronology, 28, 54-61.

Dutt, S., Gupta, A. K., Clemens, S. C., Cheng, H., Singh, R. K., Kathayat, G., & Edwards, R. L. (2015). Abrupt changes in Indian summer monsoon strength during 33,800 to 5500 years B.P. *Geophysical Research Letters*, 42, 5526-5532, doi:10.1002/2015GL064015.

Dutta, S., Suresh, N., & Kumar, R. (2012). Climatically controlled late Quaternary terrace staircase development in the fold-and-thrust belt of the Sub Himalaya. *Palaeogeography, Palaeoclimatology, Palaeoecology*, 356-357, 16-26. doi:10.1016/j.palaeo.2011.05.006

Farquhar, G.D., O'leary, M.H., & Berry, J.A. (1982). On the relationship between carbon isotope discrimination and the intercellular carbon dioxide concentration in leaves. *Funct. Plant Biol*. 9 (2), 121e137.

Finnegan, N. J., Sklar, L. S., & Fuller, T. K. (2007). Interplay of sediment supply, river incision, and channel morphology revealed by the transient evolution of an experimental bedrock channel. *Journal of Geophysical Research.* 112, F03S11, doi:10.1029/2006JF000569

Fleitmann, D., Burns, S. J., Mudelsee, M., Neff, U., Kramers, J., Mangini, A., Matter, A. (2003). Holocene forcing of the Indian monsoon recorded in a stalagmite from southern Oman. *Science*, 300 (5626), 1737-1739. DOI: 10.1126/science.1083130

Fleitmann, D., Burns, S. J., Mangini, A., Mudelsee, M., Kramers, J., Villa, I., Neff, U., Al-Subbary, A. A., Buettner, A., Hippler, D. & Matter, A. (2007). Holocene ITCZ and Indian monsoon dynamics recorded in stalagmites from Oman and Yemen (Socotra). *Quaternary Science Reviews*, 26, 170-188. doi:10.1016/j.quascirev.2006.04.012

Fossen, H., Schultz, R. A., Shipton, Z. K. & Mair, K. (2007). Deformation bands in sandstone: a review. *Journal of the Geological Society, London*, 164, 755-769.

Gaillard, C., Singh, M., & Malassé, A. D. (2011). Late Pleistocene to early Holocene lithic industries in the southern fringes of the Himalaya. *Quaternary International*, 229,112-122. doi:10.1016/j.quaint.2010.06.023

Gibling, M. R., Tandon, S. K., Sinha, R., & Jain, M. (2005). Discontinuity-bounded alluvial sequences of the southern Gangetic plains, India: Aggradation and degradation in response to monsoonal strength. *Journal of Sedimentary Research*, 75 (3), 369-385. DOI 10.2110/jsr.2005.029

Goodbred S. L. & Kuehl, S. A. (2000a). The significance of large sediment supply, active tectonism, and eustasy on margin sequence development: Late Quaternary stratigraphy and evolution of the Ganges-Brahmaputra delta. *Sedimentary geology*, 133, 227-248. https://doi.org/10.1016/S0037-0738(00)00041-5

Goodbred, S. L. & Kuehl, S. A. (2000b). Enormous Ganges-Brahmaputra sediment discharge during strengthened early Holocene monsoon. *Geology*, 28 (12), 1083-1086. https://doi.org/10.1130/0091-7613(2000)28<1083:EGSDDS>2.0.CO;2

Goodbred, S. L., Paolo, P. M., Ullah, M. S., Pate, R. D., Khan, S. R., Kuehl, S. A., Singh, S. K., & Rahaman, W. (2014). Piecing together the Ganges-Brahamputra-Meghna River delta: Use of sediment provenance to reconstruct the history and interaction of multiple fluvial systems during Holocene delta evolution. *GSA Bulletin*, 126 (11/12), 1495-1510. doi: 10.1130/B30965.1.

Harrison, S. P., Kohfeld, K. E., Roelandt, C., & Claquin, T. (2001). The role of dust in climate changes today, at the last glacial maximum and in future. *Earth Science Reviews,* 54: 43–80. https://doi.org/10.1016/S0012-8252(01)00041-1

Hey, R. D., & Thorne, C. R. (1986). Stable channels with mobile beds. *Journal of*

Hydraulic Engineering, v. 112, p. 671–689.

Hirschmiller, J., Grujic, D., Bookhagen, B., Coutand, I., Huyghe, P., Mugnier, J. L., & Ojha, T. (2014). What controls the growth of the Himalayan foreland fold-and-thrust belt? *Geology*, 42 (3), 247-250. doi:10.1130/G35057.1

Holcomb, D.J. & Olsson, W.A. 2003. Compaction localization and fluid flow. *Journal of Geophysical Research*, 108(B6), 2290. https://doi.org/10.1029/2001JB000813

Iseya, F. (1989). Mechanism of inverse grading of suspended load deposits. In: Taira, A., Masuda, F. (Eds.), *Sedimentary Facies in the Active Plate Margin*, pp. 113–129.

Jain, M. & Singhvi, A. K. (2001). Limits to depletion of blue-green light stimulated luminescence in feldspars: implications for quartz dating. *Radiation Measurements*, 33 (6), 883-892. https://doi.org/10.1016/S1350-4487(01)00104-4

Kaproth, B., Cashman, S., Marone, C., (2010). Deformation band formation and strength evolution in unlithified sand: The role of grain breakage. *J. Geophysical Research* B 115, B12103. Doi:10.1029/2010JB007406.

Kar, R., Chakraborty, T., Chakraborty, C., Ghosh, P., Tyagi, A. K., & Singhvi, A. K. (2014). Morpho-sedimentary characteristics of the Quaternary Matiali fan and associated river terraes, Jalpaiguri, India: Implications for climatic controls. *Geomorphology*, 227, 137-152. http://dx.doi.org/10.1016/j.geomorph.2014.05.014

Kathayat, G., Cheng, H., Sinha, A., Spötl, C., Edwards, R. L., Zhang, H., Li, X., Yi, L., Ning, Y., Cai, Y., Lui, W. L., & Breitenbach, S. F. (2016). Indian monsoon variability on millennial-orbital timescales. *Scientific Reports*, 6: 24374, DOI: 10.1038/srep24374

Kohn, M.J., 2010. Carbon isotope compositions of terrestrial C3 plants as indicators of (paleo) ecology and (paleo) climate. Proc. Natl. Acad. Sci. 107 (46),19691e19695.

Kotlia, B. S., Sharma, C., Bhalla, M. S., Rajagopalan, G., Subrahmanyam, K., Bhattacharyya, A., & Valdiya, K. S. (2000). Paleoclimatic conditions in the late Pleistocene Wadda Lake, eastern Kumaun Himalaya (India). *Paleogeography, Paleoclimatology, Paleoecology*, 162, 105-118.

Kotlia, B. S., Sanwal, J., & Bhattacharya, S. K. (2008). Climatic record between ca. 31 and 22 ka BP in East-Central Uttarkhand Himalaya, India. *Himalayan Geology*, 29 (1), 25-33.

Kotlia, B. S., Sanwal, J., Phartiyal, B., Joshi, L. M., Trivedi, A., & Sharma, C. (2010). Late Quaternary climatic changes in the eastern Kumaun Himalaya, India, as deduced from multi-proxy studies. *Quaternary International*, 213, 44-55. doi:10.1016/j.quaint.2009.09.002

Kumar, R., Suresh, N., Sangode, S. J., & Kumaravel, V. (2007). Evolution of the

Quaternary alluvial fan system in the Himalayan foreland basin: Implications for tectonic and climatic decoupling. *Quaternary International*, 159, 6-20. doi:10.1016/j.quaint.2006.08.010.

Larson, K.M., Burgmann, R., Bilham, R., & Freymueller, J.T. (1999). Kinematics of the India-Eurasia collision zone from GPS measurements. *Journal of Geophysical Research: Solid Earth,* 104 (B1), 1077–1093. https://doi.org/10.1029/1998JB900043

Lavé, J. & Avouac, J.-P. (2000). Active folding of fluvial terraces across the Siwaliks Hills, Himalayas of central Nepal. *Journal of Geophysical Research*,105, 5735−5770. https://doi.org/10.1029/1999JB900292

Lavé, J. & Avouac, J.-P. (2001). Fluvial incision and tectonic uplift across the Himalayas of central Nepal. *Journal of Geophysical Research*, 106, B11, 26561-26591. https://doi.org/10.1029/2001JB000359

Lavé, J., Yule, D., Sapkota, S., Basant, K., Madden, C., Attal, M. & Pandey, R. (2005). Evidence for a great medieval earthquake (~1100 A.D.) in the central Himalayas, Nepal. *Science*, 307, 1302-1305. 10.1126/science.1104804

Liu, Y., Hubbard, J., Almeida, R. V., Foster, A., Liberty, L., Lee, Y. S., & Sapkota, S. N. (2020). Constraints on the shallow deformation around the Main Frontal Thrust in central Nepal from refraction velocities. *Tectonophysics*, 777, 228366. https://doi.org/10.1016/j.tecto.2020.228366

Manning, M. P. & Reid, R. C. (1977). CHO systems in the presence of an iron catalyst. *Industrial and Engineering Chemistry Process Design and Development,* 16(3):358–6.

Mejdahl, V. (1979). Thermoluminescence dating: beta attenuation inquartz grains. Archaeometry 21, 61–73.

Murray, A.S. and Wintle, A.G. (2000). Luminescence dating of quartz using an improved single-aliquot regenerative-dose protocol. *Radiation Measurements,* 32(1): pp57-73.

Murray, A.S. and Wintle, A.G. (2003). The single aliquot regenerative dose protocol: potential for improvements in reliability. *Radiation Measurements,* 37(4-5): pp377-381.

Nakata, T., Kimura, K., & Rockwell, T. (1998). First successful paleoseismic trench study on active faults in the Himalaya. *Eos, Transactions,* American Geophysical Union, 79, 615.

O'Leary, M.H. (1981). Carbon isotope fractionation in plants. *Phytochemistry* 20 (4),553e567.

Osmond, C.B.,Winter, K., & Ziegler, H. (1982). Functional significance of different pathways of CO2 fixation in photosynthesis. In: Lange, O.L., Nobel, P.S., Osmond, C.B., Ziegler, H. (Eds.), *Physiological Plant Ecology II*. Springer, Berlin, pp. 481e499p.

Owen, L. A., Finkel, R. C., & Caffee, M. W. (2002). A note on the extent of glaciation throughout the Himalaya during the global Last Glacial Maximum. *Quaternary Science Reviews*, 21, 147-157. https://doi.org/10.1016/S0277-3791(01)00104-4

Owen, L. A., & Benn, D. I. (2005). Equilibrium-line altitudes of the Last Glacial Maximum for the Himalaya and Tibet: an assessment and evaluation of results. *Quaternary International*, 138-139, 55-78. doi:10.1016/j.quaint.2005.02.006

Owen, L. A. (2009). Latest Pleistocene and Holocene glacier fluctuations in the Himalaya and Tibet. *Quaternary Science Reviews*, 28, 2150-2164. doi:10.1016/j.quascirev.2008.10.020

Pant, R. K., Basavaiah, N., Juyal, N., Saini, N. K., Yadava, M. G., Appel, E., & Singhvi, A. K. (2005). A 20-ka climate record from Central Himalayan loess deposits. *Journal of Quaternary Science*, 20 (5), 485-492. DOI: 10.1002/jqs.938

Parker, G. (1978). Self-formed straight rivers with equilibrium banks and mobile bed. Part 2. The gravel river. *Journal of Fluid Mechanics*, v. 89, p. 127–146.

Pickering, J. L., Goodbred, S. L., Reitz, M. D., Hartzog, T. R., Mondal, D. R., & Hossain,

M. S. (2014). Late Quaternary sedimentary record and Holocene channel avulsions of the Jamuna and old Brahmaputra river valleys in the upper Bengal delta plain. *Geomorphology*, 227, 123-136. http://dx.doi.org/10.1016/j.geomorph.2013.09.021

Pickering, J. L., Goodbred, S. L., Beam, J. C., Ayers, J. C., Covey, A. K., Rajapara, H. M., & Singhvi, A. K. (2017). Terrace formation in the upper Bengal basin since the middle Pleistocene: Brahmaputra fan delta construction during multiple highstands. *Basin Research*, 1-18. doi: 10.1111/bre.12236

Pizzati, M., Balsamo, F., Storti, F., (2020). Displacement-dependent microstructural and petrophysical properties of deformation bands and gouges in poorly lithified sandstone deformed at shallow burial depth (Crotone Basin, Italy). *J. Structural Geology* 137, 104069 https://doi.org/10.1016/j.jsg.2020.104069

Plink-Björklund, P. (2015). Morphodynamics of rivers strongly affected by monsoon precipitation: Review of depositional style and forcing factors. *Sedimentary Geology*, 323, 110-147. http://dx.doi.org/10.1016/j.sedgeo.2015.04.004

Polach, H. A., & Golson, J. (1966). Collection of specimens for radiocarbon interpretation of results. Manual No. 2, Australian Institute of Aboriginal Studies, pp. 42.

Porat, N. (2006). Use of magnetic separation for purifying quartz for luminescence dating. *Ancient TL* 24(2): pp33-36.

Pourmand, A., Marcantonio, F., & Schulz, H. (2004). Variations in productivity and eolian fluxes in the northeastern Arabian Sea during the past 110 ka. *Earth and Planetary science Letters*, 221, 39-54. doi:10.1016/S0012-821X(04)00109-8

Pratt, B., Burbank, D. W., Heimsath, A., & Ojha, T. (2002). Impulsive alluviation during early Holocene strengthened monsoons, central Nepal Himalaya. *Geology*, 30 (10), 911-914. https://doi.org/10.1130/0091-7613(2002)030<0911:IADEHS>2.0.CO;2

Pratt, B., Burbank, D. W., Heimsath, A., & Ojha, T. (2004). Landscape disequilibrium on 1000-10,000 year scales Marsyandi River, Nepal, central Himalaya. *Geomorphology*, 58 (1-4), 223-241. https://doi.org/10.1016/j.geomorph.2003.07.002

Prescott, J.R., & Hutton, J.T. (1994). Cosmic ray contributions to dose rates for luminescence and ESR dating: Large depths and long-term time variations. *Radiation Measurements* **23**(2-3): pp497-500.

Ramsay, C. B. (2009). Bayesian analysis of radiocarbon dates. *Radiocarbon*, 51 (1), 337-360. https://doi.org/10.1017/S0033822200033865

Ray Y., & Srivastava, P. (2010). Widespread aggradation in the mountainous catchment of the Alaknanda-Ganga River System: timescales and implications to Hinterland-foreland relationships. *Quaternary Science Reviews*, 29, 2238-2260. doi:10.1016/j.quascirev.2010.05.023

Reimer, P., Bard, E., Bayliss, A., Beck, J., Blackwell, P., Ramsey, C., . . . Van der Plicht, J. (2013). IntCal13 and Marine13 Radiocarbon Age Calibration Curves 0–50,000 Years cal BP. *Radiocarbon, 55*(4), 1869-1887. doi:10.2458/azu_js_rc.55.16947

Reuther, J. D., Cherkinsky, A., & Coffman, S. (2017). Radiocarbon variation in charcoal/wood and soil fractions from a loessic setting in central Alaska. *Radiocarbon*, 59, 2, 449-464. DOI:10.1017/RDC.2016.41

Rizza, M., Bollinger, L., Sapkota, S. N., Tapponnier, P., Klinger, Y., Karakaş, Ç., Kali, E., Etchebes, M., Tiwari, D. R., Siwakoti, I., Bitri, A., & Bes de Berc, S. (2019). Post earthquake aggradation processes to hide surface ruptures in thrust systems: The M8. 3, 1934, Bihar-Nepal earthquake ruptures at Charnath Khola (Eastern Nepal). *Journal of Geophysical Research: Solid Earth*, 124(8), 9182-9207. https://doi.org/10.1029/2018JB016376

Rubin, D. M., Nelson, J. M., & Topping, D. J. (1998). Relation of inversely graded deposits to suspended-sediment grain-size evolution during the 1996 flood experiment in Grand Canyon. *Geology*, 26, 99–102.

Robinson, R. A. J. & Slingerland, R. L. (1998). Origin of fluvial grain-size trends in a foreland basin: the Pocono Formation on the Central Appalachian Basin. *Journal of Sedimentary Research,* 68 (3), 473-486. https://doi.org/10.2110/jsr.68.473

Sapkota, S.N., Bollinger, L., Klinger, Y., Tapponnier, P., Gaudemer, Y., & Tiwari, D. (2013). Primary surface ruptures of the great Himalayan earthquakes in 1934 and 1255. *Nature.Geoscience*, 6, 71–76. DOI:10.1038/NGEO1669

Sharma, S., Joachimski, M., Sharma, M., Tobschall, H. J., Singh, I. B., Sharma, C., Chauhan, M.S. & Morgenroth, G. (2004). Lateglacial and Holocene environmental changes in Ganges plain, Northern India. *Quaternary Science Reviews*, 23, 145-159. doi:10.1016/j.quascirev.2003.10.005

Shipton, Z.K. & Cowie, P.A. (2003). A conceptual model for the origin of fault damage zone structures in high-porosity sandstone. *Journal of Structural Geology*, 25, 333–345. https://doi.org/10.1016/S0191-8141(02)00037-8

Sinha, A., Cannariato, K. G., Stott, L. D., Li, H. C., You, C. F., Cheng, H., Edwards, R. L., & Singh, I. B. (2005). Variability of southwest Indian summer monsoon precipitation during the Bølling-A° llerød. *Geology*, 33 (10), 813-816, doi: 10.1130/G21498.1

Sinha, R., Bhattacharjee, P. S., Sangode, S. J., Gibling, M. R., Tandon, S. K., Jain, M., & Godfrey-Smith, D. (2007). Valley and interfluve sediments in the Southern Ganga plains, India: Exploring facies and magnetic signatures. *Sedimentary Geology*, 201, 386-411. doi:10.1016/j.sedgeo.2007.07.004

Sinha, S., Suresh, N., Kumar, R., Dutta, S., & Arora, B. R. (2010). Sedimentologic and geomorphic studies on the Quaternary alluvial fan and terrace deposits along the Ganga exit. *Quaternary International*, 227, 87-103. doi:10.1016/j.quaint.2009.09.015

Sinha, R., Ahmad, J., Gaurav, K., & Morin, G. (2014). Shallow subsurface stratigraphy and alluvial architecture of the Kosi and Gandak megafans in the Himalayan foreland basin, India. *Sedimentary Geology*, 301, 133-149. http://dx.doi.org/10.1016/j.sedgeo.2013.06.008

Skolasińska, K. (2014). Inquiry of levee formation by grain size analysis – A case study from the Warta River (central Poland). *Catena*, 122, 103-110. http://dx.doi.org/10.1016/j.catena.2014.06.014

Srivastava, P., Singh, I. B., Sharma, S., Shukla, U. K., & Singhvi, A. K. (2003a).. Late Pleistocene-Holocene hydrologic changes in the interfluve areas of the central Ganga Plain, India. *Geomorphology*, 54, 279-292. doi:10.1016/S0169-555X(02)00361-6

Srivastava, P., Singh, I. B., Sharma, M., & Singhvi, A. K. (2003b). Luminescence chronometry and late Quaternary geomorphic history of the Ganga Plain, India. *Palaeogeography, Palaeoclimatology, Palaeoecology,* 197, 15-41.

doi:10.1016/S0031-0182(03)00384-5

Srivastava, P., Rajak, M. K., & Singh, L.P. (2009). Late Quaternary alluvial fans and paleosols of the Kangra basin, NW Himalaya: Tectonic and paleoclimatic implications. *Catena*, 76, 135-154. doi:10.1016/j.catena.2008.10.004

Suresh, N., Bagati, T. N., Kumar, R., & Thakur, V. C. (2007). Evolution of Quaternary alluvial fans and terraces in the intramontane Pinjaur Dun, Sub-Himalaya, NW India: interaction between tectonics and climate change. *Sedimentology*, 54, 809-833. doi: 10.1111/j.1365-3091.2007.00861.x

Thakur, V.C., Joshi, M., Sahoo, D., Suresh, N., Jayangondapermal, R., & Singh, A. (2014). Partitioning of convergence in Northwest Sub-Himalaya: estimation of late Quaternary uplift and convergence rates across the Kangra reentrant, North India. *International Journal of Earth Sciences*,103, 1037–1056. http://dx.doi.org/10.1007/s00531-014-1016-7.

Tsukamoto, S., Asahi, K., Watanabe, T., & Rink, W. J. (2002). Timing of past glaciations in Kanchenjunga Himal, Nepal by optically stimulated luminescence dating of tills. *Quaternary International*, 97-98, 57-67. https://doi.org/10.1016/S1040-6182(02)00051-4

Ulak, P. D. (2009). Lithostratigraphy and late Cenozoic fluvial styles of Siwalik Group along Kankai River section, east Nepal Himalaya. *Bulletin of the Department of Geology, Tribhuvan University, Kathmandu, Nepal*, Vol. 12, 2009, pp. 63–74.

Vermeesch, P. (2009). Radial Plotter: a Java application for fission track, luminescence and other radial plots, *Radiation Measurements*, 44, 4, 409-410.

Vogel, J. S., Southon, J. R., Nelson, D. E., & Brown, T. A. (1984). Performance of catalytically condensed carbon for use in accelerator mass spectrometry. *Nuclear Instruments and Methods in Physics Research Section B: Beam Interactions with Materials and Atoms,* 5 (2), 289-293. https://doi.org/10.1016/0168-583X(84)90529-9

Wang, Y., Cheng, H., Edwards, R. L., He, Y., Kong, X., An, Z., Wu, J., Kelly, M. J., Dykoski, C. A., & Li, X. (2001). The Holocene Asian Monsoon: Links to solar changes and North Atlantic climate. *Science*, 308 (5723), 854-857. DOI: 10.1126/science.1106296

Wennbnerg, O., Casini, G., Jahanpanah, A., Lapponi, F., Ineson, J., Wall, B., Gilespie, P., (2013). Deformation bands in chalk, examples from the Shetland Group of the Oseberg Field, North Sea, Norway. *Journal of Structural Geology,* 56, pp. 103 – 117. https://doi.org/10.1016/j.jsg.2013.09.005

Wesnousky, S. G., Kumahara, Y., Chamlagain, D., Pierce, L. K., Karki, A., & Gautam, D.

(2017). Geological observations on large earthquakes along the Himalayan frontal fault near Kathmandu, Nepal. *Earth and Planetary Science Letters*, 457, 366-375. https://doi.org/10.1016/j.epsl.2016.10.006

Wesnousky, S. G. (2020). Great pending Himalaya earthquakes. *Seismological Research Letters*, 91 (6), 3334-3342. https://doi.org/10.1785/0220200200

Wickert, A. D., Martin, J. M., Tal, M., Kim, W., Sheets, B., & Paola, C. (2013). River channel lateral mobility: metrics, time scales, and controls. *Journal of Geophysical Research,* 118 (2), 396-412. https://doi.org/10.1029/2012JF002386

Willett, S. D., & Brandon, M. T. (2002). On steady states in mountain belts. *Geology*, 30 (2), 175-178. https://doi.org/10.1130/0091-7613(2002)030<0175:OSSIMB>2.0.CO;2

Wilson, J., Goodwin, L., Lewis, C., (2003). Deformation bands in nonwelded ignimbrites: Petrophysical controls on fault-zone deformation and evidence of preferential fluid flow. Geology 31, pp. 837 – 840. https://doi.org/10.1130/G19667R.1

Wintle, A.G. & Murray, A.S. (2006). A review of quartz optically stimulated luminescence characteristics and their relevance in single-aliquot regeneration dating protocols. *Radiation Measurements,* 41(4): pp369-391.

Wolff, E. W., Chappellaz, J., Blunier, T., Rasmussen, S. O., & Svensson, A. (2010).

Millennial-scale variability during the last glacial: The ice core record. *Quaternary Science Reviews*, 29, 2828-2838. doi:10.1016/j.quascirev.2009.10.013

Wu, Y., Wang, S., & Zhou, L. (2011). Possible factors causing older radiocarbon age for bulk organic matter in sediment from Daihai Lake, north China. *Radiocarbon*, 53, 2, 359-366. https://doi.org/10.1017/S0033822200056617

York, D., & Evensen, N. M. (2004). Unified equations for the slope, intercept, and standard errors of the best straight line. *American Journal of Physics*, 72 (3), 367. https://doi.org/10.1119/1.1632486

Geochemistry, Geophysics, Geosystems

Supporting Information for

Fluvio-sedimentary response to late Quaternary climate and tectonics at the Main Frontal Thrust, central Nepal

Mari Hamahashi[1†], Judith A. Hubbard[1, 2], Rafael Almeida[3], Samuel H. Haines[1],

Lewis A. Owen[4], Sanjita Mishra[5], and Soma Nath Sapkota[5]

[1]Earth Observatory of Singapore, Nanyang Technological University, Singapore

[2]Asian School of the Environment, Nanyang Technological University, Singapore

[3]Department of Geological Sciences, San Diego State University, USA

[4]Department of Marine, Earth, and Atmospheric Sciences, North Carolina State University, USA

[5]Department of Mines and Geology, National Seismological Center, Nepal

[†]Now at Kobe University, Kobe Ocean-Bottom Exploration Center, Japan

Contents of this file

Text S1 to S2

Figures S1 to S8

Additional Supporting Information (Files uploaded separately)

Captions for Datasets S1 to S2

Introduction

This supporting information contains detailed descriptions of the dating methodologies employed in this study, and additional descriptions of the outcrop terraces and bedrock surrounding our study area. Text S1 contains the description of optically stimulated luminescence (OSL) dating methodology. Text S2 contains the description of radiocarbon (^{14}C) dating methodology. Figure S1 shows the uninterpreted image of the Ratu river seismic profile (pre-stack depth-migrated, no vertical exaggeration) by Almeida et al. (2018) with co-located boreholes P6-P10 in this study. Figures S2 and S3 illustrate the features of bedrock Upper Siwalik Group and outcrop terraces surrounding our study area. Figure S4 shows regional satellite map of the Himalayan foreland and Ganges plain illustrating the rivers studied in this paper and the surrounding major rivers. Figures S5 and S6 show data of measured luminescence and equivalent dose of samples and the analysis of two-mixing model used to obtain OSL age. Figure S7 shows the calibration data of radiocarbon age to calendar years. Figure S8 shows the locations of previous studies in other foreland regions cited in this paper. Dataset S1 contains our core description data (raw data) presented in this paper. Dataset S2 contains the geotechnical report created by the drilling company.

Text S1. Optically stimulated luminescence (OSL) dating

Eighteen OSL samples were chosen from relatively well-sorted, silt to fine sand identified from surrounding cores at Sites P2, P3, P4, P6, P7, and P9, and were measured for quartz OSL at the University of Cincinnati and North Carolina State University in the USA. We avoided poorly-sorted fluvial sediment (sand with pebbles) due to risk of partial bleaching during fluvial transport, and selected well-sorted fluvial sediment (silty sand to clay). The samples were opened in the Luminescence Dating Laboratory under safe light conditions. The end of each sample (approximately 1 inch) was first removed, and were dried to determine water content. The sediment from the ends were then crushed and sent to the Activation Laboratories Limited in Ancaster, Ontario, Canada for Major Elements Fusion ICP/MS/Trace Elements analysis to determine the U, Th, Rb and K concentrations for dose rate calculations (Table 2).

The remaining samples were pretreated with 10% HCl and 10% H_2O_2 to remove carbonates and organic matter, respectively. The pretreated samples were rinsed in water, dried and sieved to obtain the 90-150 µm particle size fraction. A sub-fraction (~20 g) of each sample was etched using 44% HF acid for 80 minutes to remove the outer alpha irradiated layer from quartz particles. This treatment also helps dissolve any feldspars present. Any fluorides precipitated during HF treatment were removed using concentrated HCl for 30 min. The quartz samples were then rinsed in distilled water and acetate, and dried and sieved to obtain grain size 90-150 µm in diameter. Next, a low-field-controlled Frantz isodynamic magnetic separator (LFC Model-2) was used to separate feldspar and magnetic minerals from quartz in the 90-150 µm particle size fraction following the method of Porat (2006), with the forward and side slopes set at 100° and 10°, respectively, within a variable magnetic field. The quartz was sieved using a 90 µm mesh to remove any grains smaller than 90 µm, so that the 90-150 µm fraction could be used for OSL measurement.

An automated Riso OSL reader model TL-DA-20 was used for OSL measurements and irradiation. Aliquots, containing approximately several hundred grains of the samples, were mounted onto ~6 mm-diameter stainless steel discs as a small central circle of ~3 mm in diameter. Aliquots were first checked for feldspar contamination using infrared stimulated luminescence (IRSL) at room temperature before the main OSL measurements were undertaken (Jain and Singhvi, 2001). The samples that did not pass the IRSL test were etched in 40% HF for further 30 minutes to remove any feldspar, followed by 10% HCl treatment and sieving again. The samples then passed the IRSL test and was used for OSL dating. Aliquots of the samples were illuminated with blue LEDs stimulating at a wavelength of 470 nm (blue light stimulated luminescence). The detection optics comprised Hoya U-340 and Schott BG-39 color glass filters coupled to an EMI 9235 QA photomultiplier tube. The aliquots were irradiated using a $^{90}Sr/^{90}Y$ beta source. The single aliquot regeneration (SAR) method (Murray and Wintle, 2000; 2003) was used to determine the dose rate for age estimation. Only aliquots that satisfy the criterion of a recycling ratio not more than 10% were used in determining equivalent dose. A preheat of 240°C for 10 s was used and the OSL signal was recorded for 40 s at 125°C. OSL sensitivity of the samples had a high signal to noise ratio. Dose recovery tests (Wintle and Murray, 2006) indicate that a laboratory dose of 10 Gy could be recovered to within 10% by the SAR protocol, suggesting that the protocol was appropriate.

Table 2 presents the radioisotope, water content, and cosmic dose, dose rate, equivalent dose, and OSL age for the samples. Dose rate calculations follows the details highlighted in the captions of Table 2 and confirmed using the Dose Rate and Age Calculator (DRAC) of Duncan et al. (2015). The dose rates for the samples were 3.21±0.19 and 3.98±0.24 Gy/ka, which is within the normal range for terrestrial sediments. The Th/U ratio is consistent with there being no problems of leaching of radionuclides from the sediment. Natural water content was ~10%, and we assumed a conservative value with a large uncertainty (±5%) to account for any possible changes in water content over the geologic history.

The natural OSL signal for all aliquots were at least two orders of magnitude greater than background signal. The shine down curves (luminescence stimulated in the lab over 40 s of exposure to light) for all aliquots showed fast decay patterns that confirm that the signal is the fast component of luminescence, which is dominant in quartz. This provides confidence that quartz would have likely been bleached quickly if only briefly exposed to sunlight. Figure S3 shows an example of shine down curves for the dated samples. Figure S3 also shows examples of the regenerative curves, illustrating good growth and recuperation. Dose rate recovery tests for the samples showed that they have good recovery within the uncertainty of the laboratory measurement and 10% of the applied dose of 100 s.

At least thirty-two aliquots were measured for each sample. Of those several aliquots were saturated (»200 Gy), and many aliquots failed the recuperation (especially for sample P3-39) and recycling criteria (Table 2). The remaining aliquots were used to determining a likely equivalent dose for the sample (Table 2). The spread of equivalent dose varied between the samples and are shown in Figure S4. In all the samples (especially P3-39), the large spread of equivalent dose values (dispersion >25%) and the significant number of aliquots that were saturated suggests partial bleaching problems (i.e., not all the sand grains were totally rest by sunlight before burial). This can result in an overestimate of the age. To address this issue, we use a minimum age model separating the population of equivalent dose using a two-mixing model (Figure S4; Vermeesch, 2009), and we use the equivalent dose value of the minimum peak to calculate the age (Table 2 and Figure S4). This provides best estimation of ages (see ages highlighted in bold in Table 2). For completeness and comparison, the average and weighted averages ages are provided in Table 2. The average ages are overestimates because of partial bleaching issue and have large uncertainties associated with them, but all our data is included in those ages. The weighted averages skew the ages towards the lower range because of the smaller associated uncertainties with low value aliquots. These ages are similar to the two-mixing model ages, adding confidence in our two-mixing model ages (Table 2). In this study, we use average OSL ages for samples that showed ≤ 25% dispersion of the aliquots, and 2-mixing model OSL ages for samples that yielded > 25% dispersion (Table 2).

Text S2. Radiocarbon (^{14}C) dating

Fourteen samples of organic sediment were retrieved from the cores at Sites P2, P3, and P8, and measured for ^{14}C dating at Beta Analytics Inc., following standard laboratory procedures. Given the absence of charcoals and other macrofossils, the bulk organic fraction (carbon content: 0.06-1.62%) of less than 180 μm in size, inclusive of humic and humins, were used for dating. The samples were first visually inspected for size, homogeneity, debris, inclusions, clasts, grain size, organic constituents and potential contaminants, before they were dispersed in de-ionized water and sieved through a 180 μm mesh. The samples were then bathed in 1.25 N HCl at 90°C for a minimum of 1.5 hours to ensure removal of carbonates, followed by serial de-ionized water rinses at 70°C until neutrality was reached. Any debris or micro-rootlets were discarded during these rinses. After drying in an oven at 100°C for 12-24 hours, HCl was applied to a representative sub-sample under the microscope to validate the absence of carbonate. Microscopic examination was performed to assess its characteristics and to determine the appropriate sub-sample for AMS dating.

The pretreated samples were then oxidized to CO_2 by combustion at 1000-1200°C. The CO_2 generated was cryogenically purified by removing water vapor and any non-combustible/condensable gases, and were converted to graphite (Vogel et al., 1984; Manning and Reid, 1977). AMS counting was performed by charging the atoms in the sample graphite using NEC accelerator mass spectrometers. Stable isotope ratio ($^{13}C/^{12}C$ or $\delta^{13}C$) values were measured separately by Thermo isotope ratio mass spectrometers (IRMS). The conventional radiocarbon age was calculated using the Libby half-life (5568 years), and were corrected for total isotopic fractionation effects. Errors reported from the laboratory are based on 1 sigma counting statistics, and the conventional ages and their sigmas were rounded to the nearest 10 years. Calibration of the conventional age were performed using the 2013 calibration databases (INTCAL13) (Reimer et al., 2013), high probability density range method and Bayesian probability analysis (Ramsey, 2009) (Fig. S5).

$\delta^{13}C$ values of bulk organic fraction can be referred as a proxy to infer intensity of regional precipitation, in the recognition that differences in $\delta^{13}C$ values of plants are controlled by differences in metabolic processes in C_3 and C_4 plants (e.g. Kohn, 2010). It serves as a proxy because C_3 plants are generally known to flourish under moderate temperature and wet climate, compared to C_4 plants which favor cold and dry climate (e.g. O'Leary, 1981; Farquhar et al. 1982). $\delta^{13}C$ values of C_3 plants are reported to range between -35 and -22‰, whereas C_4 plants range between -20 and -9‰ (e.g. Osmond et al., 1982). In this study, we placed a cut-off around -15 to 20‰ to infer differences in C_3 and C_4 plants and climate.

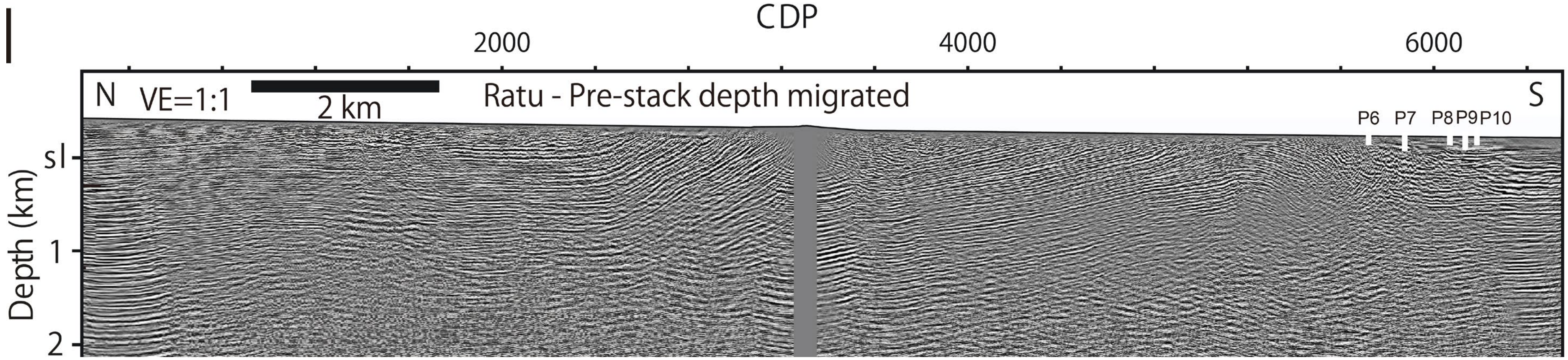
CDP
2000
4000
6000
N
VE=1:1
2 km
Ratu - Pre-stack depth migrated
S
P6
P7
P8
P9
P10
sl
1
2
Depth (km)

Figure S1. Ratu river seismic profile (pre-stack depth-migrated, no vertical exaggeration) by Almeida et al. (2018), uninterpreted image. CDP spacing is 2.5 m. Depth measurements are with respect to sea level (sl). White vertical bars show location of borehole sites P6–P10 in this study. Interpretation by Almeida et al. (2018) is shown in Figure 3a (main text).

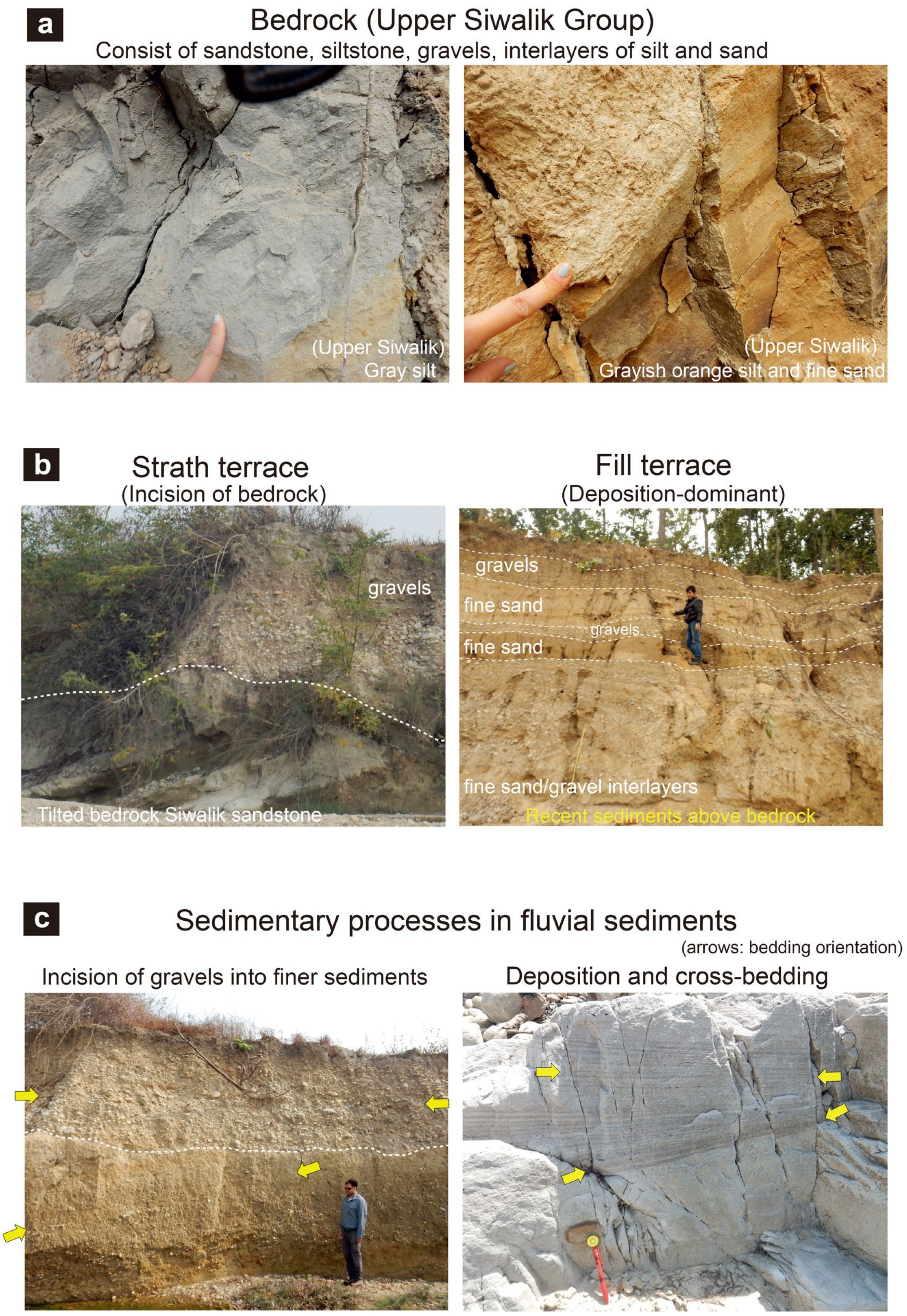
a
Bedrock (Upper Siwalik Group)
Consist of sandstone, siltstone, gravels, interlayers of silt and sand
(Upper Siwalik)
Gray silt
(Upper Siwalik)
Grayish orange silt and fine sand
b
Strath terrace
(Incision of bedrock)
gravels
Tilted bedrock Siwalik sandstone
Fill terrace
(Deposition-dominant)
gravels
fine sand
gravels
fine sand
fine sand/gravel interlayers
Recent sediments above bedrock
c
Sedimentary processes in fluvial sediments
(arrows: bedding orientation)
Incision of gravels into finer sediments
Deposition and cross-bedding

Figure S2. (a) Representative images of bedrock Upper Siwalik Group observed from the outcrops in the study area. Left panel: Gray silt (partially oxidized). Right panel: Grayish orange silt and fine sand. **(b)** Representative images of terrace outcrops in the study area. Left panel: Features of a strath terrace, showing tilted Upper Siwalik bedrock (sandstones) incised and buried by more recent fluvial sediments (gravels), bounded by white dotted line. Right panel: Features of a fill terrace, showing thick sequence of recent fluvial sediments, interbedded with fine sand/gravels (bounded by white dotted lines). The bedrock is not exposed in fill terraces. **(c)** Representative images of terrace outcrops showing sedimentary processes in fluvial sediments. Yellow arrows mark bedding orientations. Left panel: Beveled erosional surface between finer and coarser fluvial sediments. Right panel: Cross-bedding observed in sandstone.

Observation from outcrop terraces

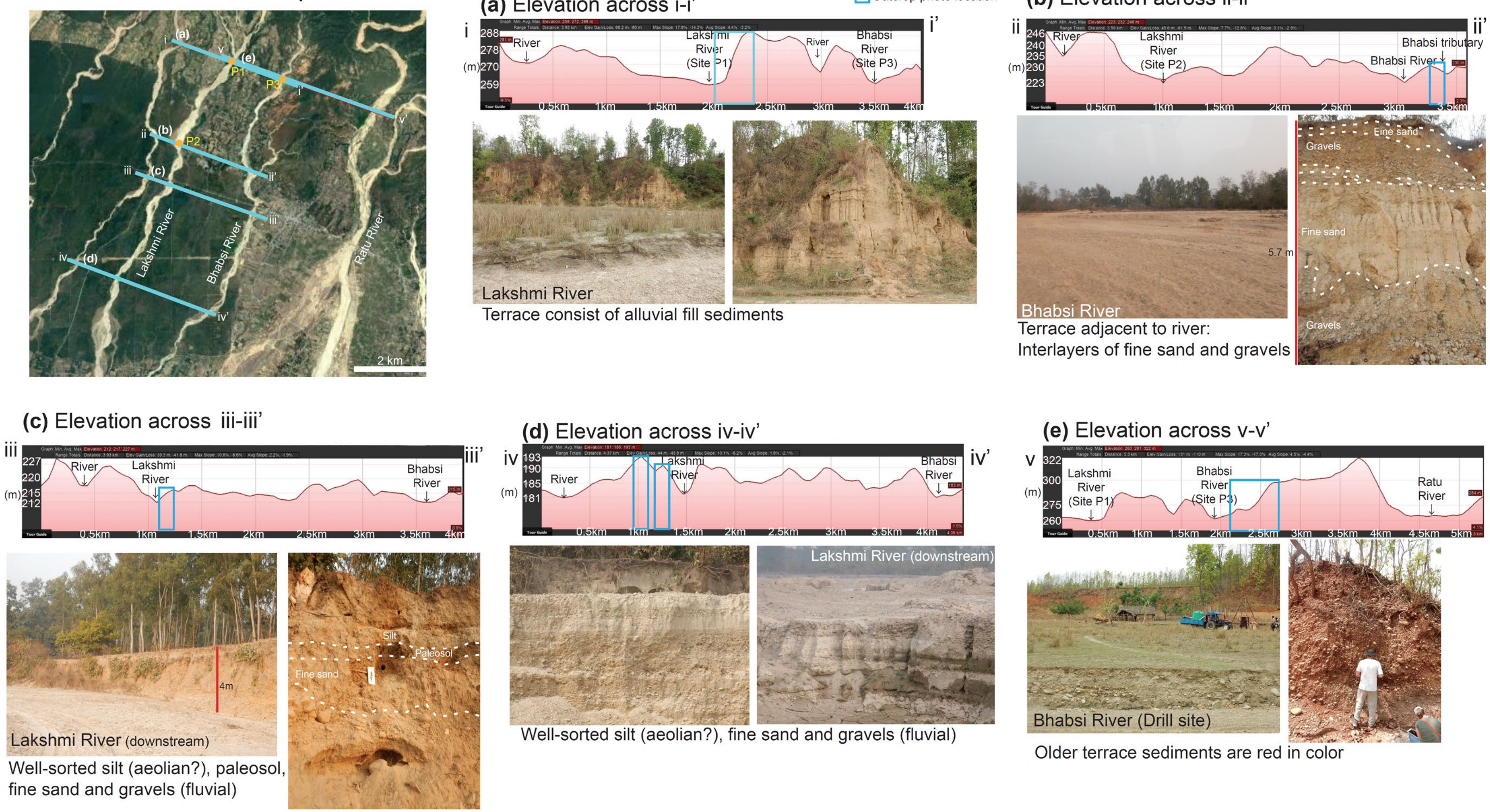

Figure S3. Views of exposures along river terraces surrounding borehole sites in this study. Map shows locations of borehole Sites P1-P3. Blue lines in map show locations of elevation profiles for (a)-(e). **(a)** Elevation profile across i-i′ and representative images of river terrace outcrops along the Lakshmi River (location is indicated in blue box in elevation profile). River terrace sediments consist of mainly alluvial fill sediments. **(b)** Elevation profile across i-ii′ and representative images of terrace outcrops along the Bhabsi River (location is indicated in blue box in elevation profile). River terrace sediments consist of interlayers of fine sand and gravels. **(c)** Elevation profile across iii-iii′ and representative images of terrace outcrops along the Lakshmi River (location is indicated in blue box in elevation profile). River terrace sediments consist of well-sorted silt, paleosol, fine sand and gravels. **(d)** Elevation profile across iv-iv′ and representative images of terrace outcrops along the Lakshmi River (location is indicated in blue box in elevation profile). Terrace sediments consist of well-sorted silt, fine sand and gravels. **(e)** Elevation profile across v-v′ and representative images of terrace outcrops along the Bhabsi River (location is indicated in blue box in elevation profile). Terrace consist of alluvial fill sediments.

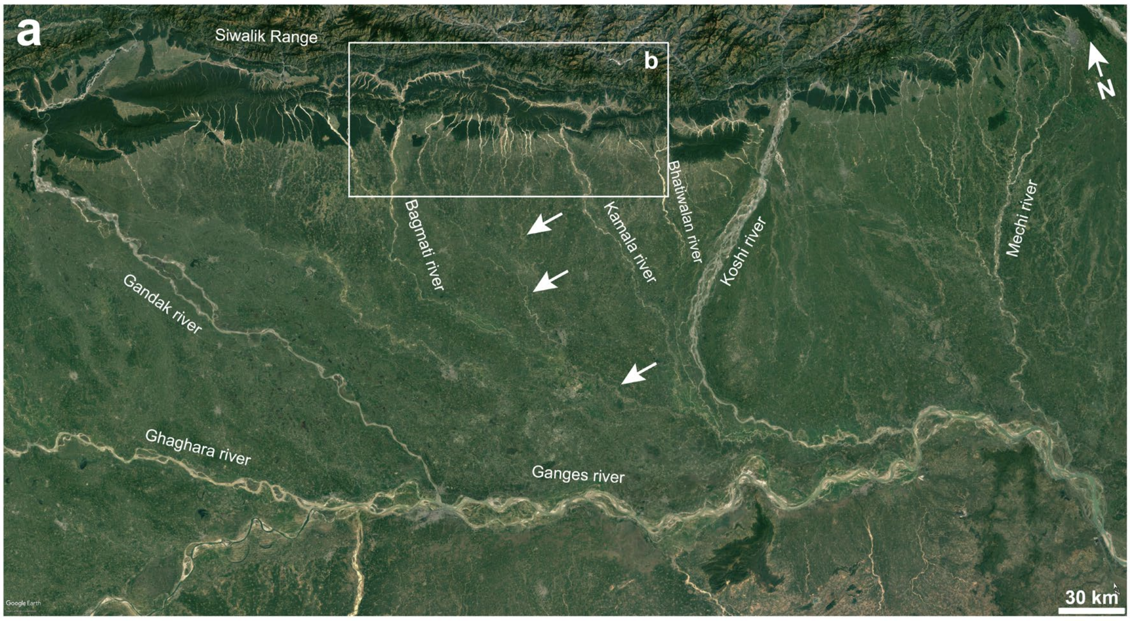

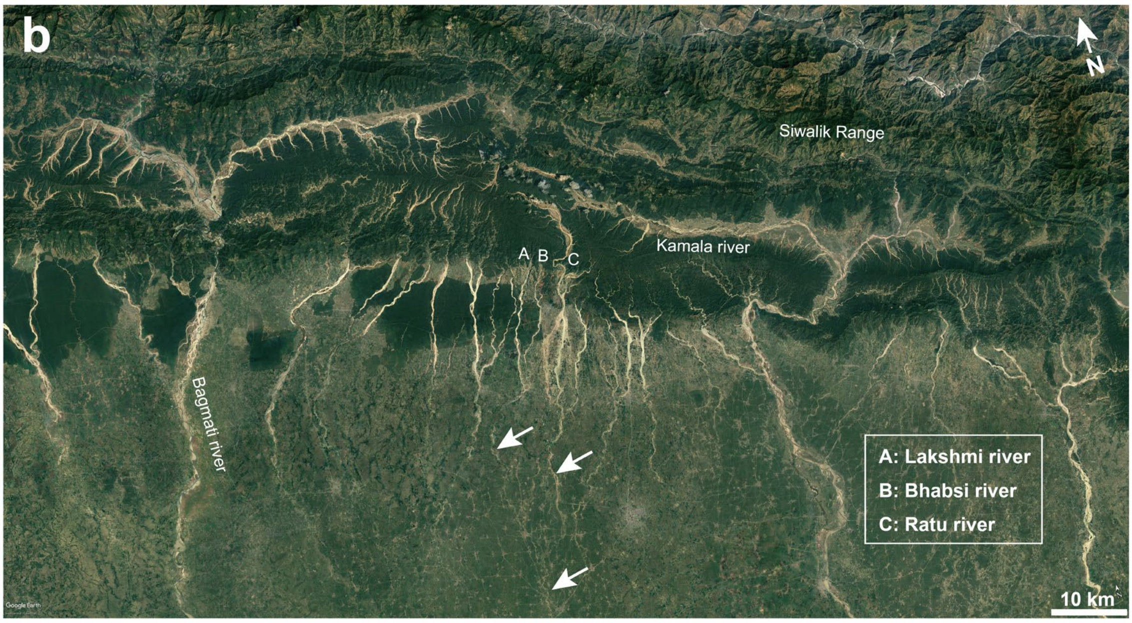

Figure S4. Regional satellite image showing the rivers studied in this paper and the surrounding major rivers flowing into the Himalayan foreland and to the Ganges plain. **(a)** In contrast to the major transverse Himalayan rivers such as the Koshi, Gandak, and the Ganges rivers, which have large drainage basins further upstream (High Himalaya), the drainage of the rivers in this study (white square closed-up in b.) are limited to the southern part of the Siwalik Range and are smaller ("footwall-fed rivers"). As the rivers travel hundreds of kilometers towards the southeast, their channel widths decrease (white arrows). Some of the channels are abandoned, while some merge with the Koshi and the Ganges rivers. **(b)** Close-up map showing the rivers in this study and their drainage basins within the Siwalik Range. A: Lakshmi river. B: Bhabsi river. C: Ratu river. The width of the rivers decreases downstream (white arrows). Satellite image uses map from Google Earth imagery, Image Landsat/Copernicus.

P3-31M

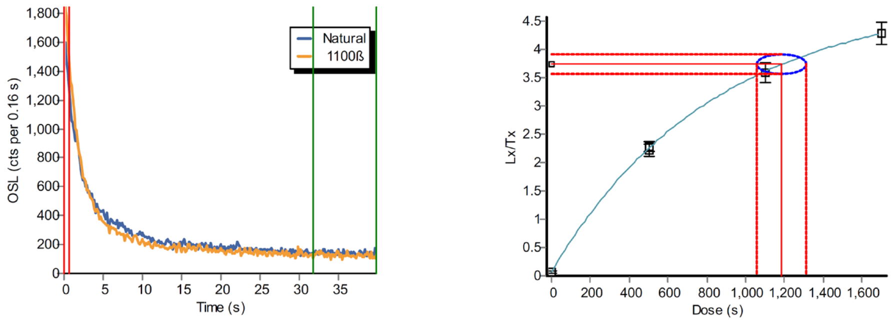

P3-39M

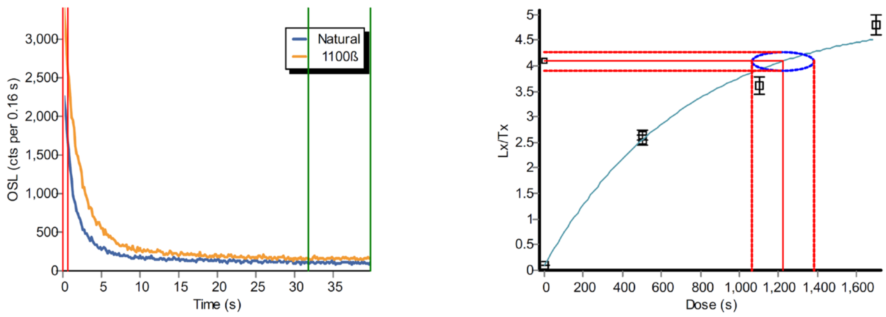

P3-41M

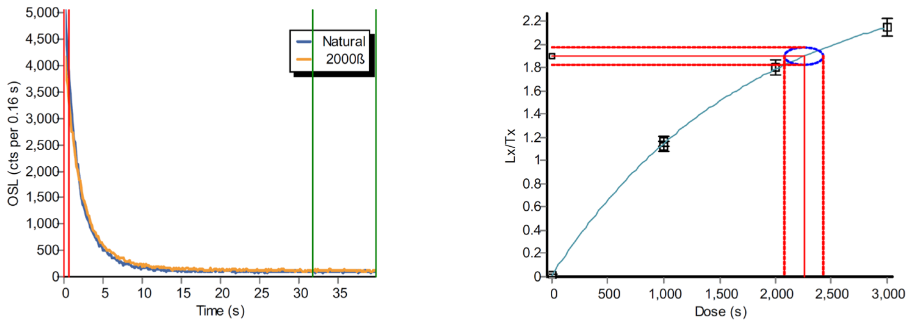

P3-49M

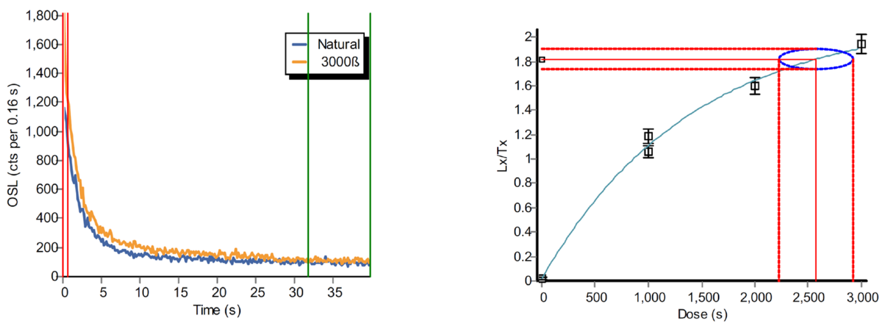

P2-23m

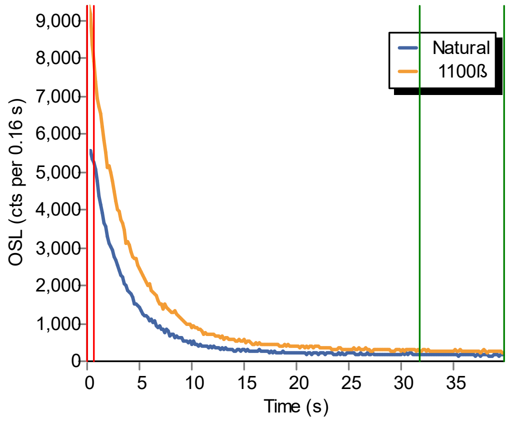

OSL (cts per 0.16 s)
Time (s)
Natural
1100ß

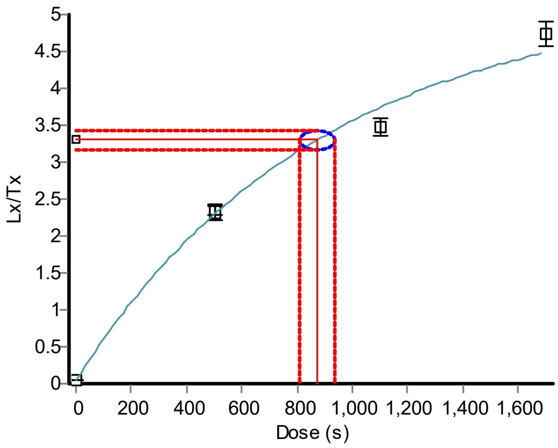

Lx/Tx
Dose (s)

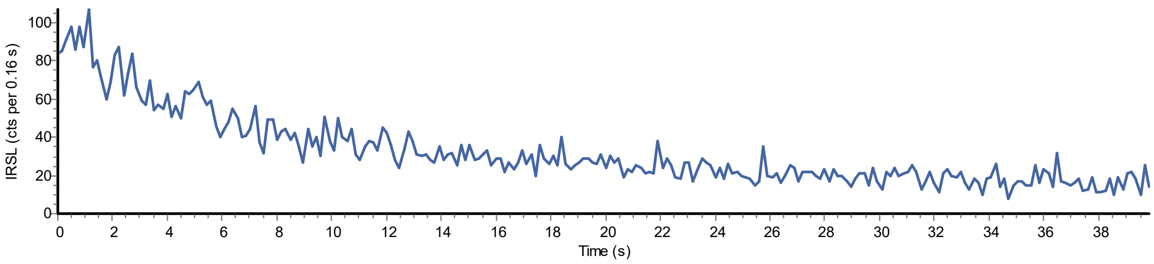

IRSL (cts per 0.16 s)
Time (s)

P2-27m

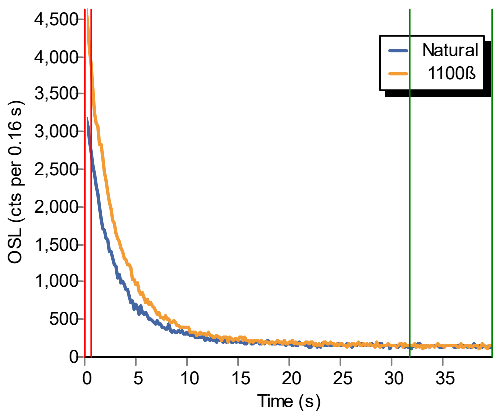

OSL (cts per 0.16 s)
Time (s)
Natural
1100ß

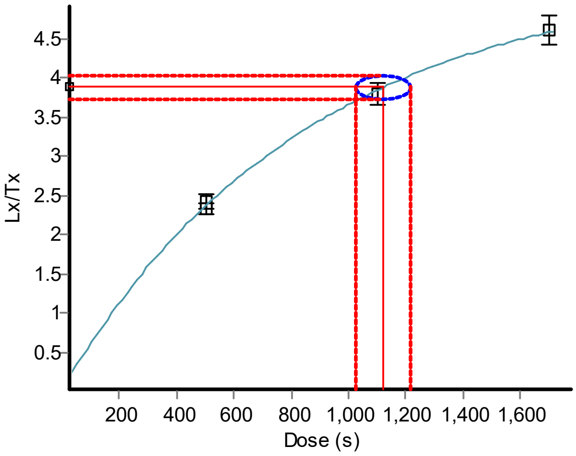

Lx/Tx
Dose (s)

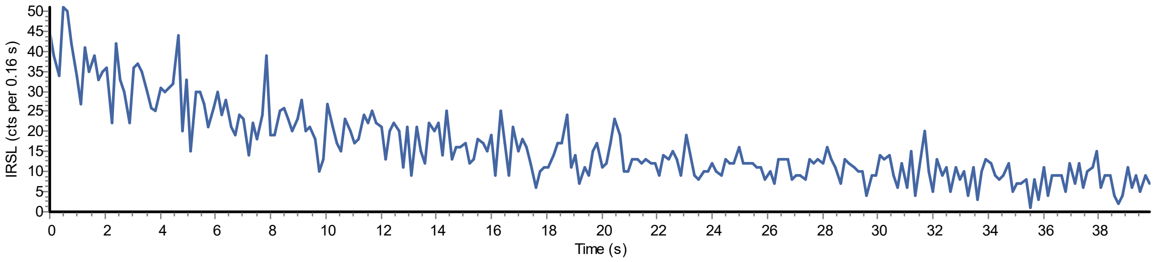
IRSL (cts per 0.16 s)
Time (s)

P2-31m

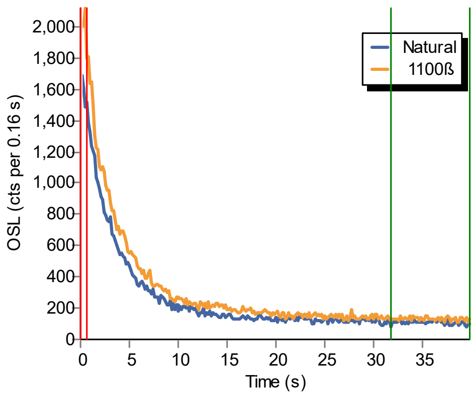
OSL (cts per 0.16 s)
Natural
1100ß
Time (s)

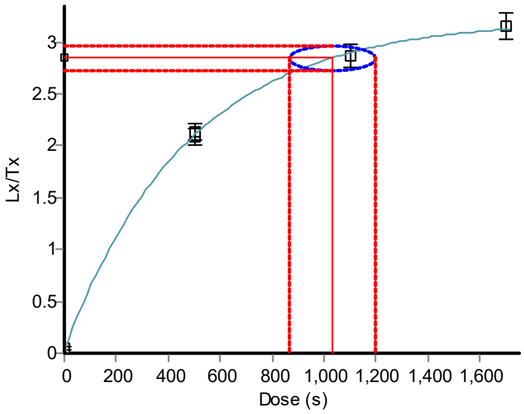
Lx/Tx
Dose (s)

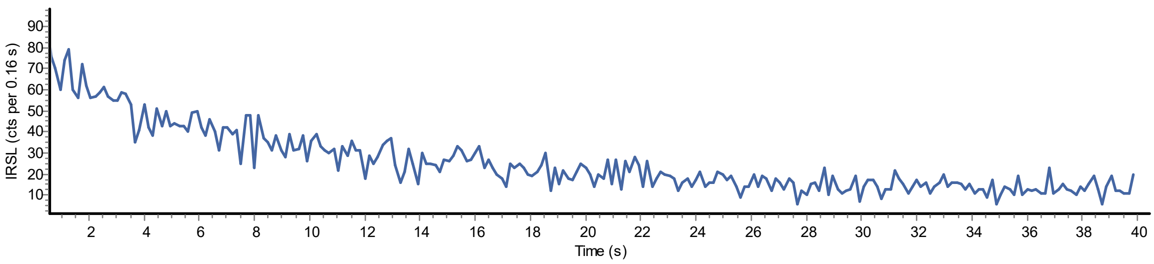
IRSL (cts per 0.16 s)
Time (s)

P2-31 (Representative saturated curve)

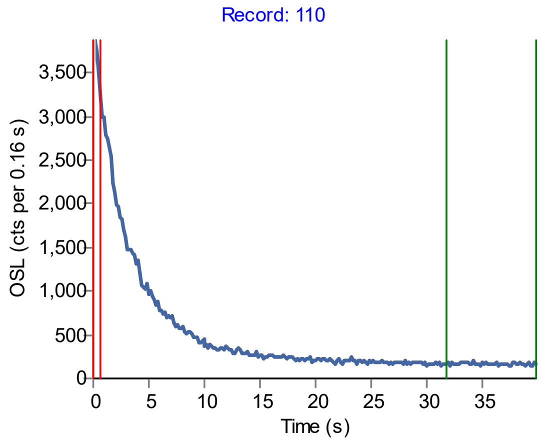

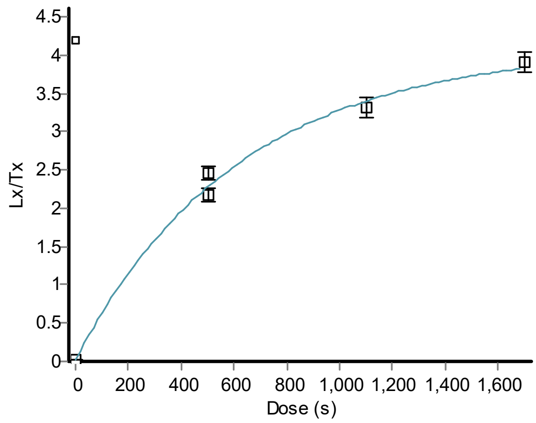

P2-41m

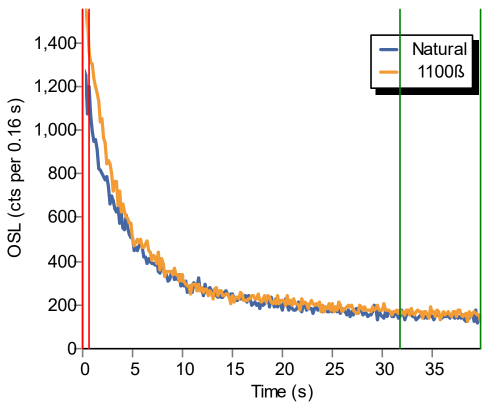

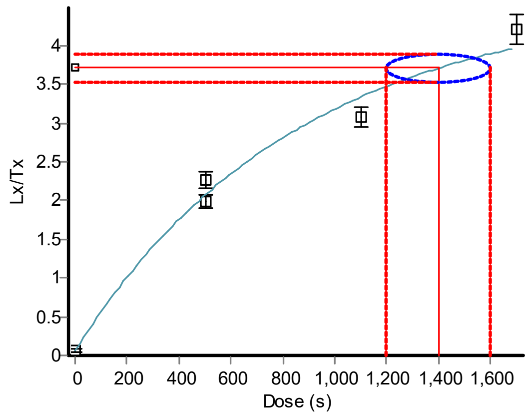

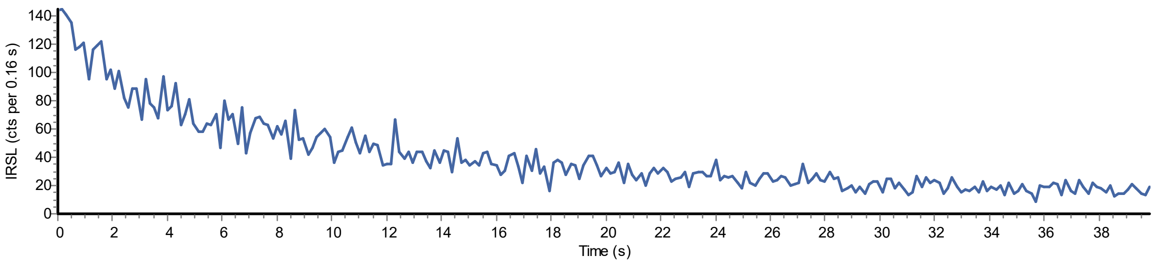

P2-41 (Representative saturated curve)

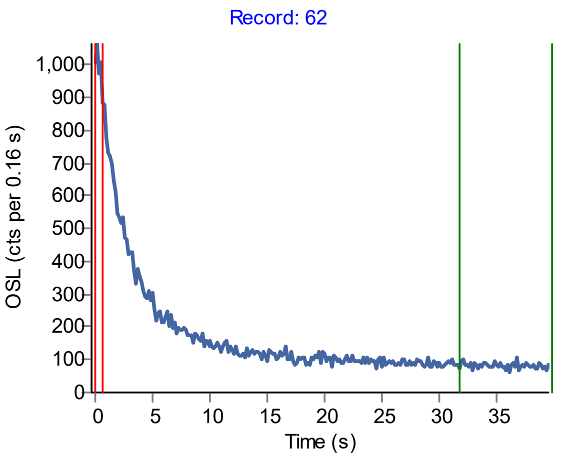

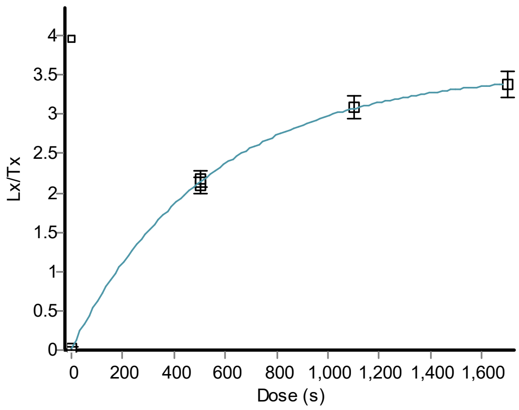

P3-29m

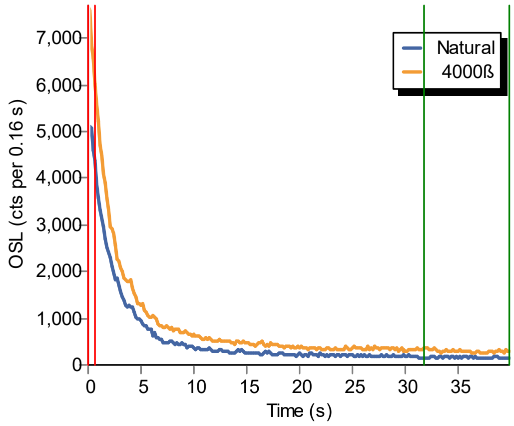
OSL (cts per 0.16 s)
Time (s)
Natural
4000ß

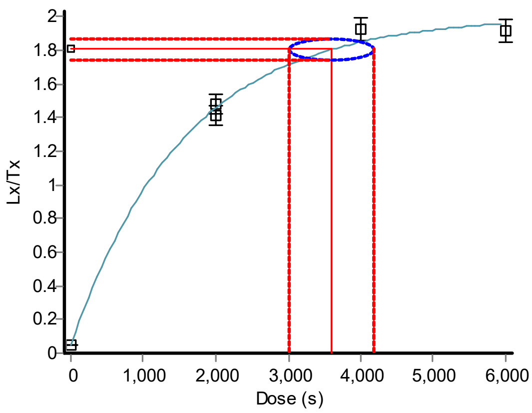
Lx/Tx
Dose (s)

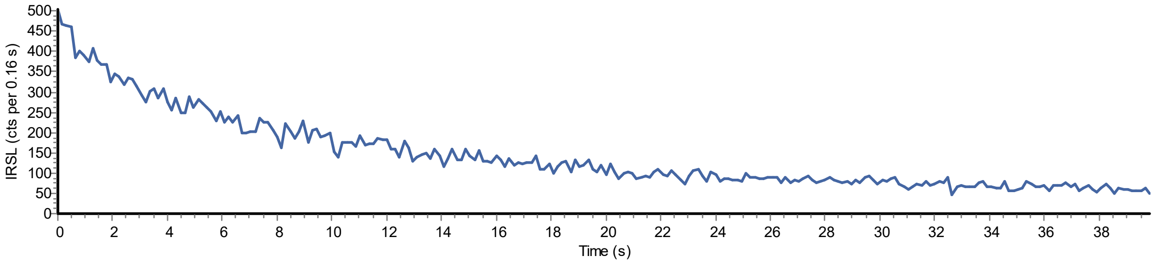
IRSL (cts per 0.16 s)
Time (s)

P4-51m

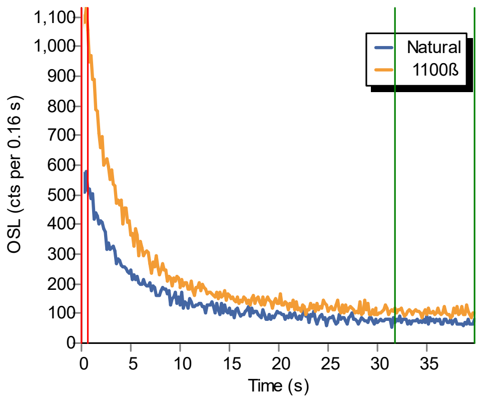
OSL (cts per 0.16 s)
Time (s)
Natural
1100ß

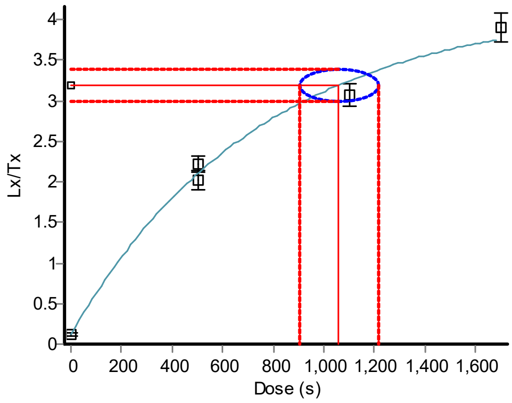
Lx/Tx
Dose (s)

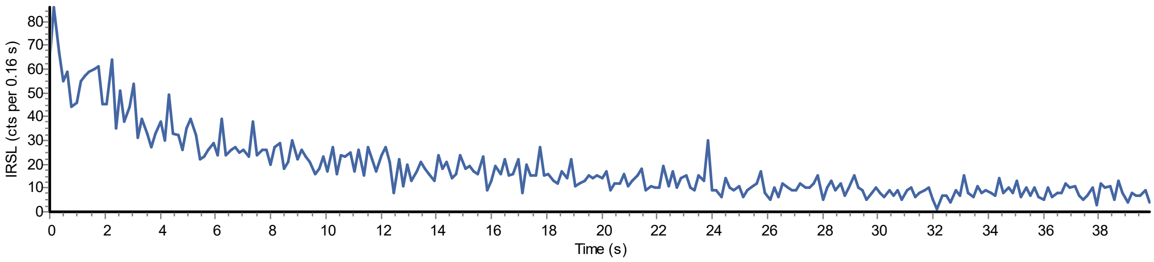
IRSL (cts per 0.16 s)
Time (s)

P4-69m

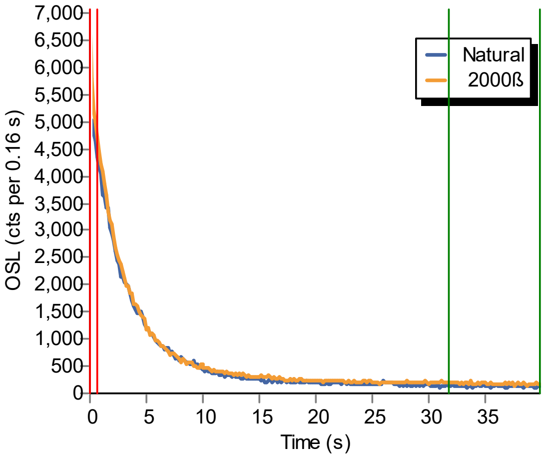
OSL (cts per 0.16 s)
Time (s)
Natural
2000ß

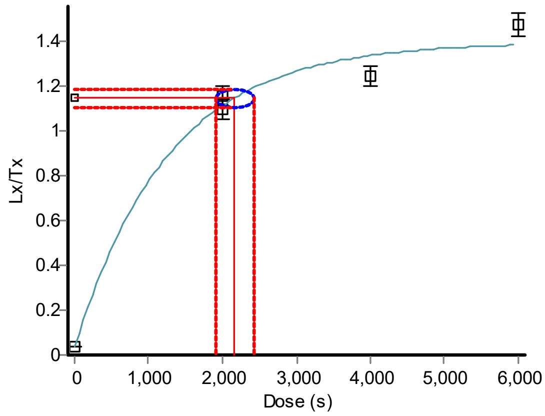
Lx/Tx
Dose (s)

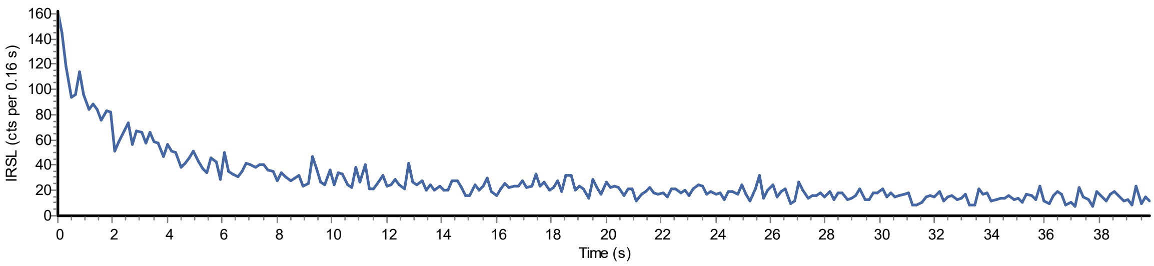
IRSL (cts per 0.16 s)
Time (s)

P4-99m

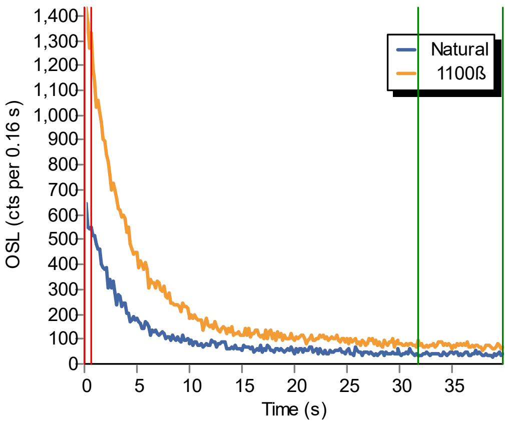

OSL (cts per 0.16 s)
1,400
1,300
1,200
1,100
1,000
900
800
700
600
500
400
300
200
100
0
Natural
1100ß
0
5
10
15
20
25
30
35
Time (s)

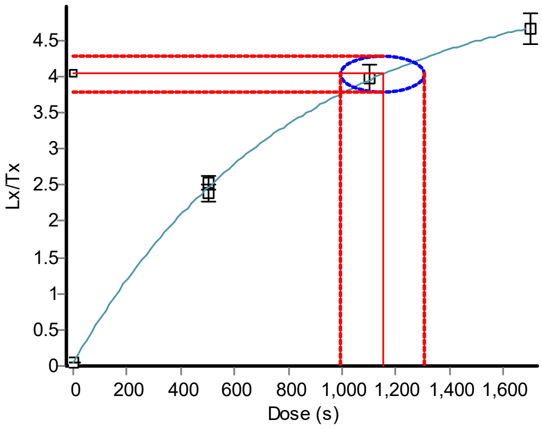

Lx/Tx
4.5
4
3.5
3
2.5
2
1.5
1
0.5
0
0
200
400
600
800
1,000
1,200
1,400
1,600
Dose (s)

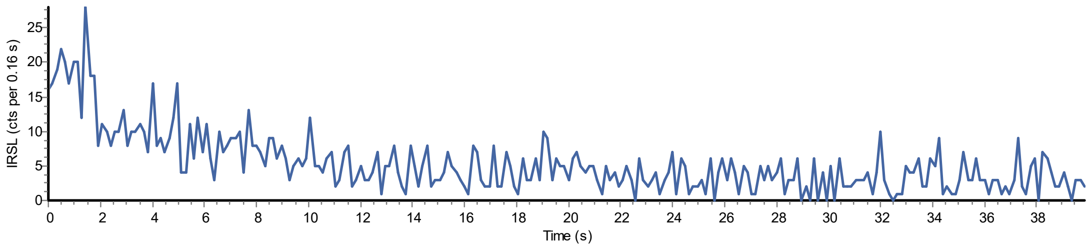

IRSL (cts per 0.16 s)
25
20
15
10
5
0
0
2
4
6
8
10
12
14
16
18
20
22
24
26
28
30
32
34
36
38
Time (s)

P6-19m

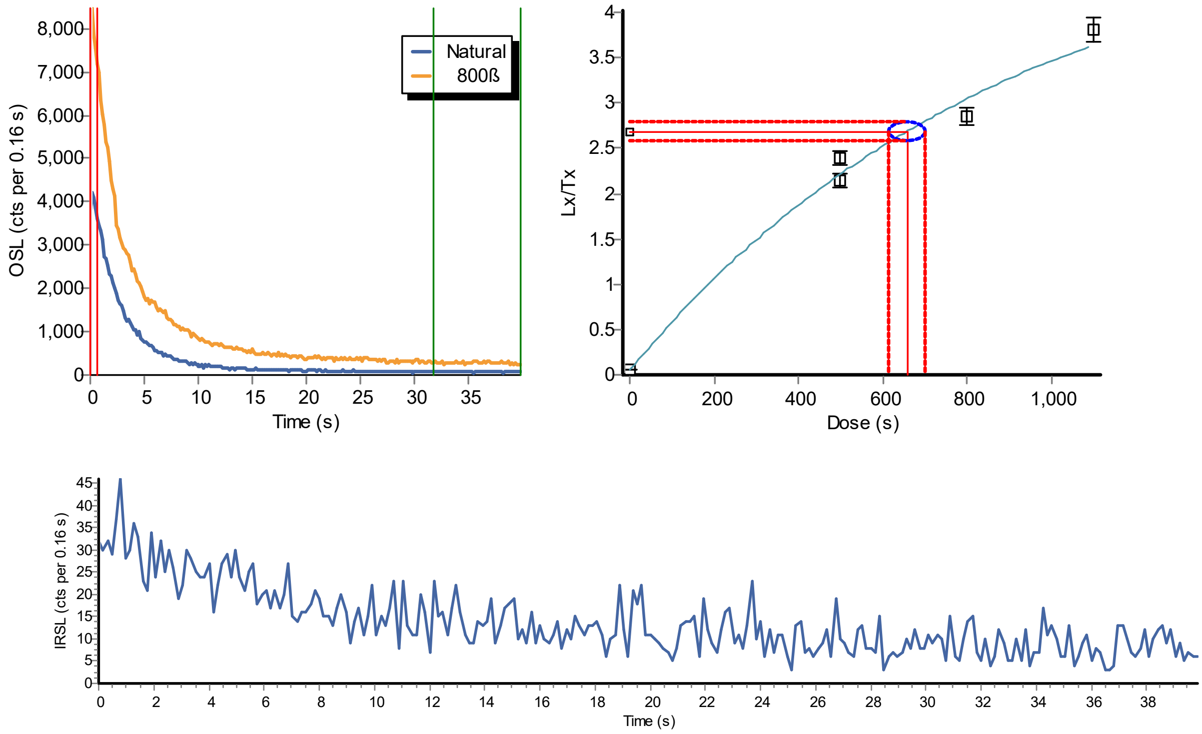
Natural
800ß
OSL (cts per 0.16 s)
Time (s)
Lx/Tx
Dose (s)
IRSL (cts per 0.16 s)
Time (s)

P6-33m

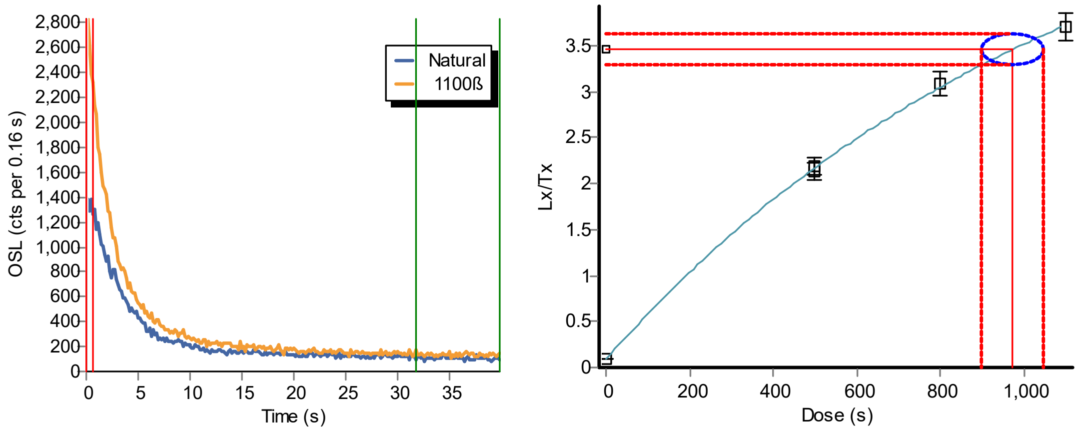
Natural
1100ß
OSL (cts per 0.16 s)
Time (s)
Lx/Tx
Dose (s)

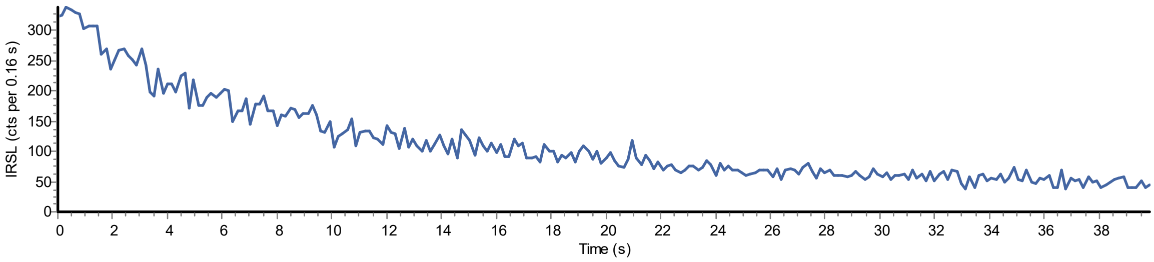

IRSL (cts per 0.16 s)
300
250
200
150
100
50
0
0 2 4 6 8 10 12 14 16 18 20 22 24 26 28 30 32 34 36 38
Time (s)

P6-39m

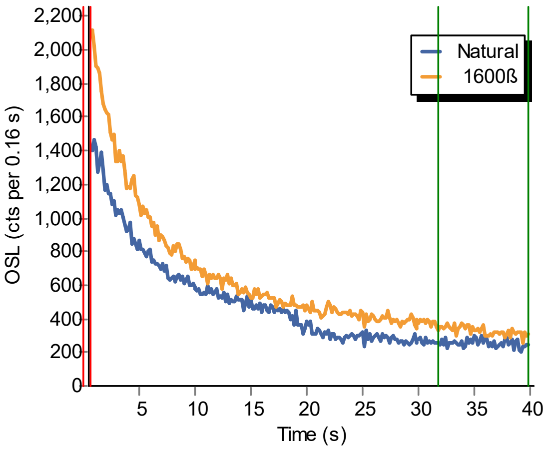

OSL (cts per 0.16 s)
2,200
2,000
1,800
1,600
1,400
1,200
1,000
800
600
400
200
0
5 10 15 20 25 30 35 40
Time (s)
Natural
1600ß

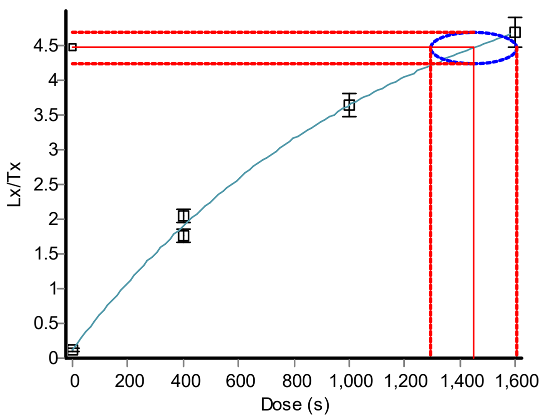

Lx/Tx
4.5
4
3.5
3
2.5
2
1.5
1
0.5
0
0 200 400 600 800 1,000 1,200 1,400 1,600
Dose (s)

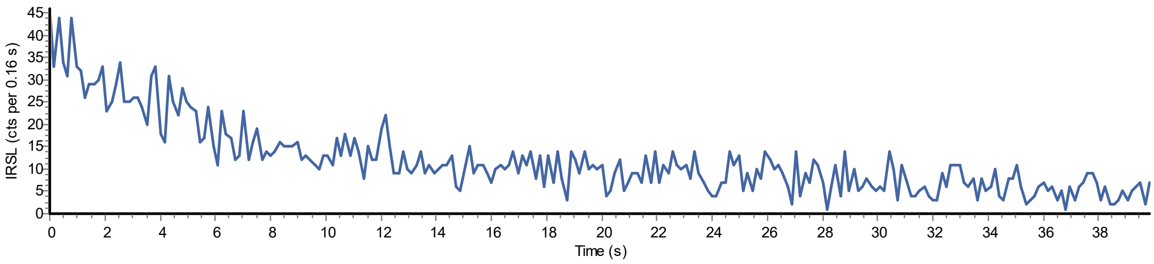

IRSL (cts per 0.16 s)
45
40
35
30
25
20
15
10
5
0
0 2 4 6 8 10 12 14 16 18 20 22 24 26 28 30 32 34 36 38
Time (s)

P6-49m

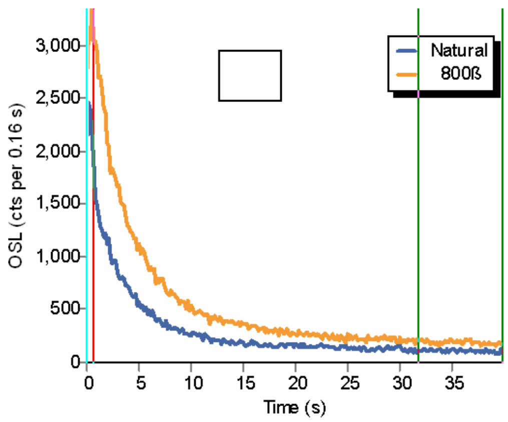
Natural
800ß
OSL (cts per 0.16 s)
Time (s)

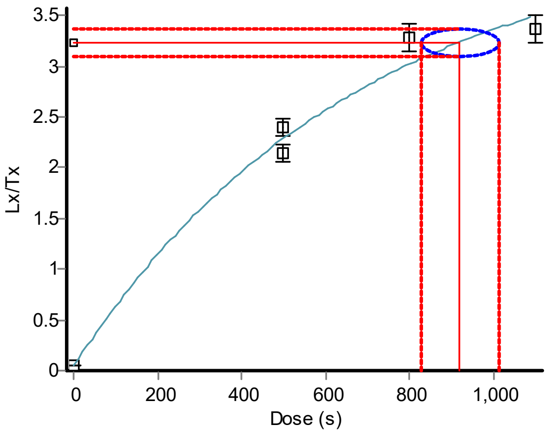
Lx/Tx
Dose (s)

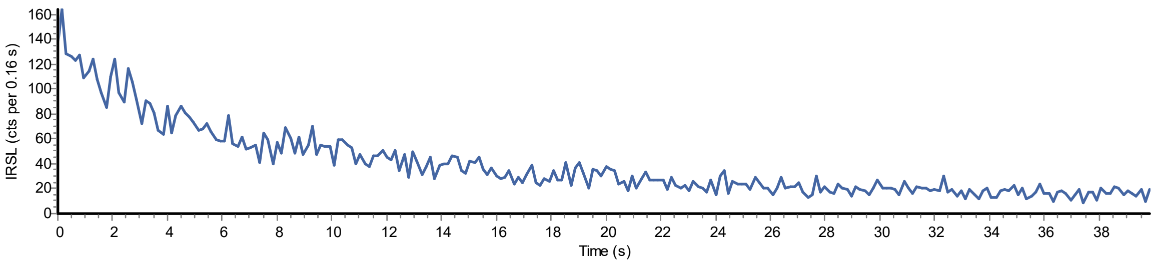
IRSL (cts per 0.16 s)
Time (s)

P7-57m

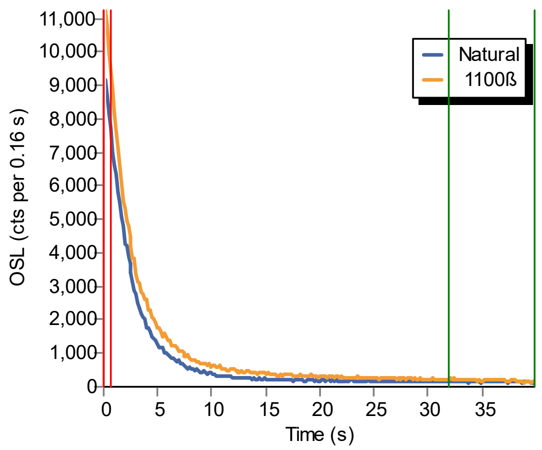
Natural
1100ß
OSL (cts per 0.16 s)
Time (s)

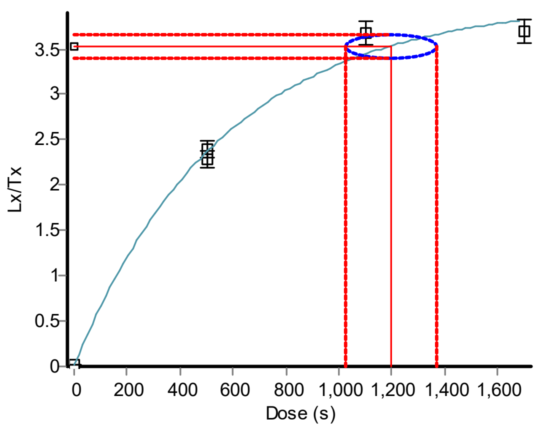
Lx/Tx
Dose (s)

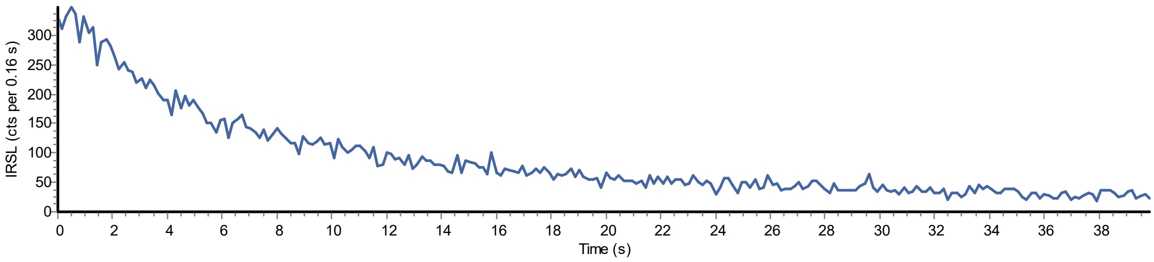
IRSL (cts per 0.16 s)
Time (s)

P7-71m

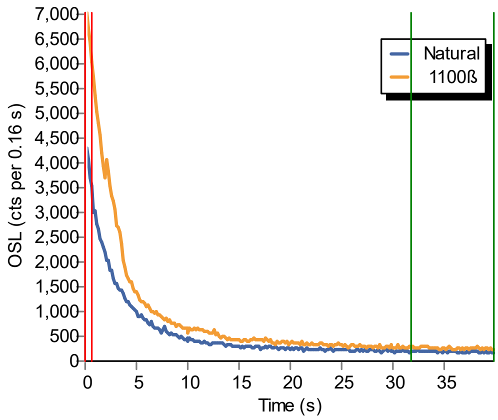
OSL (cts per 0.16 s)
Time (s)
Natural
1100ß

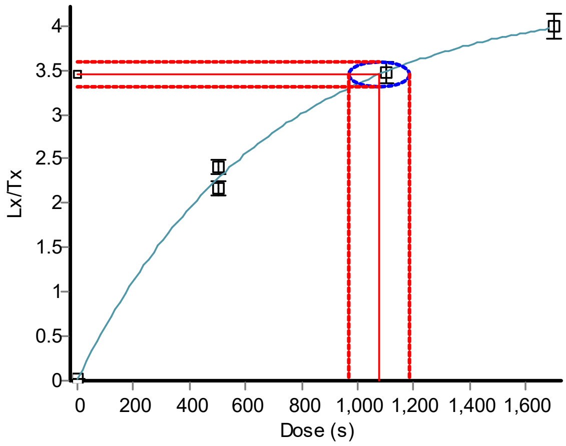
Lx/Tx
Dose (s)

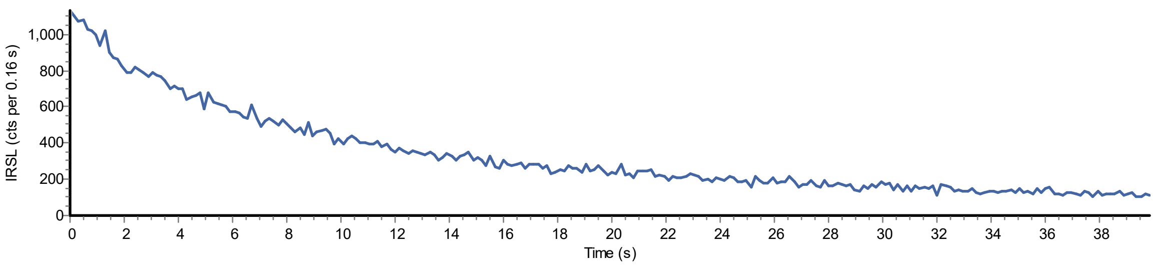
IRSL (cts per 0.16 s)
Time (s)

P9-40m

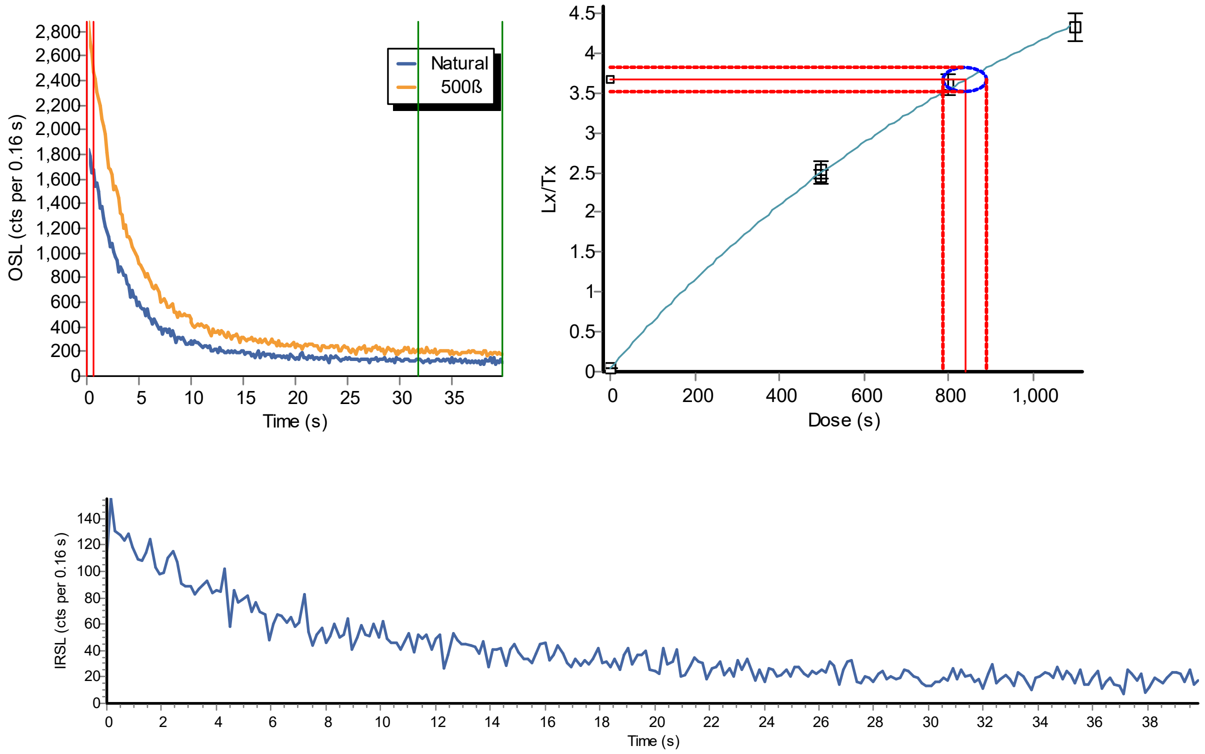

Figure S5. Examples of typical OSL shine down curves (luminescence stimulated in the lab over 40 s of exposure to light) (right panels) and regenerative curves (left panels) for the measured samples. The shine down curves for all aliquots showed fast decay patterns that confirm that the signal is the fast component of luminescence, which is dominant in quartz. Bottom panel shows the decay curve of infrared stimulated luminescence (IRSL).

P3-31M

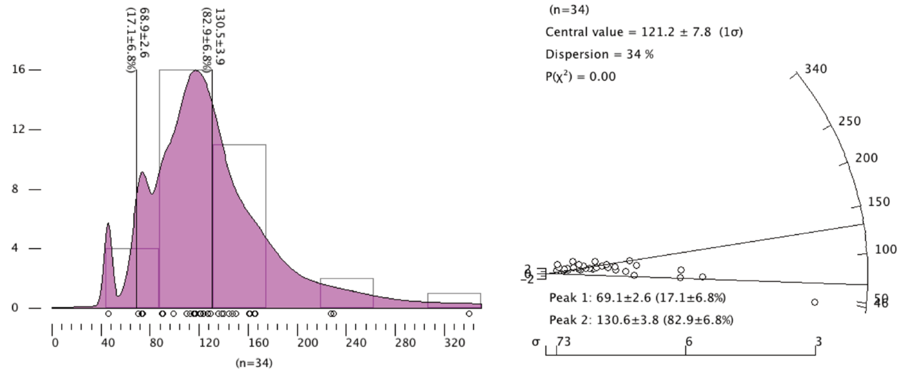

P3-39M

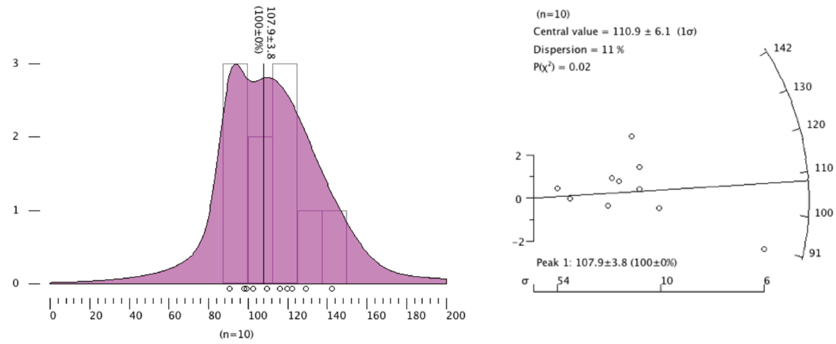

P3-41M

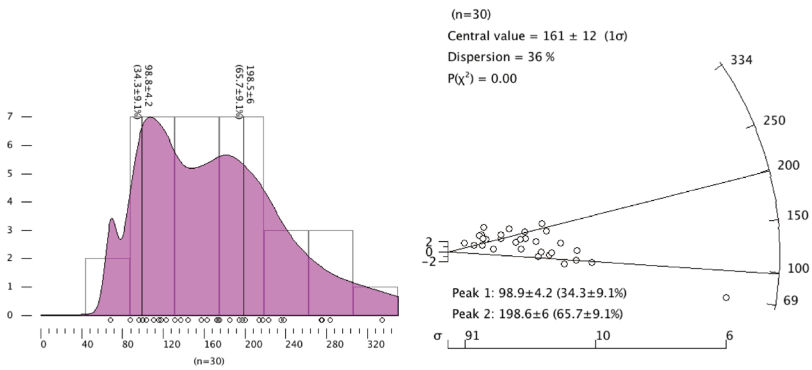

P3-49M

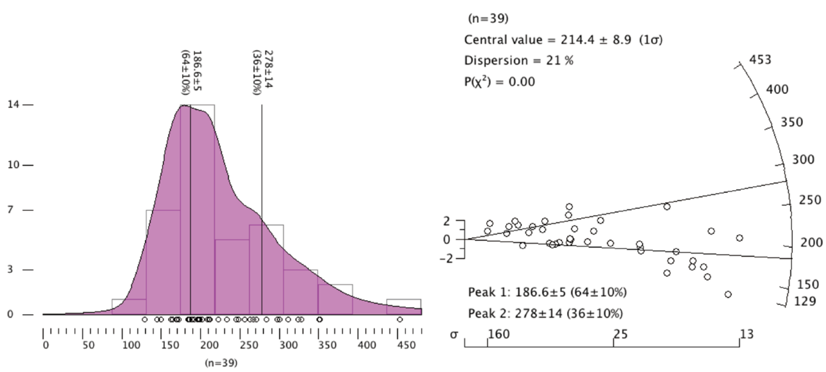

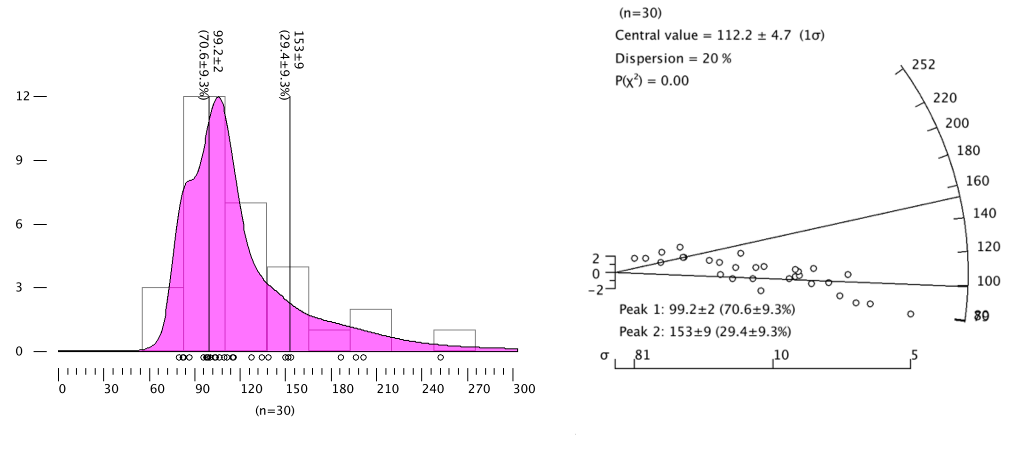
99.2±2
(70.6±9.3%)
153±9
(29.4±9.3%)
(n=30)
(n=30)
Central value = 112.2 ± 4.7 (1σ)
Dispersion = 20 %
P(χ²) = 0.00
Peak 1: 99.2±2 (70.6±9.3%)
Peak 2: 153±9 (29.4±9.3%)

P2-23m

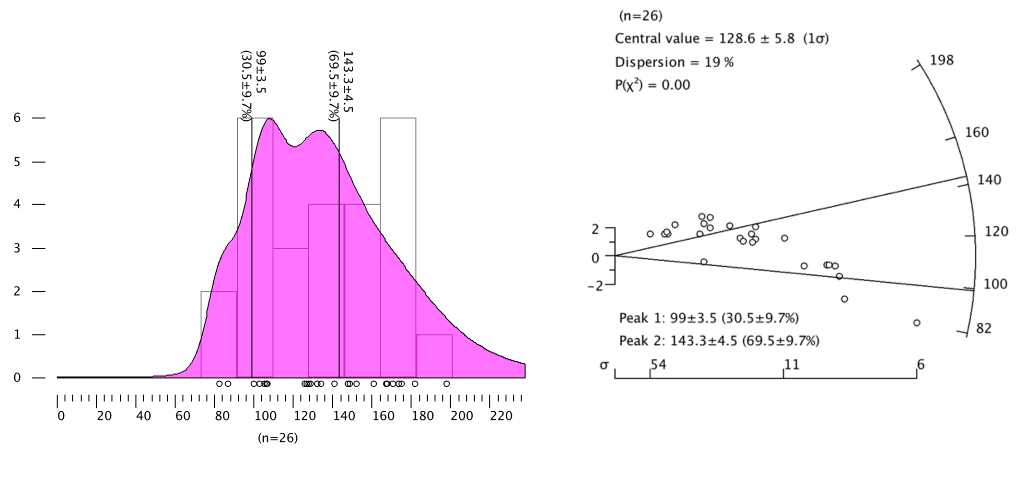
99±3.5
(30.5±9.7%)
143.3±4.5
(69.5±9.7%)
(n=26)
(n=26)
Central value = 128.6 ± 5.8 (1σ)
Dispersion = 19 %
P(χ²) = 0.00
Peak 1: 99±3.5 (30.5±9.7%)
Peak 2: 143.3±4.5 (69.5±9.7%)

P2-27m

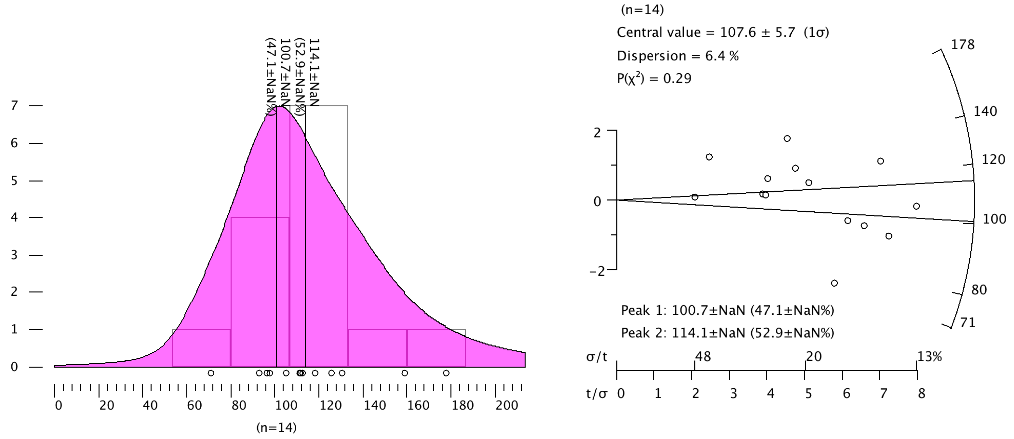
114.1±NaN
(52.9±NaN%)
100.7±NaN
(47.1±NaN%)
(n=14)
(n=14)
Central value = 107.6 ± 5.7 (1σ)
Dispersion = 6.4 %
P(χ²) = 0.29
Peak 1: 100.7±NaN (47.1±NaN%)
Peak 2: 114.1±NaN (52.9±NaN%)
σ/t
t/σ

P2-31m

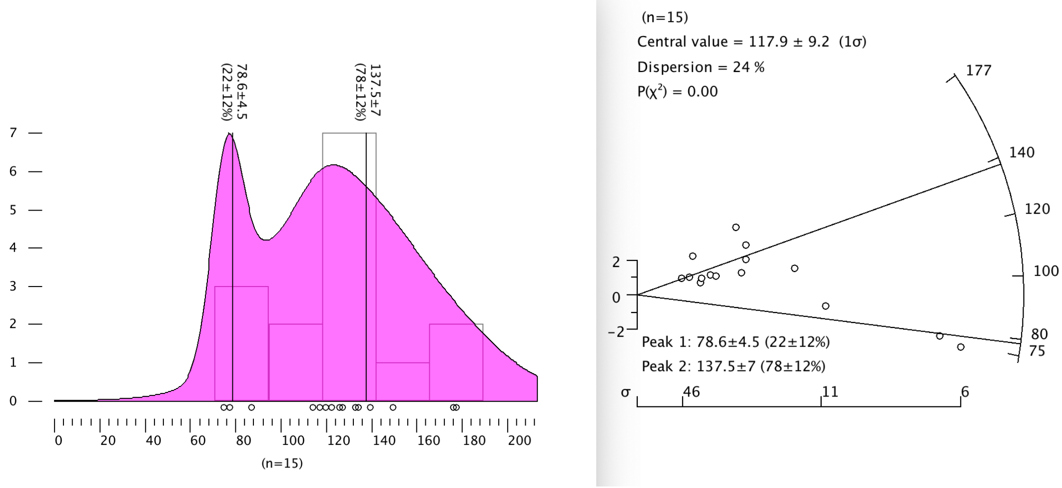
78.6±4.5
(22±12%)
137.5±7
(78±12%)
(n=15)
(n=15)
Central value = 117.9 ± 9.2 (1σ)
Dispersion = 24 %
P(χ²) = 0.00
Peak 1: 78.6±4.5 (22±12%)
Peak 2: 137.5±7 (78±12%)
σ

P2-41m

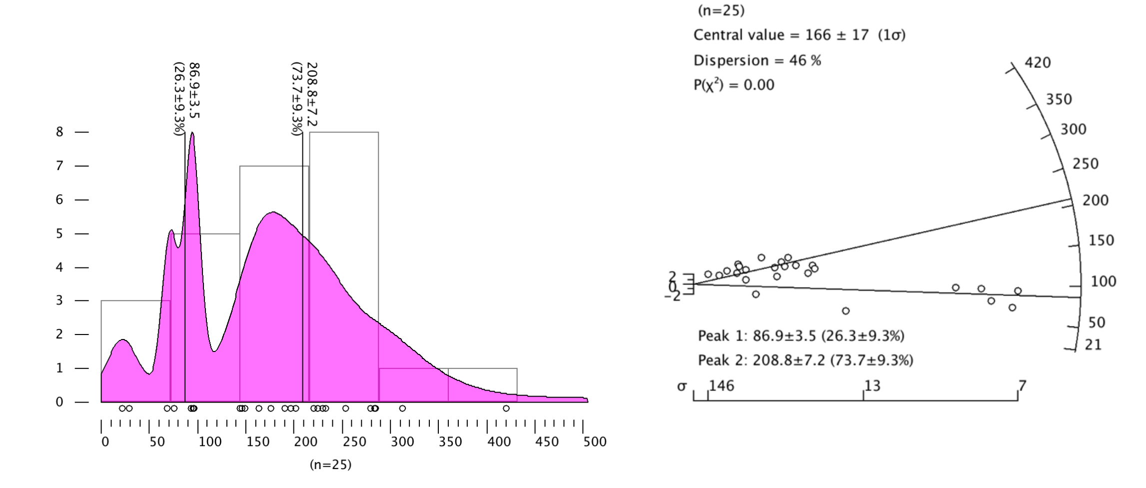
86.9±3.5
(26.3±9.3%)
208.8±7.2
(73.7±9.3%)
(n=25)
(n=25)
Central value = 166 ± 17 (1σ)
Dispersion = 46 %
P(χ²) = 0.00
Peak 1: 86.9±3.5 (26.3±9.3%)
Peak 2: 208.8±7.2 (73.7±9.3%)
σ
146
13
7

P3-29m

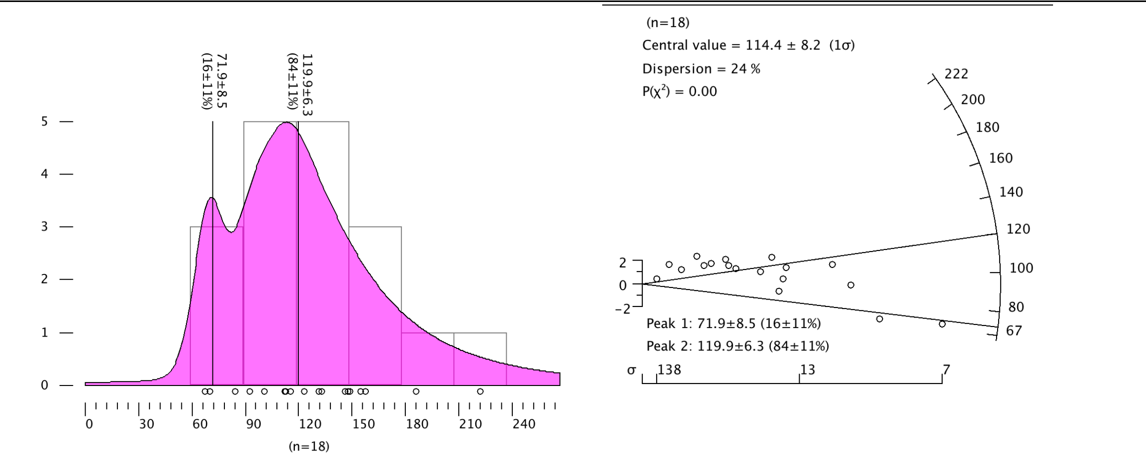
71.9±8.5
(16±11%)
119.9±6.3
(84±11%)
(n=18)
(n=18)
Central value = 114.4 ± 8.2 (1σ)
Dispersion = 24 %
P(χ²) = 0.00
Peak 1: 71.9±8.5 (16±11%)
Peak 2: 119.9±6.3 (84±11%)
σ
138
13
7

P4-51m

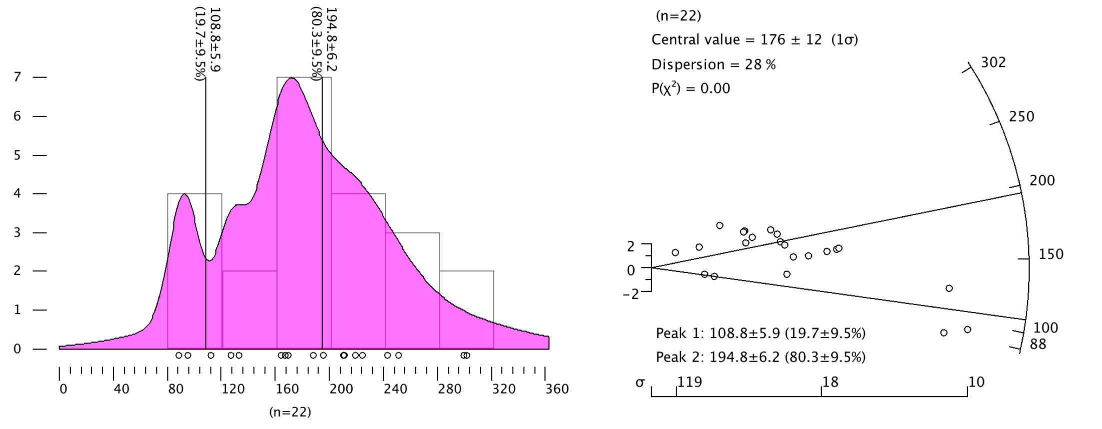
108.8±5.9
(19.7±9.5%)
194.8±6.2
(80.3±9.5%)
(n=22)
(n=22)
Central value = 176 ± 12 (1σ)
Dispersion = 28 %
P(χ²) = 0.00
Peak 1: 108.8±5.9 (19.7±9.5%)
Peak 2: 194.8±6.2 (80.3±9.5%)
σ
119
18
10
302
250
200
150
100
88

P4-69m

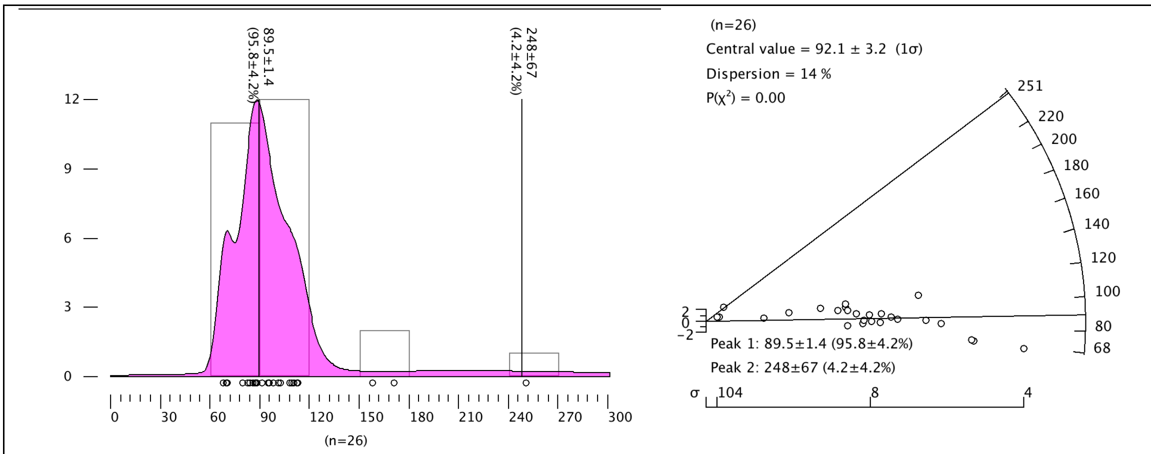
89.5±1.4
(95.8±4.2%)
248±67
(4.2±4.2%)
(n=26)
(n=26)
Central value = 92.1 ± 3.2 (1σ)
Dispersion = 14 %
P(χ²) = 0.00
Peak 1: 89.5±1.4 (95.8±4.2%)
Peak 2: 248±67 (4.2±4.2%)
σ
104
8
4
251
220
200
180
160
140
120
100
80
68

P4-99m

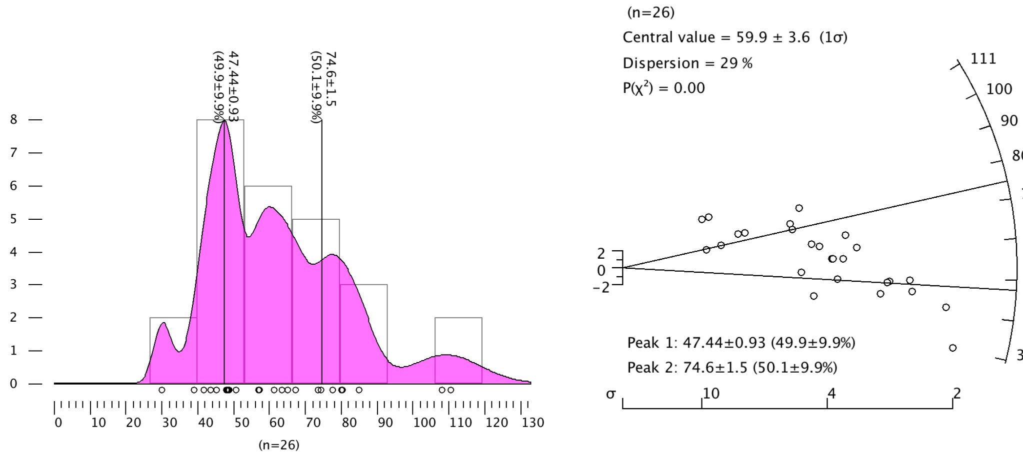
47.44±0.93
(49.9±9.9%)
74.6±1.5
(50.1±9.9%)
(n=26)
(n=26)
Central value = 59.9 ± 3.6 (1σ)
Dispersion = 29 %
P(χ²) = 0.00
Peak 1: 47.44±0.93 (49.9±9.9%)
Peak 2: 74.6±1.5 (50.1±9.9%)
σ

P6-19m

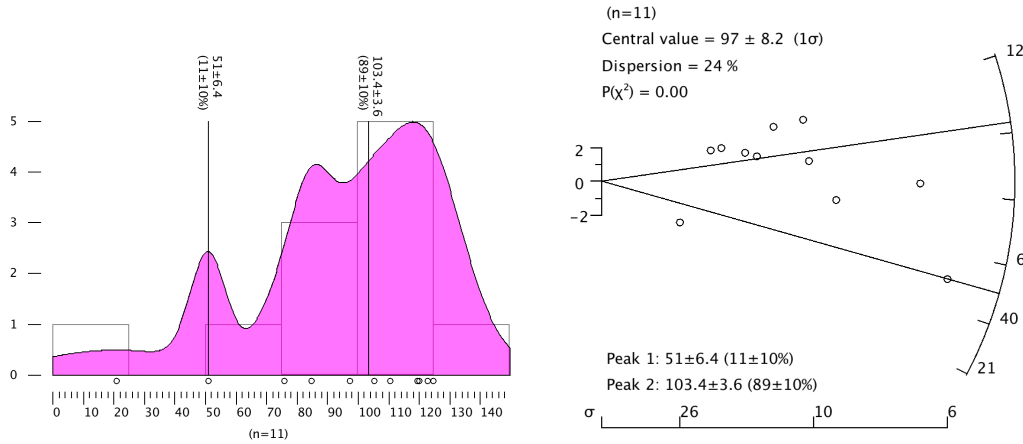
51±6.4
(11±10%)
103.4±3.6
(89±10%)
(n=11)
(n=11)
Central value = 97 ± 8.2 (1σ)
Dispersion = 24 %
P(χ²) = 0.00
Peak 1: 51±6.4 (11±10%)
Peak 2: 103.4±3.6 (89±10%)
σ

P6-33m

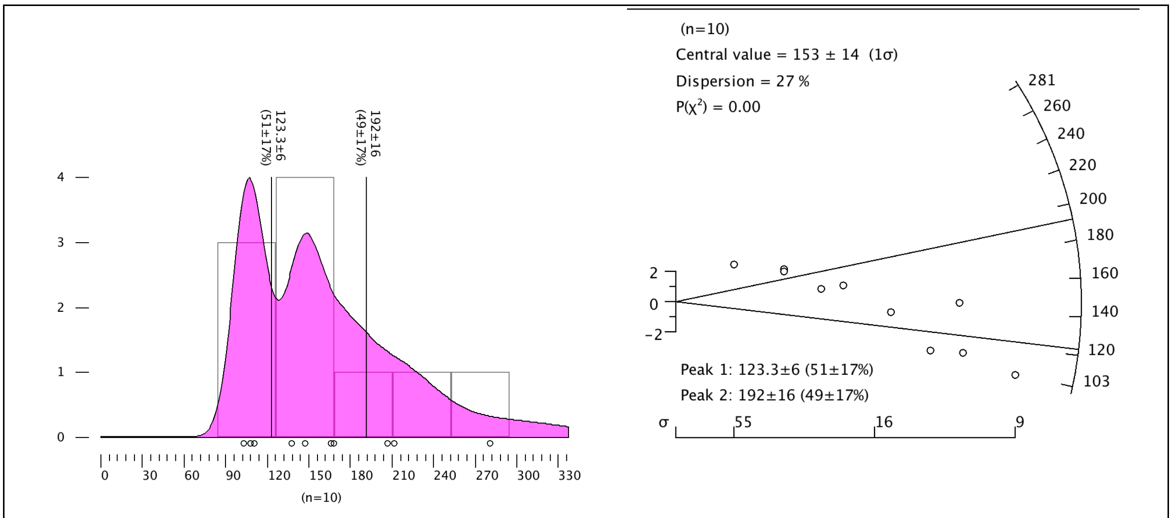

(n=10)
Central value = 153 ± 14 (1σ)
Dispersion = 27 %
P(χ²) = 0.00
123.3±6 (51±17%)
192±16 (49±17%)
Peak 1: 123.3±6 (51±17%)
Peak 2: 192±16 (49±17%)

P6-39m

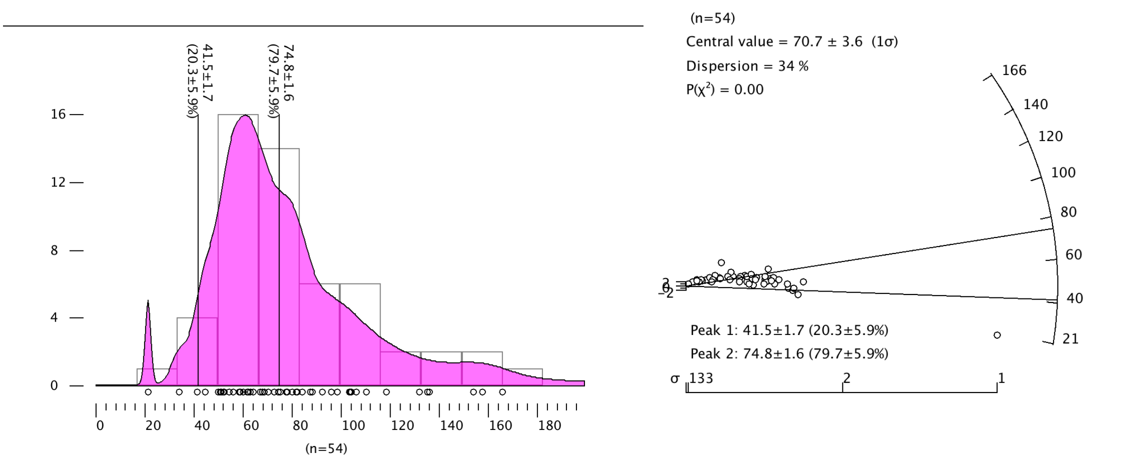

(n=54)
Central value = 70.7 ± 3.6 (1σ)
Dispersion = 34 %
P(χ²) = 0.00
41.5±1.7 (20.3±5.9%)
74.8±1.6 (79.7±5.9%)
Peak 1: 41.5±1.7 (20.3±5.9%)
Peak 2: 74.8±1.6 (79.7±5.9%)

P6-49m

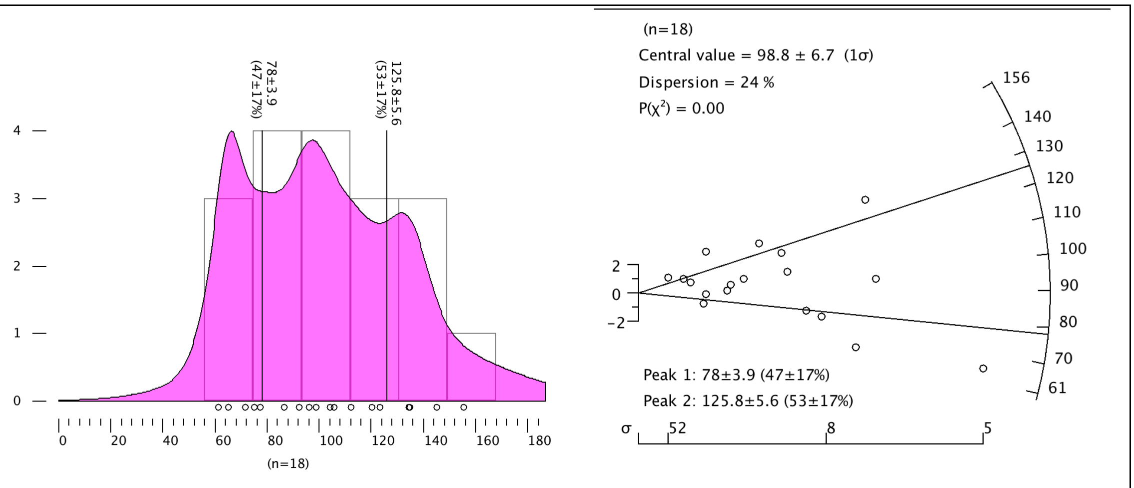
78±3.9
(47±17%)
125.8±5.6
(53±17%)
(n=18)
Central value = 98.8 ± 6.7 (1σ)
Dispersion = 24 %
P(χ²) = 0.00
Peak 1: 78±3.9 (47±17%)
Peak 2: 125.8±5.6 (53±17%)
σ
52
8
5
156
140
130
120
110
100
90
80
70
61
0 20 40 60 80 100 120 140 160 180
(n=18)

P7-57m

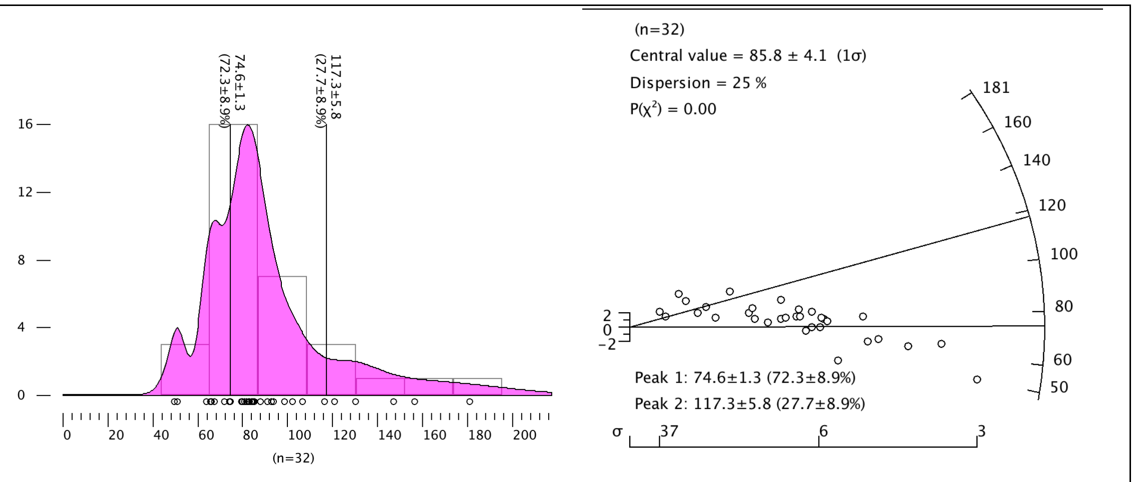
74.6±1.3
(72.3±8.9%)
117.3±5.8
(27.7±8.9%)
(n=32)
Central value = 85.8 ± 4.1 (1σ)
Dispersion = 25 %
P(χ²) = 0.00
Peak 1: 74.6±1.3 (72.3±8.9%)
Peak 2: 117.3±5.8 (27.7±8.9%)
σ
37
6
3
181
160
140
120
100
80
60
50
0 20 40 60 80 100 120 140 160 180 200
(n=32)

P7-71m

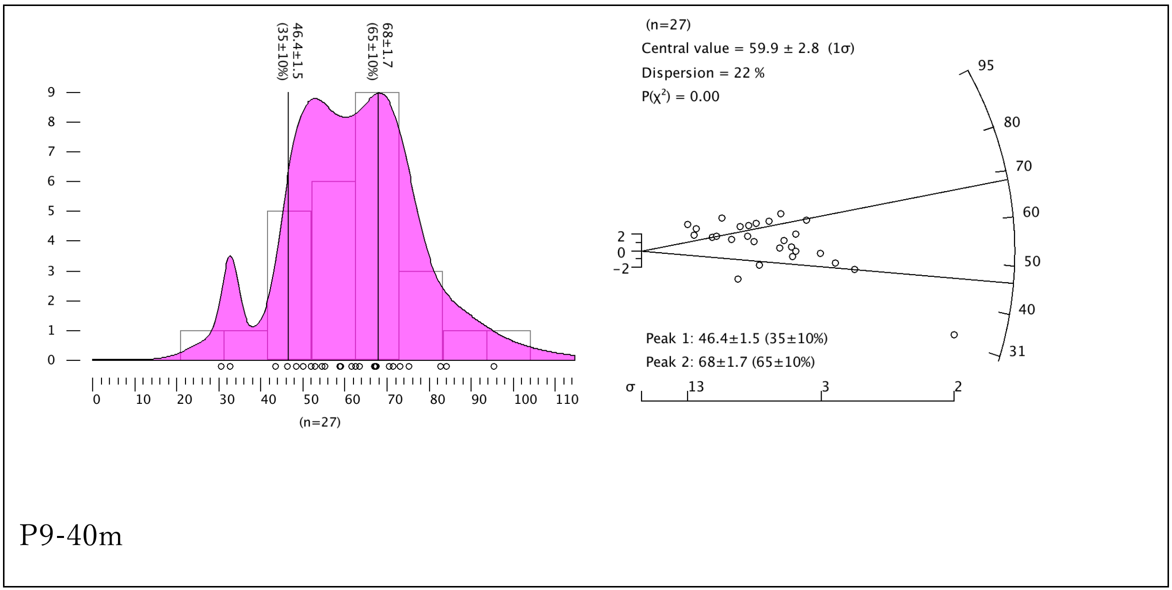

Figure S6. Equivalent doses for measured samples plotted as histograms (number of aliquots) and probability against equivalent dose (Gy) (right panels), and radial plots for each sample using a two-mixing model (left panels). The spread of equivalent dose varies among the samples. A minimum age model separating the population of equivalent dose was employed using a two-mixing model (Vermeesch, 2009). We used the equivalent dose value of the minimum peak from this analysis to calculate the age (Table 2).

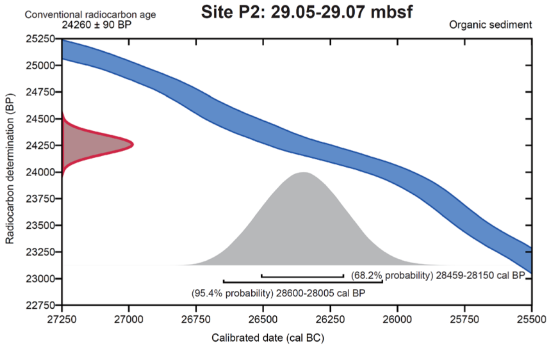
Site P2: 29.05-29.07 mbsf
Conventional radiocarbon age
24260 ± 90 BP
Organic sediment
(68.2% probability) 28459-28150 cal BP
(95.4% probability) 28600-28005 cal BP
Radiocarbon determination (BP)
Calibrated date (cal BC)

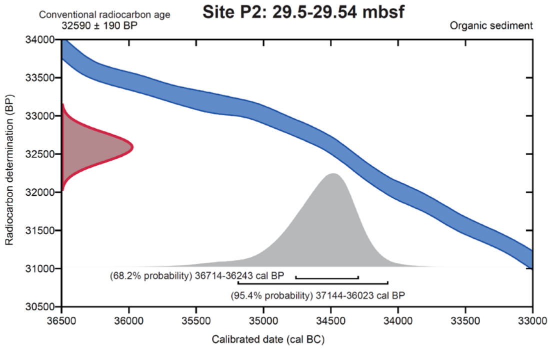
Site P2: 29.5-29.54 mbsf
Conventional radiocarbon age
32590 ± 190 BP
Organic sediment
(68.2% probability) 36714-36243 cal BP
(95.4% probability) 37144-36023 cal BP
Radiocarbon determination (BP)
Calibrated date (cal BC)

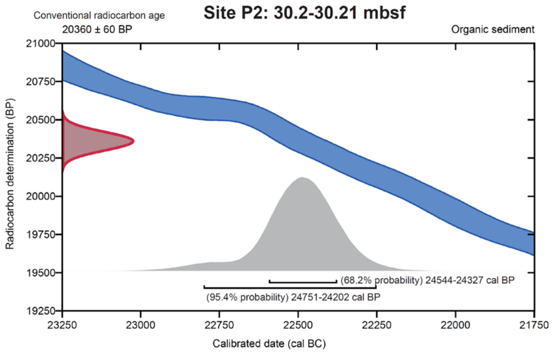
Site P2: 30.2-30.21 mbsf
Conventional radiocarbon age
20360 ± 60 BP
Organic sediment
(68.2% probability) 24544-24327 cal BP
(95.4% probability) 24751-24202 cal BP
Radiocarbon determination (BP)
Calibrated date (cal BC)

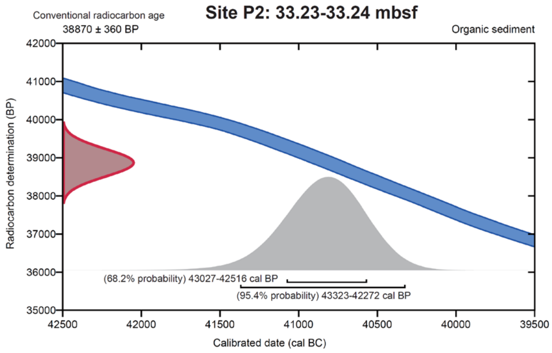
Site P2: 33.23-33.24 mbsf
Conventional radiocarbon age
38870 ± 360 BP
Organic sediment
(68.2% probability) 43027-42516 cal BP
(95.4% probability) 43323-42272 cal BP
Radiocarbon determination (BP)
Calibrated date (cal BC)

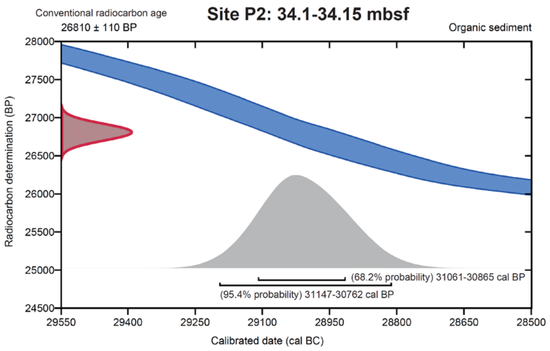
Site P2: 34.1-34.15 mbsf
Conventional radiocarbon age
26810 ± 110 BP
Organic sediment
(68.2% probability) 31061-30865 cal BP
(95.4% probability) 31147-30762 cal BP
Radiocarbon determination (BP)
Calibrated date (cal BC)

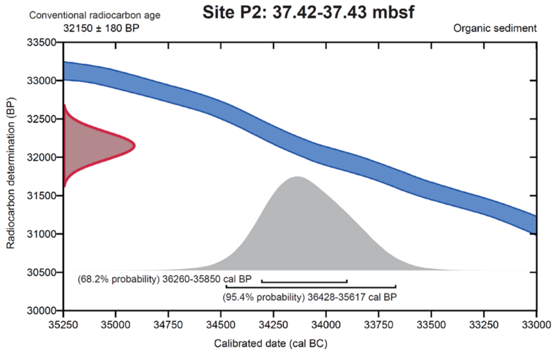
Site P2: 37.42-37.43 mbsf
Conventional radiocarbon age
32150 ± 180 BP
Organic sediment
(68.2% probability) 36260-35850 cal BP
(95.4% probability) 36428-35617 cal BP
Radiocarbon determination (BP)
Calibrated date (cal BC)

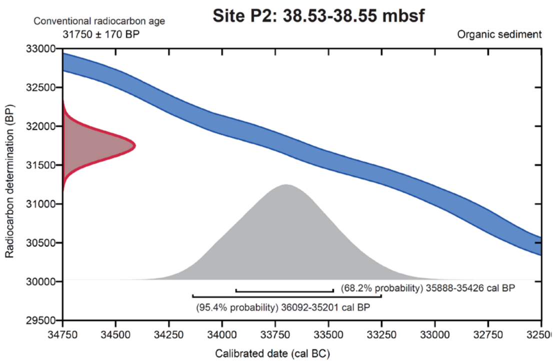
Site P2: 38.53-38.55 mbsf
Conventional radiocarbon age
31750 ± 170 BP
Organic sediment
(68.2% probability) 35888-35426 cal BP
(95.4% probability) 36092-35201 cal BP
Radiocarbon determination (BP)
Calibrated date (cal BC)

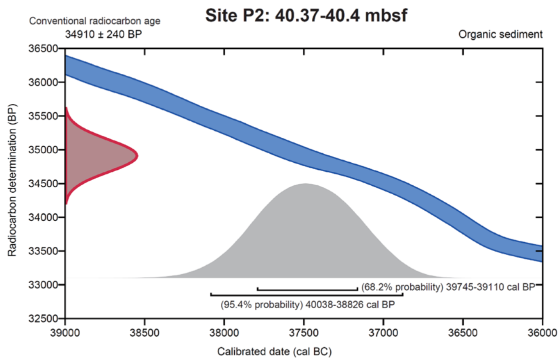
Site P2: 40.37-40.4 mbsf
Conventional radiocarbon age
34910 ± 240 BP
Organic sediment
(68.2% probability) 39745-39110 cal BP
(95.4% probability) 40038-38826 cal BP
Radiocarbon determination (BP)
Calibrated date (cal BC)

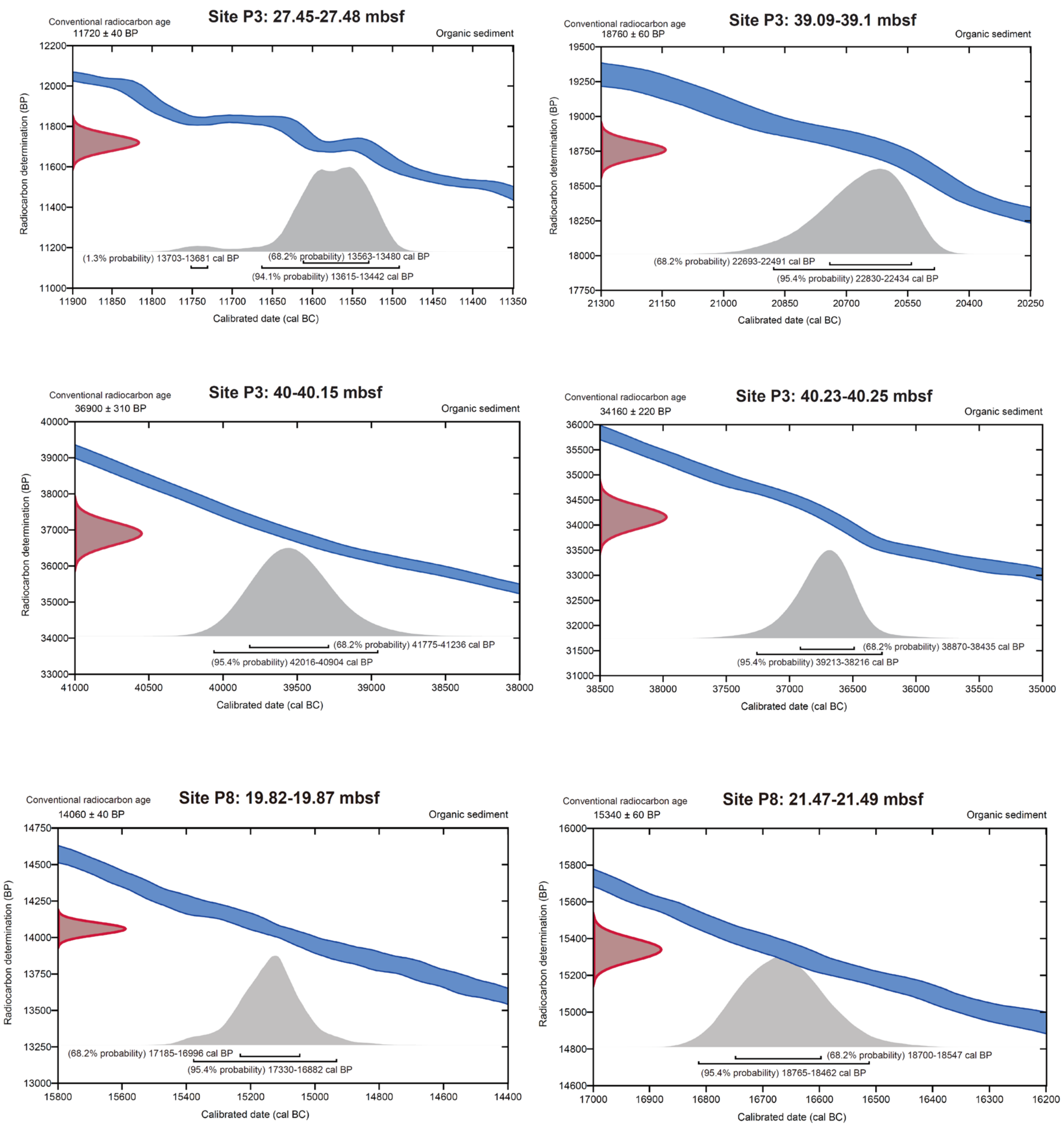

Figure S7. Radiocarbon dating results measured at Beta Analytics Inc., and calibration of radiocarbon age to calendar years for the 18 samples reported in this paper. Sample information is shown above each chart. Calibration of the conventional radiocarbon age were performed using the 2013 calibration databases (INTCAL13) (Reimer et al., 2013), high probability density range method and Bayesian probability analysis (Ramsey, 2009).

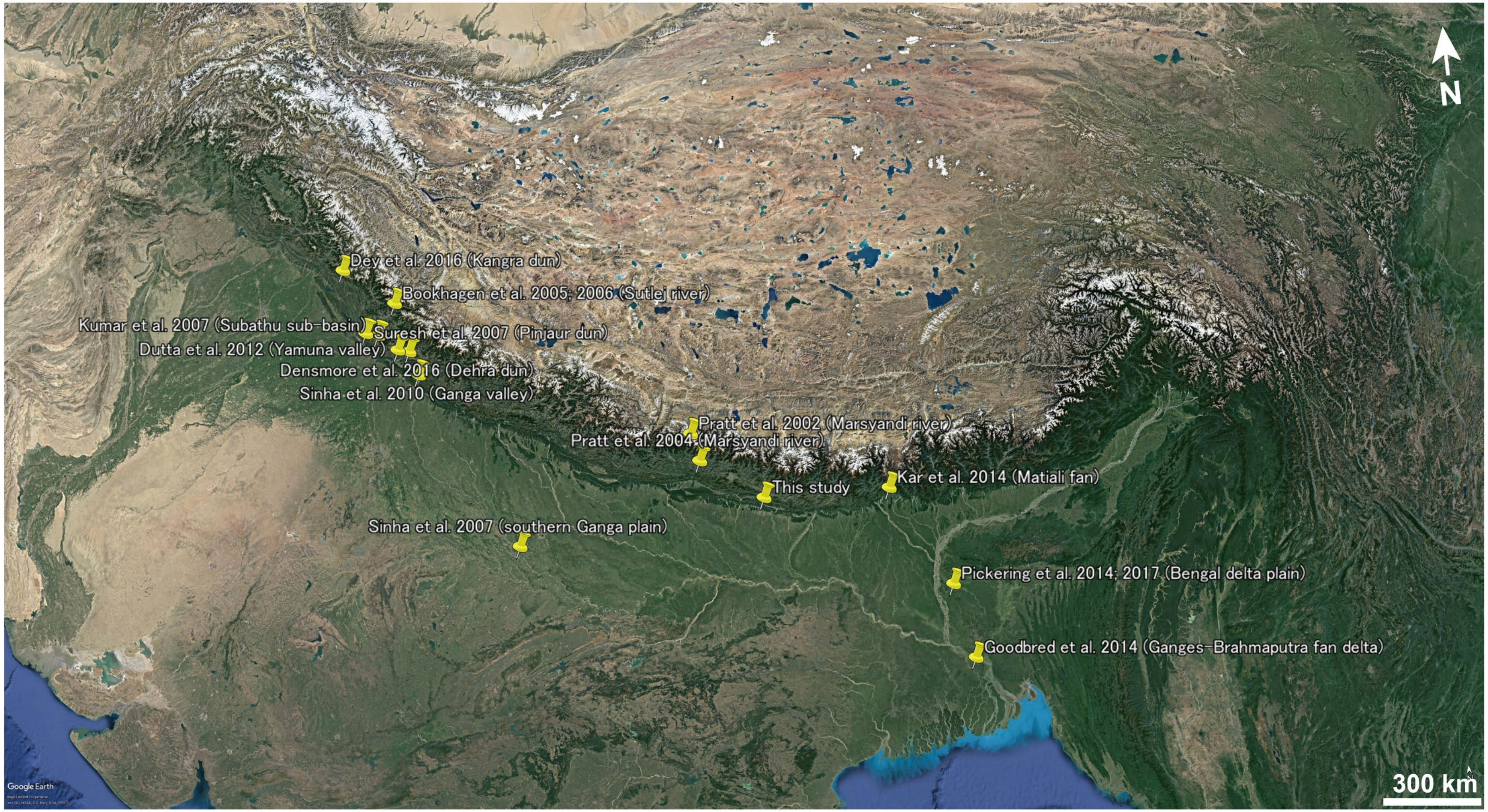
N
Dey et al. 2016 (Kangra dun)
Bookhagen et al. 2005; 2006 (Sutlej river)
Kumar et al. 2007 (Subathu sub-basin)
Suresh et al. 2007 (Pinjaur dun)
Dutta et al. 2012 (Yamuna valley)
Densmore et al. 2016 (Dehra dun)
Sinha et al. 2010 (Ganga valley)
Pratt et al. 2002 (Marsyandi river)
Pratt et al. 2004 (Marsyandi river)
This study
Kar et al. 2014 (Matiali fan)
Sinha et al. 2007 (southern Ganga plain)
Pickering et al. 2014; 2017 (Bengal delta plain)
Goodbred et al. 2014 (Ganges-Brahmaputra fan delta)
300 km
Google Earth

Figure S8. Regional satellite map showing locations of previous studies in other foreland regions (Pratt et al., 2002; 2004; Bookhagen et al., 2005; 2006; Kumar et al., 2007; Sinha et al., 2007; Suresh et al., 2007; Sinha et al., 2010; Dutta et al., 2012; Goodbred et al., 2014; Kar et al., 2014; Pickering et al., 2014; 2017; Densmore et al., 2016; Dey et al., 2016) and this study. Satellite image uses map from Google Earth imagery, Image Landsat/Copernicus.

Dataset S1. Core description sheets for Sites P1-P10, which are the raw data from which we created the core logs in this study. The files contain excel spreadsheets that include our lithological and structural data for each site.

Dataset S2. Geotechnical reports created by the drilling company (Geotech Solutions International Pvt. Ltd.). The files contain drilling procedures, photos, on-site reports, core and sample handling, and on-site logs of the cores.